Dynamic Control of Radiative Heat Transfer with Tunable Materials for Thermal Management in Both Far and Near Fields

by

Yue Yang

A Dissertation Presented in Partial Fulfillment
of the Requirements for the Degree
Doctor of Philosophy

Approved July 2016 by the
Graduate Supervisory Committee:

Liping Wang, Chair
Patrick Phelan
Robert Wang
Sefaattin Tongay
Konrad Rykaczewski

ARIZONA STATE UNIVERSITY

August 2016

ABSTRACT

The proposed research mainly focuses on employing tunable materials to achieve dynamic control of radiative heat transfer in both far and near fields for thermal management. Vanadium dioxide (VO_2), which undergoes a phase transition from insulator to metal at the temperature of 341 K, is one tunable material being applied. The other one is graphene, whose optical properties can be tuned by chemical potential through external bias or chemical doping.

In the far field, a VO_2-based metamaterial thermal emitter with switchable emittance in the mid-infrared has been theoretically studied. When VO_2 is in the insulating phase, high emittance is observed at the resonance frequency of magnetic polaritons (MPs), while the structure becomes highly reflective when VO_2 turns metallic. A VO_2-based thermal emitter with tunable emittance is also demonstrated due to the excitation of MP at different resonance frequencies when VO_2 changes phase. Moreover, an infrared thermal emitter made of graphene-covered SiC grating could achieve frequency-tunable emittance peak via the change of the graphene chemical potential.

In the near field, a radiation-based thermal rectifier is constructed by investigating radiative transfer between VO_2 and SiO_2 separated by nanometer vacuum gap distances. Compared to the case where VO_2 is set as the emitter at 400 K as a metal, when VO_2 is considered as the receiver at 300 K as an insulator, the energy transfer is greatly enhanced due to the strong surface phonon polariton (SPhP) coupling between insulating VO_2 and SiO_2. A radiation-based thermal switch is also explored by setting VO_2 as both the emitter and the receiver. When both VO_2 emitter and receiver are at the insulating phase, the switch is at the “on” mode with a much enhanced heat flux due to strong SPhP

coupling, while the near-field radiative transfer is greatly suppressed when the emitting VO_2 becomes metallic at temperatures higher than 341K during the "off" mode. In addition, an electrically-gated thermal modulator made of graphene covered SiC plates is theoretically studied with modulated radiative transport by varying graphene chemical potential. Moreover, the MP effect on near-field radiative transport has been investigated by spectrally enhancing radiative heat transfer between two metal gratings.

ACKNOWLEDGMENTS

I am most grateful to Dr. Liping Wang, who has served as my Ph.D. advisor and guided my scientific research for four years. As an advisor, he is equipped with lots of passion and expertise in the areas relevant to my research topics, and he is always patient to teach me every detail he can think about to help me improve. I can't imagine how many nights he spent to go through every word of my manuscript writings and every detail of the manuscript figures. I have learned a lot from the excellent experience under his guidance. Treating me also as a friend, he is so willing to help me with everything in my life, and he always offers the help before I ask. I really appreciate all of his efforts.

I would also like to thank Dr. Patrick Phelan, Dr. Robert Wang, Dr. Sefaattin Tongay, and Dr. Konrad Rykaczewski, who took their time to serve on my dissertation reading committee and provide valuable advice. Some researches presented in this dissertation were supported by the National Science Foundation and Arizona State University. Sincere appreciation is also expressed to my former and current group members, and I benefited a lot by collaborating and interacting with them during my Ph.D. study.

Moreover, my deep gratitude goes to my family: parents, parents-in-law, sister and most importantly my wife, Dating Jiang. Without their support and encouragement, there would be no way for me to be successful. To support my Ph.D. study, my wife quitted her job in China and came to US two years ago, then quitted her graduate study plan again to stay at home to take care of our 1-year-old baby, Joey Qiaoyi Yang. I want to say thank you to my beloved wife from my deepest heart for all the sacrifice she made for this family.

TABLE OF CONTENTS

Page

LIST OF TABLES

Table Page

LIST OF FIGURES

Figure Page

Figure Page

Figure Page

Figure Page

Figure Page

CHAPTER 1 INTRODUCTION

Far-field thermal radiation considers the radiative heat transfer between two objects separated by a distance d which is much larger than the wavelength of interest, i.e., $d >> \lambda$. Besides the geometric view factor, the surface emissivity, which is generally a function of wavelength, polarization, direction, surface roughness and temperature, is a crucial material property to determine the amount of radiative heat transfer, which, however, has to be smaller to the blackbody limit in the far field. Tailoring the surface emissivity could find numerous applications in various energy systems for power generation and thermal management, optics, microelectronics, and so on. On the other hand, when the two objects are brought close together such that the distance d is much smaller than wavelength, i.e., $d << \lambda$, the evanescent waves, whose amplitude exponentially decays away from the surface and thus does not transport energy in the far field, starts to dominate the radiative transfer over the propagating waves in the so-called near-field regime. Due to the coupling of evanescent waves, in particular resonant surface modes, it has been demonstrated theoretically and experimentally that the radiative transfer in the near field could exceed the far-field blackbody limit by several orders of magnitude, depending on the materials and the vacuum gap distances, which enables promising applications like energy harvesting, thermal management, imaging and manufacturing. This chapter reviews the state-of-the-art research on selective control of tunable far-field thermal emission and near-field radiative heat transfer enhancement, followed by the objectives of the proposed PhD research tasks.

1.1 Selective and Tunable Emission/Absorption in Far Field

Great progress has been made on both selective absorbers and thermal emitters in the past decade, and various applications like radiative cooling [3], sensing [4] and energy conversion systems [5, 6] have been found. As a pioneering work in coherent thermal sources, Greffet et al. demonstrated both temporal and spatial coherence of thermal emission from SiC gratings by exciting surface phonon polaritons (SPhP) [7]. Similarly, surface plasmon polaritons can be employed in metallic micro/nanostructures such as one-dimensional (1D) complex grating [8], 2D tungsten grating [9], and photonic crystals [10-12] for tailoring thermal emission. The cavity resonant mode excited in the so-called Salisbury screen [13] and Fabry-Perot cavity [14] is another way to achieve coherent emission. However, beyond the static selective emission or absorption, vanadium dioxide (VO_2), which has been known for its phase transition at temperature of 68°C [1, 15], was used to achieve active control of selective emission or absorption. Tunable metamaterial absorbers in the microwave [16] and THz regimes [17] were designed by using VO_2 film as the ground plane to modulate the impedance match conditions for split-ring resonators (SRRs). Dicken et al. [18] reported a resonance frequency tunable metamaterial in the near-infrared by depositing split-ring resonators on a continuous VO_2 film, which modulates surface plasmon at different phases. Similarly, a thermally tunable mid-infrared metamaterial made of a Y-shape plasmonic antenna array on a VO_2 film was demonstrated [19]. Dicken et al. also proposed an ultra-thin tunable perfect absorber based on the VO_2 phase transition [20]. Besides, Ben-Abdallah et al. [21] proposed a phase-change thermal antenna made of patterned VO_2 gratings that exhibits switchable thermal emission enabled by surface plasmon polaritons excited with the

metallic phase of VO_2. Designs reported above were mainly realized by modulating the excitation condition of surface plasmon polariton (SPP), and the tunability was quite limited.

Graphene, whose optical properties can be electrically tuned by changing its chemical potential [22-24], has been recently employed in the novel designs of switchable and tunable metamaterials. Tunable selective transmission has been investigated in patterned graphene ribbon arrays by actively exciting plasmonic resonances [25, 26]. One step further, Chu et al. introduced an active plasmonic switch with dynamically controlled transmission in both single and multi-layer graphene ribbon arrays [27]. In addition, tunable perfect absorbers were investigated with graphene ribbon array on dielectric spacer and metallic substrate [28, 29]. Fang et al. demonstrated tunable selective absorption in graphene disk arrays [30]. Enhanced light absorption was also observed in graphene layer integrated with a metamaterial perfect absorber [31]. However, graphene-based tunable coherent thermal emission has not been demonstrated yet.

1.2 Enhanced and Tunable Radiative Heat Transfer in Near Field

Significant research progress has been made during the past decade on thermal management with phonon-based thermal rectifiers [32-35] and transistors [36]. Thermal switches have also been realized by making and breaking thermal contact between two interfaces applications [37-39]. However, the repeating mechanical movement limits the lifetime of these switches and phonon-based thermal device might suffer from low speed due to inherent behavior of the energy carrier, while photon transport has certain

advantages such as much faster speed. The researches on nanoscale thermal radiation have showed that the radiant energy exchanges in near field can exceed that predicted by Planck's law by a few orders of magnitude [40-44]. The surface plasmon or phonon polaritons (SPhPs) effect [45, 46] can significantly enhance the near-field thermal radiation. These facts make it possible to use thermal radiation for thermal management by manipulating heat flow in the near field.

Otey et al. [47] were the first to propose a vacuum thermal rectifier based on the near-field radiation made of two semi-infinite isotropic SiC-3C and uniaxial SiC-6H plates with temperature dependent dielectric functions. Later, Iizuka and Fan [48] looked into the effect of a dielectric coating on one SiC plate. Basu and Francoeur [49] investigated the thermal rectification between a film and half-space of doped silicon with different doping concentrations. Wang and Zhang [50] explored the rectification effect between intrinsic bulk silicon and a dissimilar material at higher emitter temperatures. However, in order to obtain significant thermal rectification, the previously proposed radiation-based thermal rectifiers require either high temperatures or extremely small vacuum gaps of several nanometers between two planar surfaces, which is by far not practical to achieve. By taking advantage of the characteristics of near-field thermal radiation, Zhu et al. [51] described a bistable thermal switch made of two SiC plates with different polytypes placed in close proximity with a nanometer vacuum gap, but high temperature above 800 K was required to achieve thermal switch effect.

On the other hand, as a two-dimensional semiconductor, graphene supports tunable surface plasmon in the terahertz and infrared region with variable chemical potentials induced by external voltage biases [22-24]. Recent theoretical studies have

looked into the modulation of near-field radiative heat transfer between graphene-based materials [2, 52-56]. Volokitin et. al [52] studied the near-field radiative energy transfer between graphene and an amorphous SiO2 substrate, and contributions from quantum fluctuations with a drift velocity between the free carries in the graphene and the substrate were also considered besides the thermal fluctuations. Later, tunable near-field radiation transfer between two closely separated graphene sheets was implemented by changing the graphene chemical potential and electron relaxation time [53]. Besides the suspended graphene sheets, the near-field radiation transfer between graphene covered dielectrics was modulated via changing graphene chemical potential [54]. Lim et al. [55] further investigated the near-field radiative transport between graphene covered doped silicon plates. It showed that the radiative heat flux could be modified by both graphene chemical potential and silicon doping level. Recently, Liu et at. [2] demonstrated that the near-field radiative transport could be enhanced between graphene covered gratings compared to plates. A near-field thermal radiation based heat flux splitter was even constructed by looking into the heat transfer between three graphene disks with different chemical potentials [56].

1.3 Primary Objective of the Proposed Research

The primary objective of the proposed research is to achieve dynamic control of radiative heat transfer in both far field and near field using tunable material. The following Chapter 2 will give the theoretical background, which include optical properties of VO_2 and graphene, and numerical methods to calculate radiative properties in far field and radiative transport in near field. Next, proposed work and results on far-

field tunable emission will be discussed in Chapter 3, followed by the investigation of near-field tunable radiative heat transfer in Chapter 4. The effect of magnetic polaritons on near-field radiation has been investigated for the first time, which will be discussed in Chapter 5. As the last section, the conclusion and recommendations will be provided in Chapter 6.

CHAPTER 2 THEORETICAL BACKGROUND

2.1 Optical Properties of Vanadium Dioxide (VO_2) and Graphene

As mentioned above, VO_2 undergoes a phase transition at 341 K, below which it is an insulator. The monoclinic insulating VO_2 exhibits anisotropic dielectric responses, and here we consider the two crystalline orientations to be in and out of the surface [1, 57]. In this case, the insulating VO_2 can be treated as a uniaxial medium with ordinary and extraordinary dielectric responses when the electric field is perpendicular or parallel to the optical axis (i.e., surface normal), respectively.

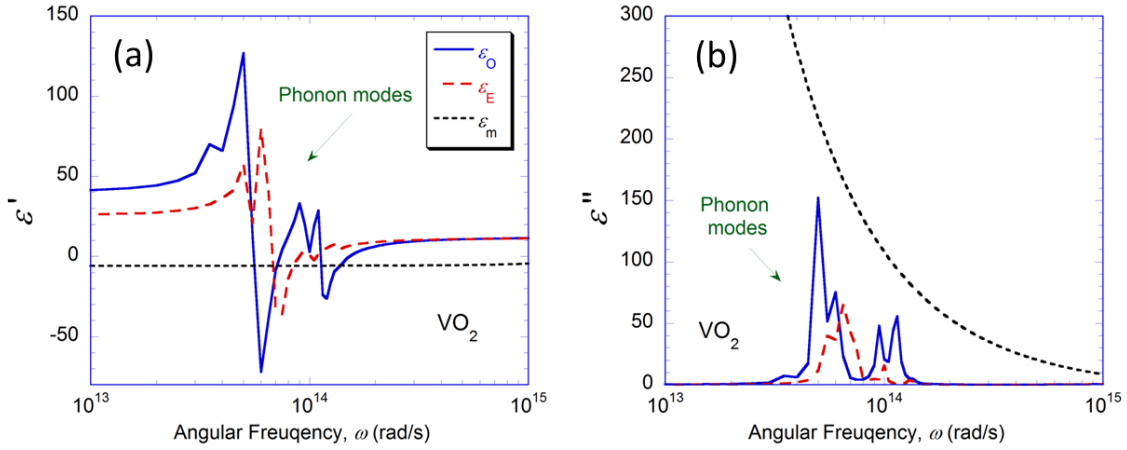

Figure 2.1 The dielectric functions of VO_2: (a) real part ε' and (b) imaginary part ε''. The insulating VO_2 is a uniaxial medium with ordinary (ε_O) and extraordinary dielectric functions (ε_E), while the metallic VO_2 is an isotropic medium, whose dielectric function is denoted as (ε_m). The optical constants of VO_2 are taken from Ref. [1].

A classical oscillator model $\varepsilon(\omega) = \varepsilon_\infty + \sum_{j=1}^{N} \frac{S_j \omega_j^2}{\omega_j^2 - i\gamma_j \omega - \omega^2}$ is used to describe the dielectric functions of insulating VO_2 [58], where ε_∞ is the high-frequency constant, ω is

the angular frequency, ω_j is the phonon vibration frequency, γ is the scattering rate, S_j represents the oscillation strength, and j is the mode index. The experimentally fitted parameters from Barker et al. [1] are used to obtain the ordinary (ε_O) and extraordinary (ε_E) dielectric functions of insulating VO_2. A total of eight modes are considered for ε_O while nine modes are used for ε_E. Figure 2.1 plots the real (ε') and imaginary (ε'') parts of the dielectric functions for both components. Several strong phonon modes are clearly seen for both components in the infrared region from 3×10^{13} rad/s to 1.5×10^{14} rad/s. When the temperature is above the phase transition temperature of 341 K, VO_2 becomes metallic. The isotropic dielectric response of metallic VO_2 can be described by a Drude model $\varepsilon_m = -\omega_p^2\varepsilon_\infty / \left(\omega^2 - i\omega\Gamma\right)$, where $\varepsilon_\infty = 9$, the plasma frequency ω_p = 8000 cm^{-1} and collision frequency Γ = 10000 cm^{-1} [1]. As shown in Fig. 2.1, the metallic VO_2 has no phonon modes in the considered infrared region, and the imaginary part of the dielectric function increases with lower frequency towards its plasma frequency.

Electrical permittivity of graphene is obtained by $\varepsilon_G = i\sigma_G / (t_G\omega\varepsilon_0)$ [23, 24, 59], where σ_G is the conductivity of graphene, t_G is the thickness of a single graphene layer, ω is the angular frequency, and ε_0 is the permittivity of vacuum. Note that $t_G = 0.5\,\text{nm}$ is assumed for this proposed research. The conductivity of graphene is acquired by $\sigma_G = \sigma_D + \sigma_I$. Note that σ_D corresponds to the intraband electron-photon scattering, while σ_I is associated with interband electron transition. σ_D and σ_I can be calculated by:

$$\sigma_D = \frac{i}{\omega + i/\tau}\frac{2e^2k_BT}{\pi\hbar^2}\ln\left(2\cosh\left(\frac{\mu}{2k_BT}\right)\right) \tag{2.1}$$

$$\sigma_1 = \frac{e^2}{4\hbar}\left[G\left(\frac{\hbar\omega}{2}\right) + i\frac{4\hbar\omega}{\pi}\int_0^{\infty}\frac{G(\xi) - G(\hbar\omega/2)}{(\hbar\omega)^2 - 4\xi^2}d\xi\right] \tag{2.2}$$

where $G(\xi) = \sinh(\frac{\xi}{k_B T}) / \left[\cosh\left(\frac{\mu}{k_B T}\right) + \cosh\left(\frac{\xi}{k_B T}\right)\right]$. In Eqs. (2.1–2.2), τ is the relaxation time which is chosen as 10^{-13} s, e is the elementary charge, k_B is the Boltzmann's constant, $\hbar$ is the reduced Planck's constant, temperature T is taken as 300 K, and μ is chemical potential of graphene.

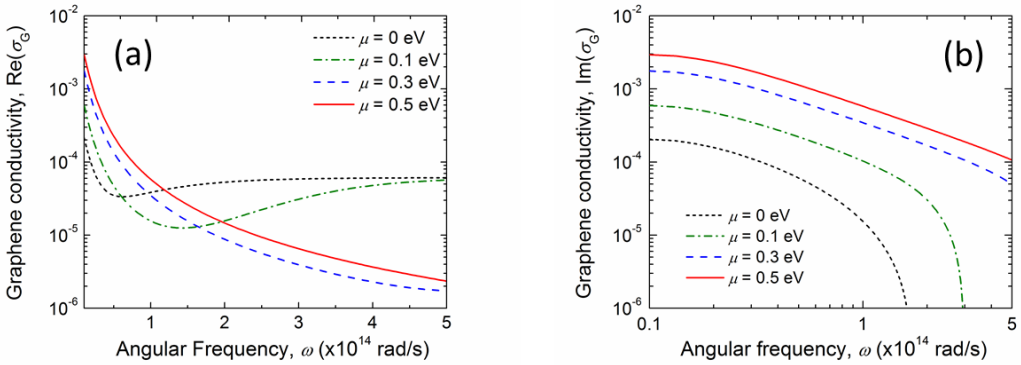

Figure 2.2 (a) Real part and (b) imaginary parts of electrical conductivity of graphene monolayer at different chemical potentials at the temperature of 300 K.

Figure 2.2 shows the real and imaginary parts of graphene electrical conductivity at room temperature. As shown in Fig. 2.2, the amplitude of graphene electrical conductivity σ can be tuned by orders with chemical potential μ. It can be observed from Fig. 2.2(a) that larger chemical potential will introduce a larger real part of the graphene electrical conductivity at lower angular frequency, and a smaller one at higher angular frequency. Note that a larger real part of graphene electrical conductivity indicates a larger imaginary part of graphene electrical permittivity, which means a more lossy

material. However, as presented in Fig. 2.2(b), a larger chemical potential always gives a larger imaginary part of graphene electrical conductivity along the whole spectral range.

2.2 Numerical Methods to Calculate Radiative Properties of Nanostructure

Rigorous coupled-wave analysis (RCWA) is a widely used method to obtain radiative properties of periodic grating nanostructures. The main idea of this method is based on Floquet's theorem that the solutions of periodic differential equations can be expanded with Bloch waves. After multiple scattering in the periodic grating structure, the reflected electromagnetic wave is expanded to a series of diffracted ones with different orders. Assuming a 1D grating periodically arranged in x direction, the x component of the wavevector for jth order $k_{x,j}$ is determined from the Bloch-Floquet condition

$$k_{x,j} = \frac{2\pi}{\lambda}\sin\theta + \frac{2\pi}{\Lambda} j \tag{2.3}$$

where λ is the wavelength, θ is the incident angle, and Λ is the grating period. After matching the boundary conditions at each interface, the reflectance for each diffraction order can be calculated, and the total reflectance is summation of them. RCWA is a well-developed method to calculate radiative properties of periodic grating nanostructures, and the details can be found in Refs. [60-62]. Note that the convergence of RCWA strongly depends on the total diffraction orders, and they have been carefully checked to be sufficient for the following calculations. RCWA is efficient to obtain radiative properties for 1D gratings, but very computationally expensive for 2D gratings and even more complex nanostructures.

The finite-difference time-domain (FDTD) method (Lumerical Solutions, Inc.) is another numerical analysis technique used for solving Maxwell equations in time domain, which was employed to numerically calculate the spectral-directional reflectance R and transmittance T of nanostructures, and the spectral-directional absorptance of the metamaterial structure was obtained as $\alpha = 1-R-T$. Sufficiently fine meshes were used to ensure the numerical convergence. Different boundary conditions, like periodic, Bloch and perfect matched layers, were considered for different cases. One advantage of FDTD method is its generality for various nanostructures, and the time consumed for 2D gratings modelling is much less than that of RCWA.

2.3 Fluctuational Electrodynamics Theory to Calculate Near-Field Radiative Heat Transfer

Fluctuational electrodynamics[63], based on the stochastic nature of thermal emission, was used to calculate the near-field radiative heat fluxes. For the purpose to be general, the radiative heat transfer between a thin film emitter and a thin film receiver with substrates is considered as shown in Fig. 2.3.

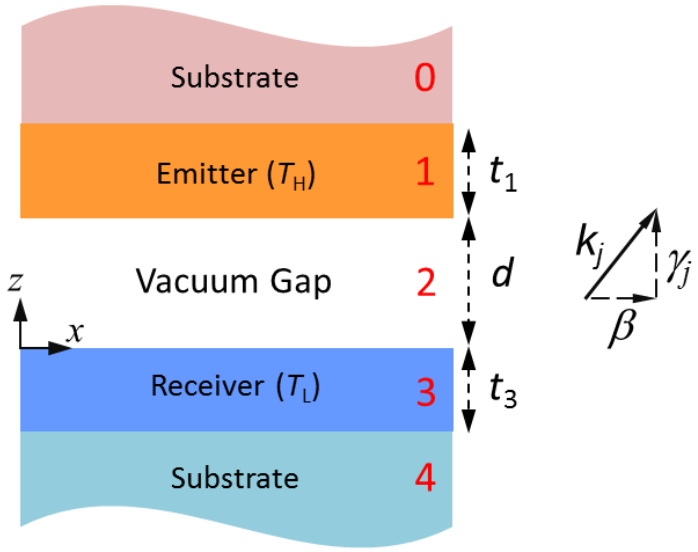

Figure 2.3 Schematic of near-field radiative heat transfer between a thin film emitter and a thin film receiver with substrates, which is separated by a vacuum gap d. The emitting and receiving thin film thicknesses are denoted as t_1 and t_3, respectively. The emitter and receiver temperature are set as T_H and T_L, respectively. The directions of the wavevectors are also shown.

The analytical expression for the radiative heat flux between two thin films with substrates at temperatures of T_H and T_L is [40, 64]

$$q'' = \frac{1}{4\pi^2}\int_0^\infty d\omega\left[\Theta(\omega,T_H)-\Theta(\omega,T_L)\right]\int_0^\infty \xi(\omega,\beta)\beta d\beta \tag{2.4}$$

Here, $\Theta(\omega,T)=\hbar\omega/[\exp(\hbar\omega/k_BT)-1]$ is the mean energy of a Planck oscillator at thermal equilibrium temperature T, where $\hbar$ and k_B are the reduced Planck constant and the Boltzmann constant, respectively. The energy transmission coefficient $\xi(\omega,\beta)$ for propagating waves ($\beta < \omega/c$) and evanescent waves ($\beta > \omega/c$) is different and can be written as

$$\xi_{prop}(\omega,\beta)=\frac{\left(1-\left|R_{210}^{s}\right|^{2}\right)\left(1-\left|R_{234}^{s}\right|^{2}\right)}{\left|1-R_{210}^{s}R_{234}^{s}e^{i2\gamma_2 d}\right|^{2}}+\frac{\left(1-\left|R_{210}^{p}\right|^{2}\right)\left(1-\left|R_{234}^{p}\right|^{2}\right)}{\left|1-R_{210}^{p}R_{234}^{p}e^{i2\gamma_2 d}\right|^{2}} \tag{2.5a}$$

and $$\xi_{evan}(\omega,\beta)=\frac{4\,\mathrm{Im}(R_{210}^{s})\,\mathrm{Im}\left(R_{234}^{s}\right)e^{-2\mathrm{Im}(\gamma_2)d}}{\left|1-R_{210}^{s}R_{234}^{s}e^{i2\gamma_2 d}\right|^{2}}+\frac{4\,\mathrm{Im}(R_{210}^{p})\,\mathrm{Im}\left(R_{234}^{p}\right)e^{-2\mathrm{Im}(\gamma_2)d}}{\left|1-R_{210}^{p}R_{234}^{p}e^{i2\gamma_2 d}\right|^{2}} \tag{2.5b}$$

where β is the parallel-component wavevector, γ is the vertical-component wavevector, $R_{210(234)}$ is respectively the reflection coefficient from the vacuum gap to either emitter (i.e., R_{210}) or to the receiver (i.e., R_{234}), which can be calculated by thin-film optics for both *s* and *p* polarizations [65, 66]

$$R_{234(210)}=\frac{r_{23(21)}+r_{34(10)}e^{i2\gamma_{3(1)}t_{3(1)}}}{1+r_{23(21)}r_{34(10)}e^{i2\gamma_{3(1)}t_{3(1)}}} \tag{2.6}$$

where r_{ij} is the Fresnel reflection coefficient at the single interface from medium *i* to medium *j*, while the subscripts 0, 1, 2, 3, 4 represent the emitter substrate, emitting thin film, vacuum gap, receiving thin film, and receiver substrate, respectively, as indicated in Fig. 2.3. Note that when the thin films (i.e., layer 1 or 3) become semi-infinite, the thin-film reflection coefficient R_{210} (or R_{234}) will be replaced by the reflection coefficient r_{21} (r_{23}) at a single interface. In addition, if the film substrate (i.e., layer 0 or 4) is vacuum, the energy associated with propagating waves will not be absorbed when it transmits into the vacuum substrate. In this case, $(1-\left|R_{ijk}\right|^{2})$ will be replaced by $(1-\left|R_{ijk}\right|^{2}-\left|T_{ijk}\right|^{2})$ in Eq. (2.5a), where T_{ijk} is the transmission coefficient from layer *i* to layer *k* through a thin layer *j*, obtained by thin-film optics [65, 66]

$$T_{234(210)}=\frac{t_{23(21)}t_{34(10)}e^{i\gamma_{3(1)}t_{3(1)}}}{1+r_{23(21)}r_{34(10)}e^{i2\gamma_{3(1)}t_{3(1)}}} \tag{2.7}$$

where t_{ij} is the transmission coefficient at the single interface from medium *i* to medium *j*.

For isotropic emitter and receiver, the reflection coefficient at the emitter-vacuum and receiver-vacuum interface can be calculated by isotropic wave propagation [58]. However, when the emitter or receiver becomes uniaxial, anisotropic wave propagation has to be considered. Taking the same consideration as the structure of nanoporous SiC plate [67], the ordinary component ε_{O} and extraordinary component ε_{E} of dielectric function were used to calculate the reflection coefficient. For s polarized wave, the electric field is always perpendicular to the optical axis, and thus only the ordinary response is considered such that $r_{ij}^{s} = (\gamma_i^{s} - \gamma_j^{s})/(\gamma_i^{s} + \gamma_j^{s})$, $t_{ij}^{s} = 2\gamma_i^{s}/(\gamma_i^{s} + \gamma_j^{s})$, where $\gamma_i^{\mathrm{s}} = \sqrt{\varepsilon_{i\mathrm{O}}(\omega/c)^2 - \beta^2}$ and *i* refers to layer index [58, 67, 68], where the superscript "s" refers to the s-polarization. While for *p*-polarized wave, both ordinary and extraordinary dielectric responses have to be considered since the electrical field would always have components perpendicular to and parallel to the optics axis. The reflection coefficient for *p* polarized waves can be obtained from $r_{ij}^{p} = (\varepsilon_{j\mathrm{O}}\gamma_i^{p} - \varepsilon_{i\mathrm{O}}\gamma_j^{\mathrm{p}})/(\varepsilon_{j\mathrm{O}}\gamma_i^{p} + \varepsilon_{i\mathrm{O}}\gamma_j^{\mathrm{p}})$, and $t_{ij}^{p} = 2\varepsilon_{j\mathrm{O}}\gamma_i^{p}/(\varepsilon_{j\mathrm{O}}\gamma_i^{p} + \varepsilon_{i\mathrm{O}}\gamma_j^{\mathrm{p}})$, where $\gamma_i^{\mathrm{p}} = \sqrt{\varepsilon_{i\mathrm{O}}(\omega/c)^2 - \varepsilon_{i\mathrm{O}}\beta^2/\varepsilon_{i\mathrm{E}}}$ [67, 68]. Note that the expressions are also valid for an isotropic medium, for which ε_{O} and ε_{E} are identical.

CHAPTER 3 FAR-FIELD TUNABLE THERMAL EMISSION

Three main nanostructures are introduced in this chapter for far-field tunable thermal emission. Note that spectral directional emittance is equal to spectral directional absorptance due to Kirchhoff's law, so the discussions below will only focus on thermal emission, which is also applicable for thermal absorption. Firstly, a VO_2-based metamaterial with a VO_2 thin film sandwiched by a periodic one dimensional Au grating and an Au substrate is employed to achieve switchable thermal emission in the mid-infrared. Followed by another VO_2-based metamaterial, which consists of a MgF_2 thin film sandwiched by a periodic one dimensional VO_2 grating and a VO_2 substrate, tunable thermal emission in the mid-infrared is obtained when VO_2 undergoes the phase transition. The third one is to cover a graphene layer on top of a one dimensional SiC grating, and the tunability of spectral emittance comes from the graphene chemical potential variation.

3.1 Switchable Thermal Emission with VO_2-Based Metamaterial

In this work, we propose a switchable metamaterial absorber/emitter by turning on or off the excitation of magnetic resonance using a VO_2 spacer layer upon its phase transition. Figure 3.1(a) depicts the proposed structure, which consists of a 1D gold grating with period Λ = 1 μm, stripe width w = 0.5 μm, and height h = 80 nm on a bottom Au substrate separated by a thin VO_2 spacer layer with thickness d = 80 nm. The bottom Au substrate could be as thin as 100 nm as long as it is optically opaque. Here, the phase transition of VO_2 is driven by a temperature-controlled stage which the structure is

placed upon, while the heating or cooling could be realized by other means in a particular application.

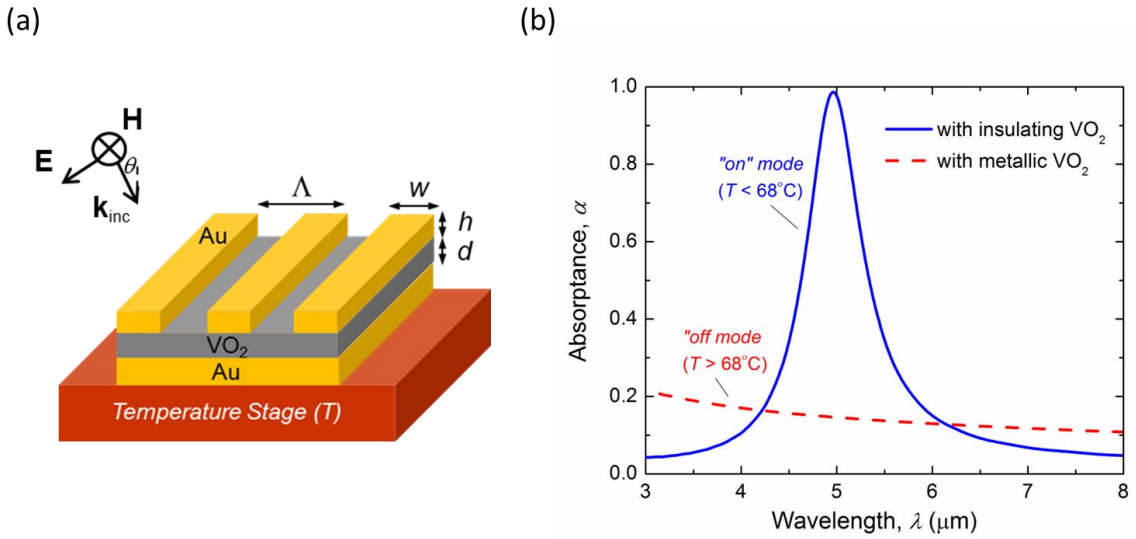

Figure 3.1 (a) Schematic of the proposed switchable metamaterial absorber/emitter made of one-dimensional gold grating (period Λ = 1 μm, strip width w = 0.5 μm, and height h = 80 nm), a thin VO_2 layer (thickness d = 80 nm), and an opaque bottom gold substrate. (b) Spectral absorptance of the switchable metamaterial at normal incidence and TM wave polarization upon phase transition of VO_2 at 68°C, suggesting the "on" and "off" modes.

The finite-difference time-domain (FDTD) method (Lumerical Solutions, Inc.) was employed to numerically calculate the spectral-directional reflectance R, from which the spectral-directional absorptance of the metamaterial structure was obtained as $\alpha = 1-R$. A unit cell with a domain size of 1 μm × 1 μm × 6 μm was simulated, and sufficiently fine meshes were used to ensure the numerical convergence. Periodic boundary conditions were used in both x and y directions at normal incidence, while

Bloch boundary condition was implemented at oblique incidence. Perfectly matched layers with reflection coefficients less than 10^{-6} were applied in z direction. The transverse magnetic (TM) waves, at which the magnetic field **H** is parallel to the grating grooves, were considered here because magnetic resonance can be excited only under this polarization in 1D grating structures [69, 70]. The optical properties of gold were taken from Palik [71]. The dielectric function of the metallic VO_2 was obtained from a Drude model, while the insulating phase was modeled as a uniaxial medium with a dielectric function tensor [1]

$$\bar{\bar{\varepsilon}}_{\text{insulator}} = \begin{pmatrix} \varepsilon_{\text{O}} & 0 & 0 \\ 0 & \varepsilon_{\text{O}} & 0 \\ 0 & 0 & \varepsilon_{\text{E}} \end{pmatrix} \tag{3.1}$$

where ε_{O} and ε_{E} are the ordinary (i.e., when incident electric field is perpendicular to its optical axis) and extraordinary (i.e., when incident electric field is parallel to its optical axis) components, respectively, whose expressions were listed in Section 2.1. Note that, only ε_{O} plays a role at normal incidence, while ε_{E} has to be considered at oblique incidence [72].

Figure 3.1(b) shows the spectral absorptance of the metamaterial structure at normal incidence in the mid-infrared regime from 3 μm to 8 μm in wavelength upon VO_2 phase transition. When the structure temperature is below 68°C, i.e., VO_2 is in the dielectric phase, a large absorption peak occurs with perfect absorption at $\lambda_{\max} = 4.96\,\mu\text{m}$. The full width at half maximum (FWHM) for this peak is $\Delta\lambda$ = 0.72 μm, resulting in a quality factor of 6.89, defined by $Q = \lambda_{\max}/\Delta\lambda$. However, when the

temperature is further increased beyond the phase transition temperature, VO_2 turns into metal and the absorption peak disappears with absorptance less than 0.15 at the same wavelength. The structure essentially becomes reflective in the considered mid-infrared regime. Therefore, simply by controlling the temperature around 68°C, the absorption peak around 5 μm could be turned "on" or "off", suggesting a switchable selective metamaterial absorber upon VO_2 phase transition. It is worth noting that the spectral-directional absorptance is equal to spectral-directional emittance, according to Kirchhoff's law. Therefore, such a metamaterial structure could potentially be a switchable infrared thermal emitter, which would facilitate the applications in space cooling, building energy management, and energy-efficient light sources.

To illustrate the underlying mechanism for the switchable metamaterial absorber/emitter, the electromagnetic field distributions at the peak absorption wavelength $\lambda_{max} = 4.96\,\mu m$ were plotted at the "on" and "off" modes respectively shown in Figs. 3.2(a) and 3.2(b). The cross section of two unit cells was presented with the top gold grating, VO_2 layer and bottom gold film delineated. The arrows represent the electric field vectors, while the background contour indicates the relative strength of magnetic field to the incidence as $\log_{10}|H/H_0|^2$.

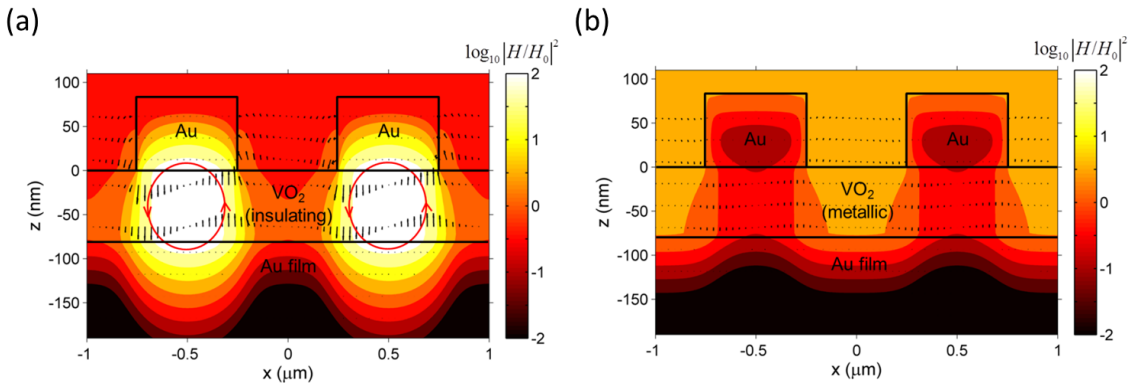

Figure 3.2 Electromagnetic field distributions at the peak wavelength $\lambda_{max} = 4.96\,\mu m$ in the switchable metamaterial with VO_2 in the (a) dielectric phase and (b) metallic phase. The magnetic resonance is excited with dielectric VO_2, resulting in strong field confinement and thus absorption, while it is turned off when VO_2 becomes metallic.

As seen in Fig. 3.2(a), in which the VO_2 is in its dielectric phase, strong magnetic field energy by two orders of magnitude larger than the incidence is localized inside the insulating VO_2 layer between top and bottom gold layers, which is responsible for the strong resonant absorption at this particular wavelength. Moreover, the electric field vectors around the localized magnetic field suggest a current loop. This is the exact behavior when magnetic resonance is excited, which has been previously studied in the similar metamaterial structures with metal-insulator-metal configurations [69, 70, 73, 74].

When magnetic resonance is excited, anti-parallel electric currents are formed around the antinode of the localized magnetic field. The anti-parallel electric currents are due to the non-uniform charge distribution within the metal surfaces at the top and bottom of the dielectric VO_2 spacer. Charges with opposite signs accumulate at the left and right edges of the gold strip and the bottom gold film across the dielectric spacer.

When the VO_2 is a dielectric, the charges form a capacitor C_m between top and bottom metals, while the metals serve as inductors, as illustrated in Fig. 3.3(a). The existence of the capacitor or the insulating VO_2 is critical in this inductor-capacitor (LC) circuit to excite the magnetic resonance at a particular wavelength, which is to be discussed in detail.

However, as shown in Fig. 3.2(b) when the VO_2 becomes metallic, the strong magnetic field confinement disappears, which results in the absorption peak to be switched "off". This can be explained by the fact that the capacitor C_m can be no longer formed when VO_2 is metallic. In other words, the top and bottom metals are shorted by the metallic VO_2 such that charges with opposite signs cannot accumulate across the VO_2 spacer layer to form a capacitor. Without a capacitor, the resonance of an LC circuit cannot be excited.

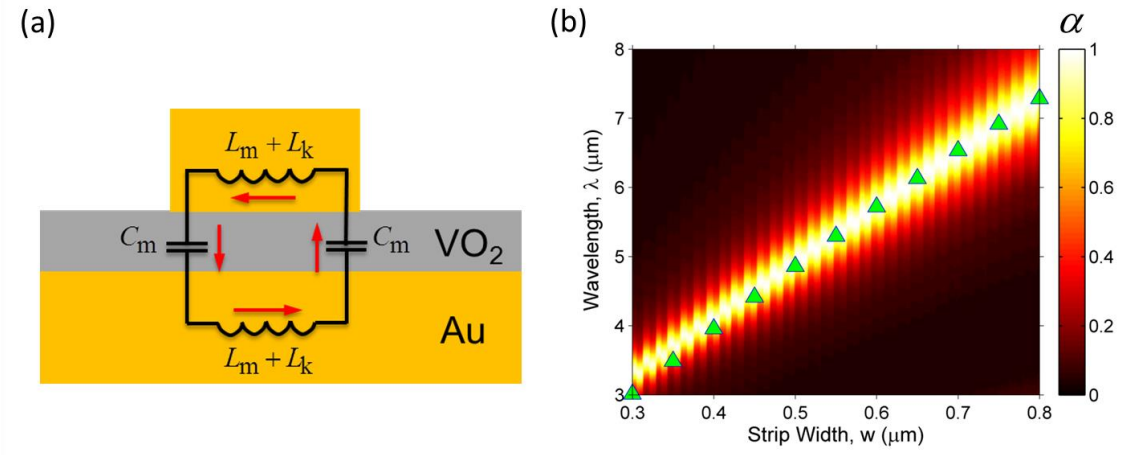

Figure 3.3 (a) Schematic of the LC model that explains the physical mechanism of the switchable absorption peak due to excitation of magnetic resonance upon VO_2 phase transition. (b) Contour plot of normal absorptance as a function of wavelength and strip

width of the switchable metamaterial at the "on" mode. The predicted condition for magnetic resonance from the LC model is shown as triangular markers.

To further explain the underlying physics, detailed analysis with the LC model is presented here. Based on the insights gained from the electromagnetic field distribution on the charge distribution, the top and bottom metals can be treated as inductors, which include two components as mutual inductance L_{m} and kinetic inductance L_{k} per unit length along the grating groove direction with the expressions as [69, 70]

$$L_{\mathrm{m}} = 0.5\mu_0 wd \tag{3.2}$$

$$L_{\mathrm{k}} = -\frac{w}{\omega^2 \varepsilon_0 \varepsilon'_{\mathrm{Au}} \delta_{\mathrm{Au}}} \tag{3.3}$$

where μ_0 is the magnetic permeability of vacuum, ε_0 is the electric permittivity for vacuum, ω is the angular frequency, $\varepsilon'_{\mathrm{Au}}$ is the real part of the permittivity of bulk gold, and δ_{Au} is the penetration depth of bulk gold. The insulating VO_2 spacer helps to form a parallel-plate capacitor C_{m}, which can be expressed as [69, 70]

$$C_{\mathrm{m}} = \frac{c_1 \varepsilon_0 \varepsilon_{\mathrm{d}} w}{d} \tag{3.4}$$

where $c_1 = 0.22$ is the coefficient that accounts for non-uniform charge distribution at the metal surfaces, and ε_{d} is the permittivity of insulating VO_2, which has to be positive. Metallic VO_2 possesses a negative permittivity, which fails to form a capacitor [72]. Magnetic resonance occurs when the impedance of the LC circuit becomes zero, which results in a resonance condition determined by

$$\lambda_{\mathrm{MR}} = 2\pi c_0 \sqrt{(L_{\mathrm{m}} + L_{\mathrm{k}}) C_{\mathrm{m}}} \tag{3.5}$$

For the structure with insulating VO_2 considered in Fig. 1(b), the LC model predicts the magnetic resonance to occur at $\lambda_{MR} = 4.86\,\mu m$, which yields a 2% relative error compared to the FDTD simulation. Similar LC circuit models have been successfully employed to verify the physical mechanism and predict the magnetic resonance conditions in plasmonic metamaterials [75-77]. It is worth mentioning that, there is an additional capacitance, called gap capacitance C_g, which considers the electromagnetic coupling between the neighboring gold strips [69, 70]. However, calculation showed that, C_g is less than 2% of C_m in the present study and thus is reasonably neglected here.

Figure 3.3(b) presents the contour plot of the normal absorptance of the proposed switchable metamaterial as a function of wavelength and strip width when it is at the "on" mode with insulating VO_2. The bright contour band indicates the absorption peak associated with the excitation of magnetic resonance. It is clearly seen that, the resonance peak shifts to longer wavelengths when the strip width increases from 0.3 μm to 0.8 μm, suggesting that the peak could be easily tuned to obtain the selective absorption at desired wavelengths by varying different geometric values during the structure design process, to meet different application needs.

The predicted resonance wavelengths from the LC model were also plotted as triangular makers for comparison, which match well with the resonance band from the FDTD simulation, undoubtedly confirming the underlying physics as magnetic resonance. The geometric dependence of the resonance wavelength is also clearly suggested from the inductance and capacitance expressions. When strip width w increases, L_m, L_k and C_m will become larger according to Eqs. (3.2-3.4), and thereby the resonance wavelength from Eq. (3.5) increases.

The behavior of the switchable metamaterial absorber/emitter at oblique angles is also important for sensing and energy related applications. The absorption or emission associated with excitation of magnetic resonance has been demonstrated with angular independent behaviors, but previously studied metamaterial structures were made of isotropic materials [69, 70, 73]. In our proposed structure, the insulating VO_2 is a uniaxial medium and exhibits anisotropic optical behaviors at oblique incidences. The effect of VO_2 anisotropy on the magnetic resonance and the radiative properties of the switchable metamaterial absorber/emitter need to be studied and understood.

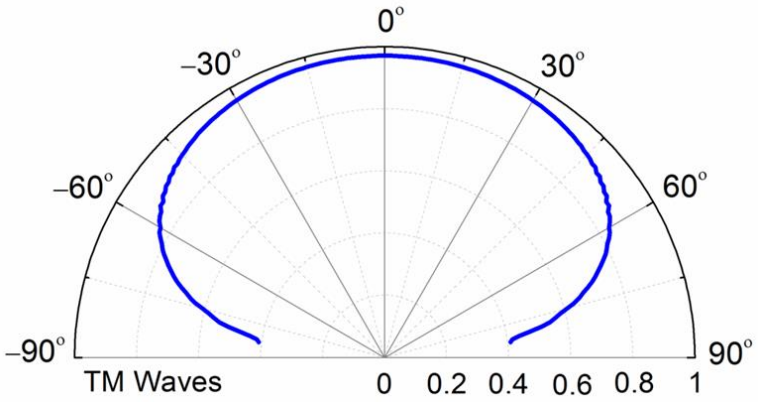

Figure 3.4 Polar plot of the directional absorptance of the switchable metamaterial at the "on" mode with insulating VO_2 as a function of incident angle at the peak wavelength ($\lambda = 4.96$ μm) under TM incidence

Figure 3.4 plots the directional absorptance of the switchable metamaterial with insulating VO_2 at the magnetic resonance wavelength of $\lambda_{max} = 4.96\,\mu m$ in the hemisphere with the incident angle varying from –90° to 90° at TM polarization from the FDTD simulation. The absorptance remains near unity from normal direction to $\theta = 30°$, slightly decreases to 0.83 at $\theta = 60°$, and then drops quickly when it approaches the

grazing angle. Surprisingly, the phase-change metamaterial absorber still exhibits strong diffuse behavior at the absorption peak even though the insulating VO_2 is anisotropic at oblique angles. This can be explained by the insignificant difference between the ordinary and extraordinary dielectric functions of insulating VO_2 [72]. Materials with larger anisotropy like hyperbolic metamaterials might affect more the radiative properties at oblique angles [78].

3.2 Tunable Thermal Emission with VO_2-Based Metamaterial

In this study, we present a tunable infrared metamaterial by exciting magnetic resonance at different conditions with either metallic or dielectric VO_2, leading to highly tunable resonant wavelength upon the phase transition of VO_2. Figure 3.5 depicts the proposed tunable metamaterial structure, which is made of a one-dimensional VO_2 periodic grating structure (period Λ = 1.5 μm and strip width w = 1.25 μm) on stacked MgF_2 and VO_2 film. The thicknesses of the VO_2 grating and thin films are h = 0.5 μm, d_1 = 0.3 μm, and d_2 = 1 μm. In practice, the VO_2 grating could be formed by the strain mismatch method from a VO_2 film on a flexible substrate [79, 80], while the temperature of the structure can be modulated to thermally control VO_2 phase transition.

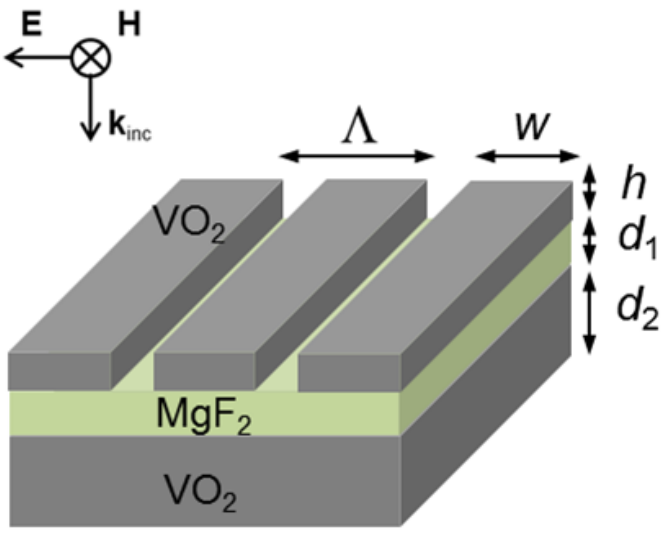

Figure 3.5 Proposed 1D tunable structure with period $\Lambda = 1.5$ μm, strip width $w = 1.25$ μm, layer thicknesses $h = 0.5$ μm, $d_1 = 0.3$ μm, and $d_2 = 1$ μm. The phase transition of VO_2 can be controlled by modulating the temperature.

The finite-difference time-domain method (Lumerical Solutions, Inc.) was used to numerically calculate the spectral reflectance R and transmittance T of the proposed tunable metamaterial above and below the VO_2 phase transition temperature of 68°C. The optical constants of MgF_2 were obtained from Palik's data. A linearly-polarized plane wave was incident normal to the metamaterial structure with transverse-magnetic (TM) incidence, in which magnetic field is along the grating groove direction. Note that magnetic resonance can be excited only at TM polarization in 1D grating based metamaterials [69, 70]. A numerical error less than 2% was verified with sufficiently fine mesh sizes. The spectral normal absorptance in the infrared region was thus obtained by $\alpha = 1-R-T$ based on energy balance.

As shown in Fig. 3.6, when the temperature is above 68°C, the VO_2 is at metallic

phase and the metamaterial exhibits a broad absorption band peaked at the wavelength of 10.9 μm with almost 100% absorption. However, when VO_2 becomes dielectric at temperatures less than 68°C, the absorption band is narrower and shifts to a peak wavelength of 15.1 μm with maximum absorptance of 0.97, resulting in a relative 38.5% peak wavelength shift upon the VO_2 phase transition from metal to dielectric induced thermally. Note that there exist three bumps on the shoulder of absorption peak around 13 μm, 16.5 μm and 19 μm, which are caused by the abrupt change in the optical properties of dielectric VO_2 associated with several phonon absorption modes at these wavelengths.

In fact, both absorption peaks are caused by the excitations of magnetic resonance at both phases of VO_2. But the fundamental difference is that, one is assisted by free charges or plasmon in metallic phase, while the other is mediated by optical phonons in its dielectric phase. The different resonance conditions and thus the resulting large resonance wavelength shift are due to different optical behaviors of different energy carriers that excite the magnetic resonances.

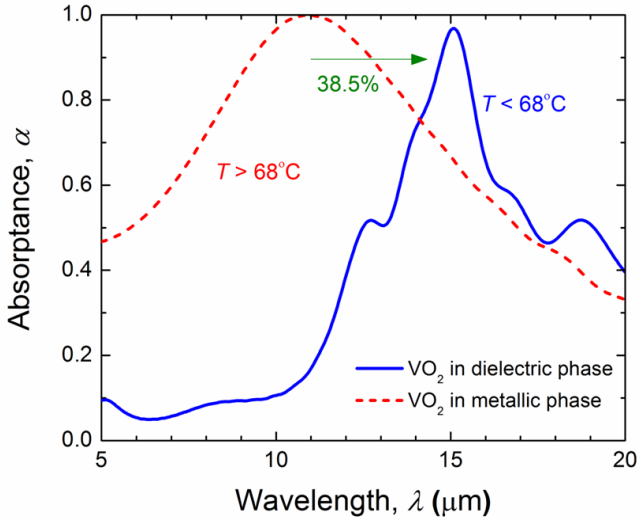

Figure 3.6 Simulated normal absorptance of proposed tunable absorber in the mid-infrared upon VO_2 phase transition, showing a relative 38.5% shift of resonant absorption peak wavelength.

To illustrate the underlying mechanism responsible for the large absorption peaks, electromagnetic field distributions at the cross section of the metamaterial structure were plotted at the resonance wavelengths with metallic and dielectric phases of VO_2, as shown in Figs. 3.7(a) and 3.7(b), respectively. The arrows indicate the strength and direction of the electric field vectors, while the contour shows magnetic field strength normalized to the incidence as $|H/H_0|^2$ at different locations.

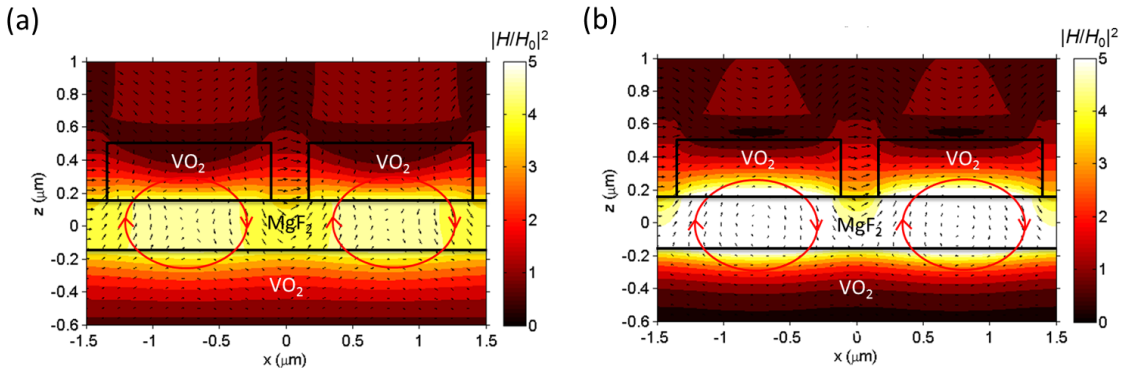

Figure 3.7 Electromagnetic field distribution at resonance peak wavelengths when VO_2 is at (a) metallic or (b) dielectric phase. The field patterns show the exact behavior of magnetic resonance with both phases of VO_2, but assisted by plasmon in metallic VO_2 and mediated by optical phonons in dielectric VO_2, respectively.

When VO_2 is in the metallic phase, the electric field vectors inside the MgF_2 layer underneath the VO_2 strips indicate an anti-parallel current loop, along with the strong

localization of magnetic field, as shown in Fig. 3.7(a). The localized energy is more than five times higher than the incidence. This is the exact behavior of magnetic resonance that has been intensively studied in similar 1D grating based metamaterials [69, 70]. Due to the oscillating movement of free charges in metallic VO_2, the sandwiched MgF_2 layer serves as a capacitor, while top metallic VO_2 strip and the bottom metallic VO_2 film function as inductors, forming a resonant alternating-current circuit. When the magnetic resonance occurs, the external electromagnetic energy at the resonant wavelength of 10.9 μm is coupled with the oscillating plasmon, resulting in almost 100% absorption inside the metamaterial structure.

When VO_2 becomes dielectric with a temperature below 68°C, the electromagnetic field shown in Fig. 3.7(b) presents a similar behavior of magnetic resonance with an induced anti-parallel electric current loop and confined magnetic field inside the MgF_2 layer but at a different resonance wavelength of 15.1 μm. The localized energy strength is about five times to the incidence. Note that, this resonant wavelength is within the phonon absorption band of the ordinary component of dielectric VO_2, in which negative permittivity exists. When optical phonons vibrate at high frequency, the fast movements of bound charges or ions form oscillating electric currents and an inductor-capacitor resonant circuit, resulting in the excitation of magnetic resonance. Since the energy carrier changes from free electrons to optical phonons upon the phase transition of VO_2 from metal to dielectric, a large shift in resonance wavelengths occurs. It should be noted that, similar to the surface phonon polariton with polar materials [7], which is a counterpart of SPP in the infrared regime, phonon-mediated magnetic resonance [81] is the counterpart of magnetic resonance in plasmonic metamaterials made of metallic

nanostructures [69, 70, 73].

Finally, we would like to show that, a hybrid magnetic resonance mode could also occur by the phonon-plasmon coupling from a modified tunable metamaterial by replacing the bottom VO_2 layer with a gold film, as shown in the inset of Fig. 3.8. The period and strip width of the top VO_2 grating are kept unchanged, while the thicknesses of the grating and the MgF_2 spacer layer are $h = d_1 = 0.5$ μm.

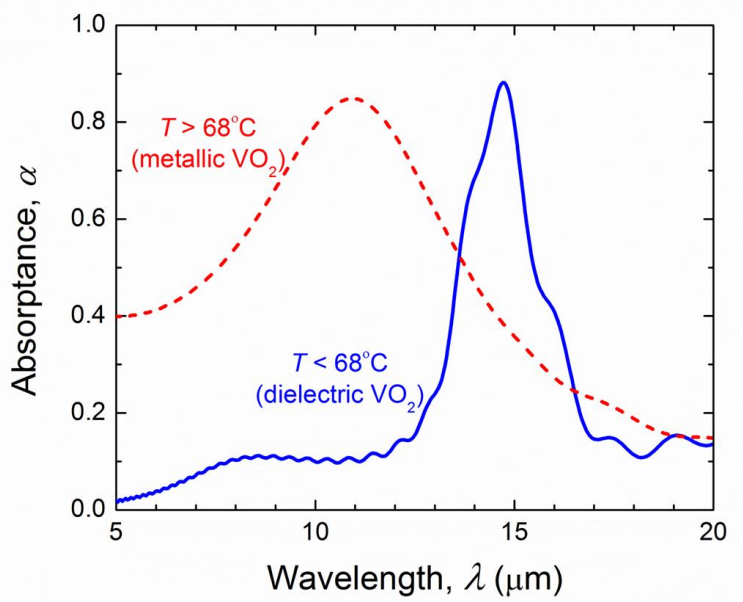

Figure 3.8 Normal absorptance of the tunable structure with gold substrate instead of the bottom VO_2 layer. The absorption peaks still exists because of a hybrid magnetic resonance mode due to phonon-plasmon coupling between top dielectric VO_2 and bottom gold.

The spectral normal absorptance of the hybrid structure is plotted in Fig. 3.8. When VO_2 is in either metallic or dielectric phase, the absorption peaks remain almost at the same resonance wavelengths, suggesting that magnetic resonance can still be excited

in both phases of VO_2. However, maximum absorptance drops slightly to 0.85 for the peak with metallic VO_2, while the absorption peak with dielectric VO_2 becomes narrower, after the bottom VO_2 film was replaced by a gold substrate. The successful excitation of magnetic resonance between metallic VO_2 strips and the bottom gold film is easy to understand, as there exist free charges in both metals. However, the peak absorptance drops because by the plasmonic coupling between metallic VO_2 and Au, whose strength is weaker compared to that between two identical materials with matching plasmonic properties. On the other hand, it would be expected that it would fail to excite phonon-mediated magnetic resonance due to the removal of the bottom VO_2 film. Surprisingly, the strong absorption with dielectric VO_2 could still occur. This can be understood by the excitation of a hybrid magnetic resonance mode due to the strong coupling between optical phonons in dielectric VO_2 and plasmon in the bottom gold substrate. The vibration of optical phonons at high frequency at the top interface of the MgF_2 spacer along with the movement of plasmon at the bottom interface could still form a close-loop inductor-capacitor circuit, which successfully excites magnetic resonance at the wavelength of 14.8 μm. Note that the absorption peak becomes narrower because Au has less intrinsic loss compared with the VO_2 substrate.

3.3 Tunable Thermal Emission with Graphene Covered Metamaterial

In this work, we numerically design an infrared frequency-tunable thermal emitter whose spectrally-selective emission peak can be shifted by varying graphene chemical potential. Figure 3.9 schematizes the proposed tunable metamaterial structure, which is made of a graphene-covered 1D SiC grating array with period Λ = 5 μm, groove width *b*

= 0.5 μm, and grating height h = 1 μm. SiC is chosen as the thermal emitter material due to its excellent high temperature stability. The SiC grating with submicron feature sizes considered here can be practically realized with advanced nanofabrication techniques such as electron-beam lithography or high-throughput low-cost nanoimprint, deep-UV, or laser interference lithography. The graphene layers can be deposited onto the grating layer from chemical vapor deposition. The tunable coherent emission in this study is achieved via the modulation of phonon-mediated MP condition by tuning the optical properties of graphene.

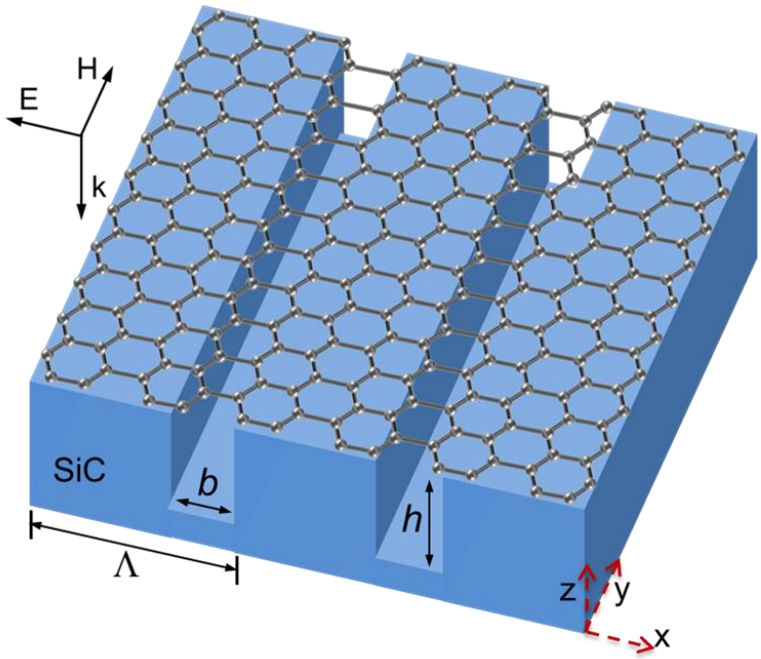

Figure 3.9 Schematic of the proposed tunable IR coherent emitter made of graphene-covered SiC gratings.

3.3.1 Tunable spectral normal emittance with varying graphene chemical potential

The spectral emittance at normal direction for transverse-magnetic (TM) polarized wave (i.e., magnetic field is along the grating groove) is plotted in Fig. 3.10 with varying graphene chemical potential μ. For the bare SiC grating without graphene layer on top, there exists a temporally-coherent emission peak at ν_{res} = 853 cm^{-1} with an peak emittance of 0.73. As studied by Ref. [81], this coherent emission peak is caused by the excitation of phonon-mediated MP inside the SiC grating structure, realized by the collective oscillation of optical phonons or bound charges at the magnetic resonance that form resonant inductor-capacitor (LC) circuitry. The physical mechanism of MP and resulting coherent emission behaviors in the bare SiC gratings have been thoroughly discussed in Ref. [81].

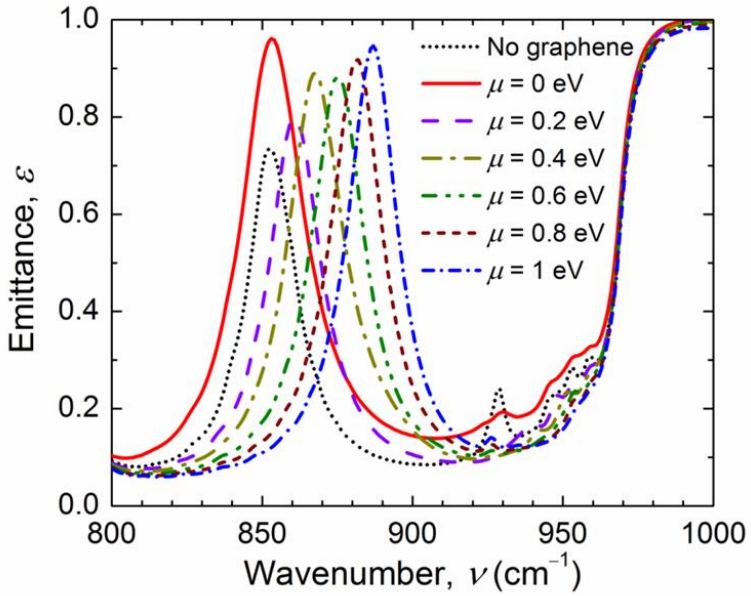

Figure 3.10 Spectral normal emittance of the tunable coherent emitter at different graphene chemical potentials for TM polarized wave. The geometric parameters for the SiC grating are Λ = 5 μm, b = 0.5 μm, and h = 1 μm.

When a graphene sheet with a chemical potential μ = 0 eV is coated onto the SiC grating, the emission peak location barely shifts, but peak emittance increases to 0.96, close to the blackbody emission. When the graphene chemical potential μ increases from 0 to 1 eV, the emission peak frequency ν_{res} monotonically shifts from 853 cm^{-1} to 887 cm^{-1}, resulting in a relative tunability of 4% in peak frequency. As summarized in Table 1, the quality factor $Q = \nu_{res} / \Delta\nu$ for the emission peaks varies from 31.6 to 42.2 with different μ values, where $\Delta\nu$ is the peak full width at half maximum.

Chemical potential (eV)	**0**	**0.2**	**0.4**	**0.6**	**0.8**	**1**
Quality factor	31.6	39.1	36.1	39.8	40.1	42.2
Peak frequency from RCWA, ν_{res} (cm^{-1})	853	861	868	875	882	887
MP frequency from LC model, ν_{LC} (cm^{-1})	841	850	862	874	886	897

Table 3.1 Quality factor for coherent emission peaks with different graphene chemical potential. Resonance frequency obtained from RCWA calculation and LC model are also presented.

3.3.2 Electromagnetic field distribution with and without monolayer graphene at MP resonances

To explain underlying mechanism responsible for the effect of graphene layer on the coherent emission peak, the electromagnetic (EM) field distributions are plotted for SiC grating structures without and with graphene (μ = 0 eV) respectively in Figs. 3.11(a) and 3.11(b) at the same MP resonance frequency ν_{res} = 853 cm^{-1}. In the EM field plots, arrows indicate the strength and direction for electric field vectors, while contour

represents the intensity of magnetic field normalized to the incident wave as $\log_{10}\left|H/H_o\right|^2$. Note that the EM field distributions are presented at the cross section of the 1D SiC grating, i.e., the x-z plane.

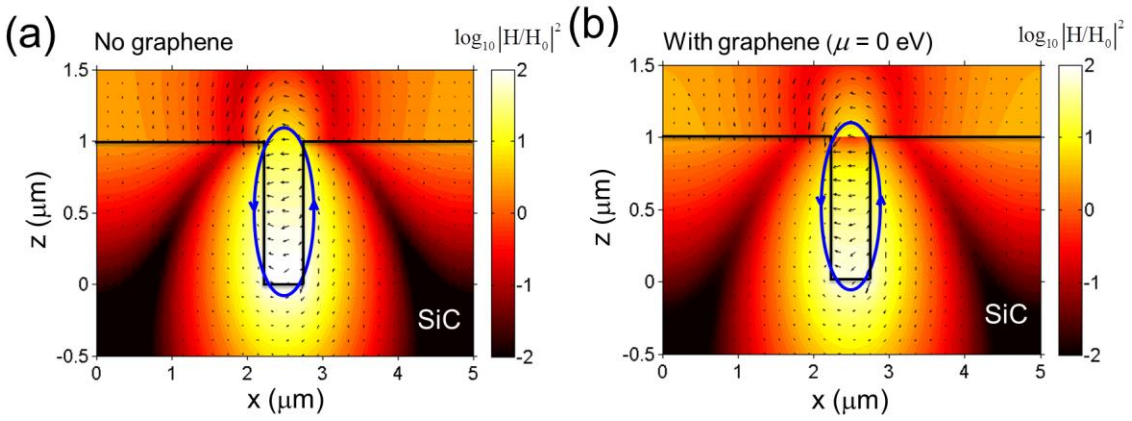

Figure 3.11 Electromagnetic fields at MP resonance frequency of ν_{res} = 853 cm^{-1} for SiC grating (a) without graphene and (b) with monolayer graphene at chemical potential μ = 0 eV. The geometric parameters for the SiC grating are Λ = 5 μm, b = 0.5 μm, and h = 1 μm.

Figure 3.11(a) illustrates the EM field distribution for SiC grating without the graphene sheet at resonance frequency ν_{res} = 853 cm^{-1}. It is observed that the electric current oscillates near the surface of SiC around the grating groove, forming a resonant current loop. The magnetic field is significantly enhanced within the groove, with a magnitude of 2 orders stronger than incidence. The EM field pattern presented in Fig. 3.11(a) distinctly shows the behavior of phonon-mediated MP [81], at which vibration of optical phonons or bound charges in SiC resonates with incident EM field. The resonance

induces an oscillating current with significantly enhanced magnetic field inside, and the emission peak arises as a consequence of this diamagnetic response.

Figure 3.11(b) shows the EM field in the SiC grating structure coated by a monolayer graphene sheet with $\mu = 0$ eV at same resonance frequency. It can be found that the resonant current loop is also excited, within which the magnetic field is still confined but a little bit weaker inside the grating groove in comparison to that in Fig. 3.11(a) without graphene monolayer. This is because the graphene sheet is lossy and more optical energy is absorbed by graphene at magnetic resonance. Although a free-standing graphene monolayer has a small absorption of 3% or so in the infrared, it could absorb much more when strongly enhanced EM field more than the incidence impinges on the graphene due to the strong localization of electromagnetic energy at magnetic resonance. As absorption is enhanced with graphene-covered SiC grating at the MP resonance, the thermal emission is equivalently strengthened according to the Kirchhoff's law under local thermal equilibrium than the case without graphene. This observation and explanation is also consistent with the study by Zhao et al [82] on the enhanced absorption of a graphene monolayer in the near-infrared due to the magnetic resonance excited inside the cavity of metallic gratings.

3.3.3 LC circuit model

As observed in Fig. 3.11, when MP resonance is excited in the graphene-covered grating, a resonant current is induced at the surfaces around the groove, which can be symbolized by an LC circuit, as shown in Fig. 3.12(a). The inductance of SiC is

determined by $L_{\mathrm{SiC}} = L_{\mathrm{k}} + L_{\mathrm{m}}$, where L_{k} and L_{m} are respectively the kinetic and mutual parts with expressions as [81]:

$$L_{\mathrm{k}} = -\frac{h'}{\varepsilon_0 \omega^2 \delta} \frac{\varepsilon'_{\mathrm{SiC}}}{(\varepsilon'^2_{\mathrm{SiC}} + \varepsilon''^2_{\mathrm{SiC}})} \tag{3.6}$$

$$L_{\mathrm{m}} = -\mu_0 h(b + \delta) \tag{3.7}$$

Note that $\delta = \lambda / 4\pi k$ is the penetration depth of SiC, where λ is the wavelength in vacuum and k is the extinction coefficient of SiC. h' is the effective path length that the current flows at the SiC surface. $\varepsilon'_{\mathrm{SiC}}$ and $\varepsilon''_{\mathrm{SiC}}$ are real and imaginary parts of permittivity of bulk SiC. μ_0 is the vacuum permeability. It should be mentioned that the resonant current is not only oscillating at the very surface of SiC but within a depth of δ. Therefore, we consider that the current oscillates in the central plane with a distance of $\delta/2$ away from SiC surface, which yields $h' = 2h + b + 2\delta$. The vacuum gap in the groove forms a capacitor with capacitance $C_{\mathrm{gap}} = c_1 \varepsilon_0 h / b$, where c_1 is the coefficient responsible for the non-uniform charge distribution inside the capacitor [81]. Note that, both the effective path length h' and the factor c_1 might vary with different geometric parameters and numbers of graphene layers, and thus their expression and values are approximations. $c_1 = 0.5$ is taken as a nominal value considering that the bound charges are linearly distributed at the SiC surfaces and thus treated constant in the present study.

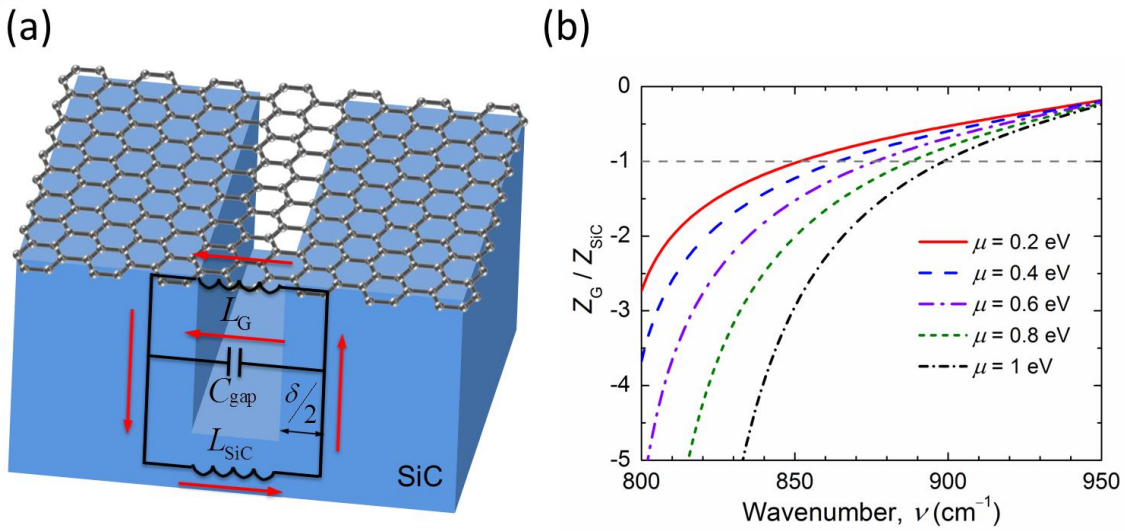

Figure 3.12 (a) Schematic for the LC circuit model that predicts MP resonance frequency. (b) Value of Z_G / Z_{SiC} in the LC circuit with different graphene chemical potentials.

When a graphene layer is attached to the SiC grating, an inductor L_G associated with the graphene sheet should be considered due to the kinetic energy of graphene plasmon. Following the kinetic inductance of SiC in Eq. (3.6), the inductance of monolayer graphene can be modelled as:

$$L_G = \frac{b+\delta}{\omega} \frac{\sigma_G''}{(\sigma_G'^2 + \sigma_G''^2)} \tag{3.8}$$

where σ_G' and σ_G'' are respectively real and imaginary parts of the graphene conductivity. As shown in Fig. 3.12(a), the graphene inductor L_G is in parallel with C_{gap}. Therefore, the total impedance of the LC circuit becomes:

$$Z_{Total} = Z_{SiC} + Z_G = i\omega L_{SiC} + \frac{i\omega L_G}{1-\omega^2 L_G C_{gap}} \tag{3.9}$$

The phonon-mediated MP is excited when $Z_{\text{Total}} = 0$, which leads to maximum resonance strength. All the inductance, capacitance, and impedance are defined on the per unit length basis along the groove direction. Note that when $\mu = 0$ eV, the graphene has positive real part of permittivity at frequencies larger than 898 cm^{-1}. In this case, the graphene sheet cannot be considered as an inductor but a capacitor instead [83].

The resonance frequency ν_{LC} predicted by the LC model is calculated for graphene-covered SiC grating structures with μ varying from 0 to 1 eV. The comparison to the numerical results from the RCWA calculation shows reasonable prediction by the analytical LC model on the MP resonance frequency with a relative difference less than 1.5%. The good agreement on the resonance frequencies of the tunable coherent emission peak between the LC model and RCWA calculation is summarized in Table 3.1, which undoubtedly confirms the excitation of MP and the dependence of MP frequency on the graphene chemical potential for the novel graphene-covered tunable coherent thermal source.

The tuning effect of graphene chemical potential on the coherent emission frequency associated with MP can be further understood from the LC model. The graphene inductance L_{G} is strongly dependent on μ, which would ultimately modulate the MP resonance frequency at zero total impedance with $Z_{\text{G}} / Z_{\text{SiC}} = -1$ indicated by Eq. (8). To quantitatively explain the increase in resonance frequency with larger graphene chemical potentials, the value of $Z_{\text{G}} / Z_{\text{SiC}}$ is plotted in Fig. 3.12(b) with different μ values. Note that only Z_{G} changes with graphene chemical potential, while Z_{SiC} is independent on μ. It is observed that since Z_{G} and Z_{SiC} are comparable, the change of Z_{G} induced by

varying μ will greatly shift the MP resonance frequency. It is also found that Z_G / Z_{SiC} decreases with increased μ. Therefore, the resonance frequency of coherent emission peak at which $Z_G / Z_{SiC} = -1$ increases with larger μ values.

3.3.4 Geometrical dependence of coherent emission from graphene-covered SiC gratings

In light of structural design for practical applications with specific requirement on the coherent emission peak location and strength, the effect of geometric parameters on the coherent emission of the graphene-covered SiC grating is investigated. Figures 3.13(a), 3.13(b) and 3.13(c) are respectively the contour plots of spectral normal emittance as a function of grating height (h), groove width (b), and grating period (Λ) at TM waves obtained from RCWA calculation. The graphene chemical potential is fixed at μ = 0.5 eV, and the geometric parameters of the SiC grating are kept at the base values (i.e., Λ = 5 μm, b = 0.5 μm, and h = 1 μm). As shown in Fig. 3.13(a), when grating height h increases from 0.5 μm to 1.5 μm, the MP resonance peak frequency decreases from ν_{res} = 910 cm^{-1} to 834 cm^{-1}. This is because that, deeper grating grooves with larger h values yield increased C_{gap} and $|L_{SiC}|$, which results in increased Z_G / Z_{SiC} values according to the LC model.

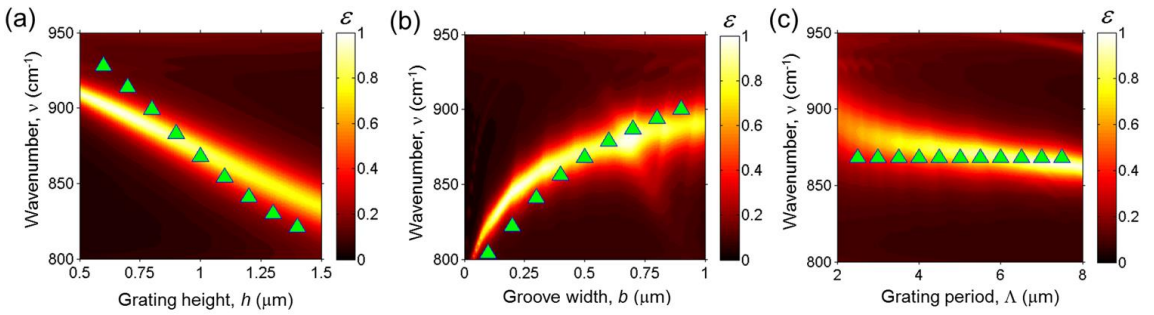

Figure 3.13 Geometric effects of (a) grating height h, (b) groove width b, and (c) grating period Λ on the spectral normal emittance of graphene-covered SiC gratings at TM waves. The graphene chemical potential is fixed at μ = 0.5 eV. The predicted MP resonance frequencies from the LC circuit model are also plotted as green triangles for comparison with RCWA simulation.

Different from the effect of grating height, the MP resonance frequency monotonically increases from ν_{res} = 820 cm^{-1} to 891 cm^{-1} when the groove width b increases from 0.1 μm to 1 μm as presented in Fig. 3.13(b). The effect of groove width b on the MP resonance frequency can be explained by the decrease of Z_G / Z_{SiC} values as C_{gap} decreases with b. However, the variation of grating period almost does not affect the resonance frequency as shown in Fig. 3.13(c), simply because grating period has no effect on the MP resonance frequency according to the LC circuit model. The resonance frequencies predicted by LC circuit model for different grating geometries are also plotted as the green triangles, and the good agreement between LC circuit model prediction and RCWA simulation clearly confirms the geometric effects on the MP resonance condition and underlying physical mechanisms. The geometric dependence of the coherent emission from the graphene-covered SiC gratings would also provide

guidelines for balancing optimal performance from materials design and manufacturing tolerance in fabrication processes.

3.3.5 Angular dependence of coherent emission from graphene-covered SiC gratings

As studied previously, coherent emission due to MP resonance in bare 1D SiC grating structures exhibit directional independence [81]. Therefore, it is worthwhile to investigate the angular behavior and possibly confirm the unique omni-directional thermal emission associated with MP resonance when a graphene monolayer is coated onto bare SiC gratings. Figure 3.14 plots the spectral emittance of graphene-covered SiC gratings as a function of wavenumber ν and in-plane wavevector $k_{x0} = (\omega/c_0)\sin\theta$, where θ is the angle of incidence. The graphene chemical potential is $\mu = 0.5$ eV, and the grating geometry is set as $h = 1$ μm, $b = 0.5$ μm, and $\Lambda = 5$ μm. TM-wave polarization is considered here, only in which the MP could be excited in 1D gratings [81]. A flat selective emission band around $\nu_{res} = 873$ cm^{-1} is observed in the contour plot, whose physical mechanism is verified as MP resonance by excellent match with the LC model prediction in green triangles (i.e., $\nu_{LC} = 868$ cm^{-1} for selected angles from 0° to 80°. Therefore, it is confirmed from both numerical simulation and analytical model that, the tunable spectrally-selective thermal emission from the graphene-covered SiC grating also exhibit strong directional independence, which is highly favorable for some applications that require diffuse-like infrared thermal sources.

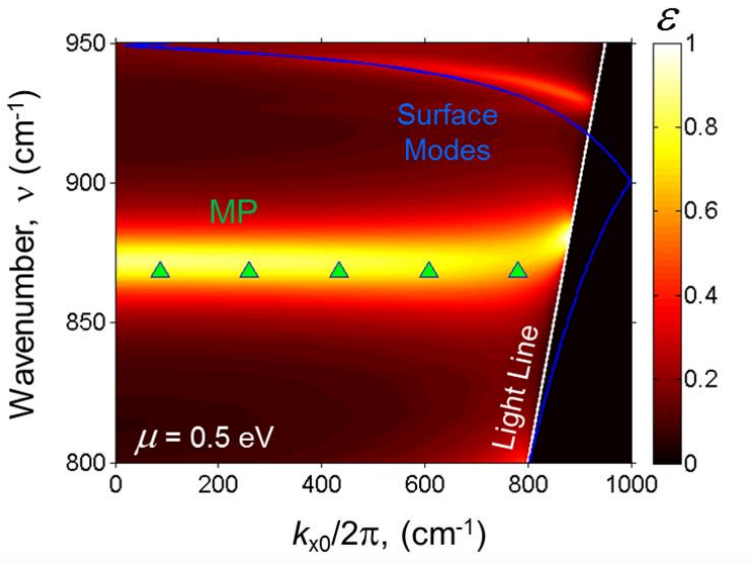

Figure 3.14 Contour plot of the spectral-directional emittance of graphene-covered SiC gratings as a function of wavenumber ν and in-pane wavevector k_{x0}. The parameters are set as h = 1 μm, b = 0.5 μm, Λ = 5 μm, and μ = 0.5 eV. The MP resonance frequency is also predicted by the LC circuit model (denoted by green triangles), and the dispersion curve of the surface modes at the vacuum-graphene-SiC interface is also plotted (as blue curves).

Besides, there exists a relatively weaker resonance band at higher frequencies, which is associated with the surface modes excited at the vacuum-graphene-SiC grating interface. The dispersion relation of the surface modes can be solved via zeroing the reflection coefficient at the interface given by [23, 55]

$$r^p = \frac{\varepsilon_1\gamma_0 - \gamma_1 + \sigma_G\gamma_0\gamma_1/(\omega\varepsilon_{00})}{\varepsilon_1\gamma_0 + \gamma_1 + \sigma_G\gamma_0\gamma_1/(\omega\varepsilon_{00})} \tag{3.10}$$

where the subscripts "0" and "1" represent vacuum and SiC medium, respectively. σ_G is the graphene conductivity described above. Here, graphene is treated as a sheet current

added to the vacuum-SiC interface. ε_{00} is the absolute dielectric function of vacuum. $\gamma_j = \sqrt{\varepsilon_j \omega^2 / c_0^2 - k_{xi}^2}$ is the wavevector component vertical to the interface in medium j = 0 or 1. According to the grating function, $k_{xi} = k_{x0} + i2\pi/\Lambda$, where i is the diffraction order. By folding at $k_{x0} = 1/2\Lambda$, i.e., 1000 cm^{-1} for Λ = 5 μm, the dispersion curve of the surface modes is plotted in Fig. 3.14, which shows good agreement with the RCWA calculation. Note that the resonance frequencies of the surface modes are highly dependent on k_{x0} or incidence angle θ, which exhibits different behaviors from the direction-independent MP resonance mode.

3.3.6 Multilayer graphene effect on tunable coherent emission

In order to possibly achieve a larger tunability for resonance frequency, radiative properties of SiC gratings covered by multiple graphene sheets are further explored. The geometric parameters of SiC gratings are Λ = 5 μm and b = 0.5 μm, while grating height h is changed from 1 μm to 1.5 μm in order to shift the MP resonance frequency at μ = 0 eV to the lower phonon band edge of SiC. In this way, it is attempted to further tune the emission peak to cover most of the phonon absorption band of SiC. The contour plots in Fig. 3.15 display the calculated spectral normal emittance as a function of μ from RCWA for the SiC gratings covered with 1, 2, 3 and 4 layers of graphene sheets.

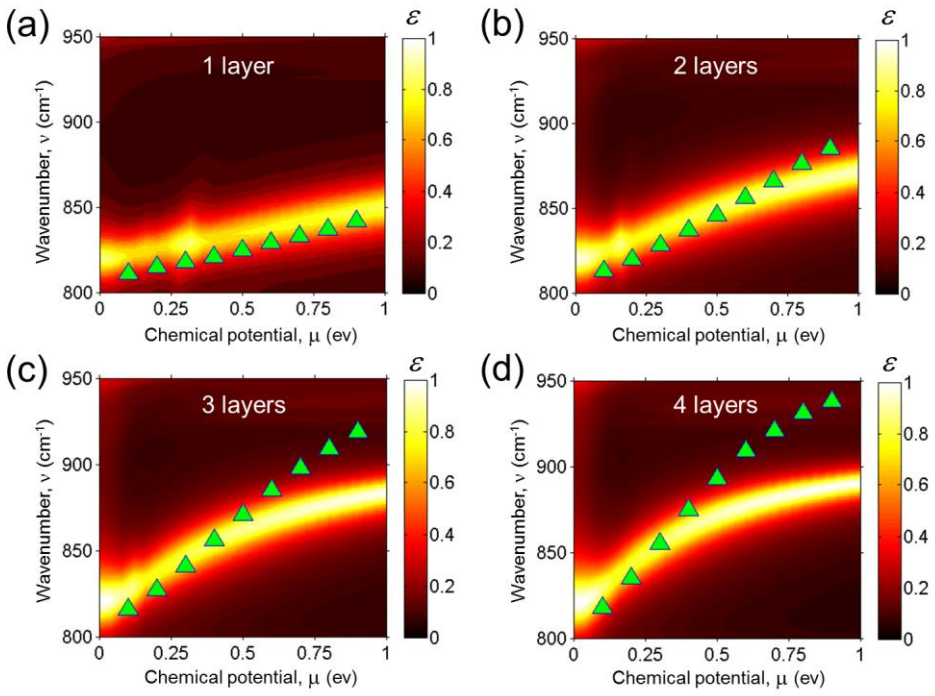

Figure 3.15 Spectral normal emittance at TM waves as a function of graphene chemical potential μ for SiC gratings covered by (a) a single graphene sheet, (b) 2 layers, (c) 3 layers, and (d) 4 layers of graphene sheets. The geometric parameters for the SiC grating are Λ = 5 μm, b = 0.5 μm, and h = 1.5 μm.

It can be observed that, as the number of graphene layer increases, the tunable spectral range of selective emission peaks increases. Specifically, compared to a monolayer graphene sheet with a tunable range from 820 cm^{-1} to 850 cm^{-1} in Fig. 3.15(a), double, triple, and quadruple layers of graphene sheets lead to a higher upper limit of the resonance frequencies associated with MP at μ = 1 eV (i.e., 870 cm^{-1}, 884 cm^{-1}, and 890 cm^{-1}, respectively). The lower limit of resonance frequency at μ = 0 eV barely changes with more graphene sheets. As a result, the tunability of the peak emission frequency is improved from 3.7% to 6.1 %, 7.8 %, and 8.5% when the number of graphene sheets on top of the SiC grating is increased from 1 to 4. Besides, the resonance

emission band tends to slightly broaden due to the increased loss with the additional graphene sheets.

The effect of multilayer graphene in further tuning the emission frequency could be understood with the help of the LC model. To account for the effect of multiple graphene sheets coated on top of the SiC gratings, the inductance for multilayer graphene sheets with a total of m layers becomes $L_{\mathrm{G},m} = L_{\mathrm{G}}/m$, where L_{G} is the inductance of monolayer graphene given by Eq. (3.8). Here we neglect the inter-coupling between graphene monolayers for simplicity. The impedance of the multiple graphene sheets is then:

$$Z_{\mathrm{G},m} = \frac{i\omega L_{\mathrm{G}}}{m - \omega^2 L_{\mathrm{G}} C_{\mathrm{gap}}} \tag{3.11}$$

It can be inferred from Eq. (3.11) that $\left|Z_{\mathrm{G},m}\right|$ increases with larger m, given the fact that $m - \omega^2 L_{\mathrm{G}} C_{\mathrm{gap}}$ is negative in the considered spectral range. When larger $\left|Z_{\mathrm{G},m}\right|$ becomes more dominant over Z_{SiC} in the total impedance as $Z_{\mathrm{Total}} = Z_{\mathrm{SiC}} + Z_{\mathrm{G},m}$, the larger variation of $\left|Z_{\mathrm{G},m}\right|$ with multiple graphene sheets will consequently lead to a larger shift of resonance frequency than that with a single layer graphene. The predicted MP resonance frequencies from the LC circuit model at different chemical potentials are presented in Fig. 7 for graphene sheets with different layers. Excellent agreement of the tunable MP resonance frequencies between the RCWA calculations and the analytical LC prediction can be clearly observed. However, when the number of graphene layers further increases, the resonance frequency at large graphene chemical potentials from the RCWA calculation tends to saturate around $\nu = 900$ cm^{-1}, which deviates from the LC prediction

at higher resonance frequencies. This is because, in graphene-covered SiC grating microstructures, grating-coupled surface modes existing at the air-graphene-SiC interface are mediated by both the graphene plasmon and optical phonons of SiC at high frequencies from ν = 925 cm^{-1} to 1000 cm^{-1}. Therefore, the graphene-tuned MP resonance frequency is suppressed when it approaches the strong surface modes at higher frequencies with larger μ, resulting in altered MP resonance frequencies away from the prediction by the LC model. Note that the simple LC model could not consider the interaction effect between the surface modes and MP resonances.

To further understand the multilayer graphene effect on the MP resonance inside the SiC grating, EM fields are calculated for graphene sheets with different layer numbers at respective MP resonance frequencies, as presented in Fig. 3.16. The geometric parameters of the SiC grating are the same with those for Fig. 3.15, while the graphene chemical potential is fixed at μ = 0.5 eV, for which the MP is excited respectively at ν = 835 cm^{-1}, 850 cm^{-1}, 862 cm^{-1}, or 871 cm^{-1} for 1, 2, 3 or 4 layers of graphene sheets, as indicated in Fig. 3.15.

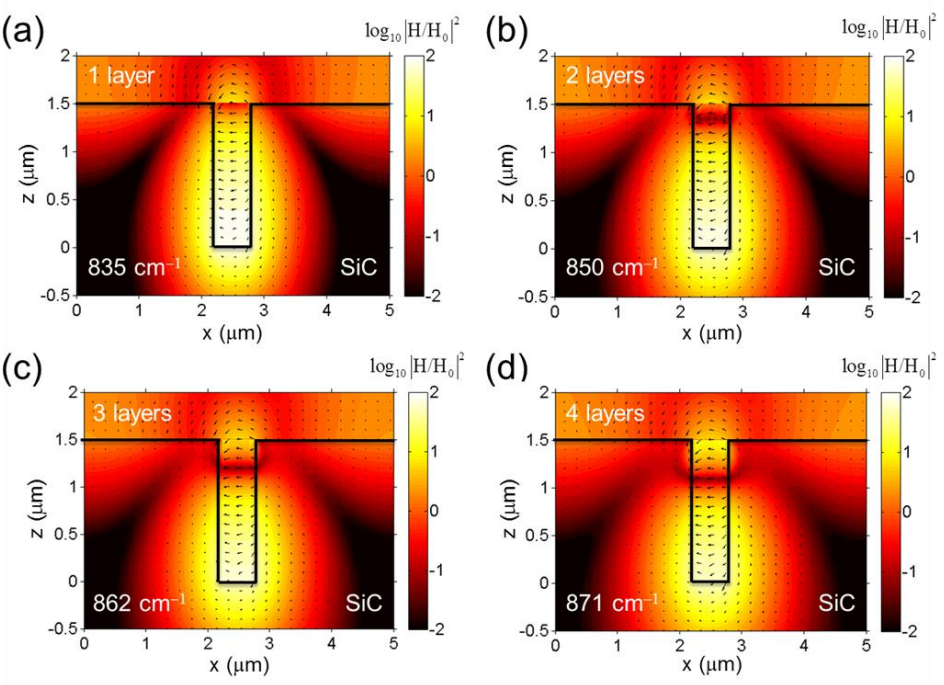

Figure 3.16 Electromagnetic fields at respective MP resonance frequency for SiC gratings coated by multiple graphene layers with (a) a single graphene sheet at ν_{res} = 835 cm^{-1}, (b) 2 layers at ν_{res} = 850 cm^{-1}, (c) 3 layers at ν_{res} = 862 cm^{-1}, and (d) 4 layers at ν_{res} = 871 cm^{-1}. The geometric parameters for the SiC grating are Λ = 5 μm, b = 0.5 μm, and h = 1.5 μm. The graphene chemical potential is μ = 0.5 eV.

When graphene layer number increases, it can be observed that the H field strength (shown as contour) around the graphene sheets becomes stronger and decays further into the SiC groove. This is because at the chemical potential μ = 0.5 eV, graphene acts as an inductor with negative ε within the phonon absorption band of SiC. As the number of graphene layers increases, larger electrical conductance will result in stronger electrical currents, which leads to stronger H field strength decaying further away from the graphene sheets. On the other hand, the strength of H field confined inside the groove becomes weaker with more graphene layers, due to the fact that less energy can penetrate into the groove with thicker conductive, i.e., more lossy, graphene sheets.

Figure 3.16 clearly illustrates the electromagnetic interaction between multiple graphene layers and the MP excited inside the grooves of SiC gratings. The EM field obtained from the RCWA simulation shows consistency with the LC circuit model depicted in Fig. 3.12(a) with graphene sheets as an inductor.

3.4 Experimental Demonstration of MP in 2D SiC Gratings

3.4.1 Sample fabrication and SEM image of 2D SiC gratings

A few theoretical studies have been conducted to show coherent emission or transmission by exciting MP in polar materials [81, 84, 85]. However, none of the experimental work has been reported. To demonstrate the existence of MP in polar materials in practice, 2D SiC gratings were fabricated via focused ion beam technique and the SEM images are shown in Fig. 3.17. The fabrication started with a 340-μm-thick, double side polished crystalline SiC-6H film, and the size is 1 inch by 1 inch. A clear sample image needs to be obtained at first under electron beam by tuning the sample position, tilting angle, lens focus and light contrast. The focused ion beam with beam current of 1 nA and the voltage of 30 kV was then applied to etch the 2D grating patterns on the surface of the SiC film. The magnification was 2000×, and the processing time was controlled to obtain different grating depth.

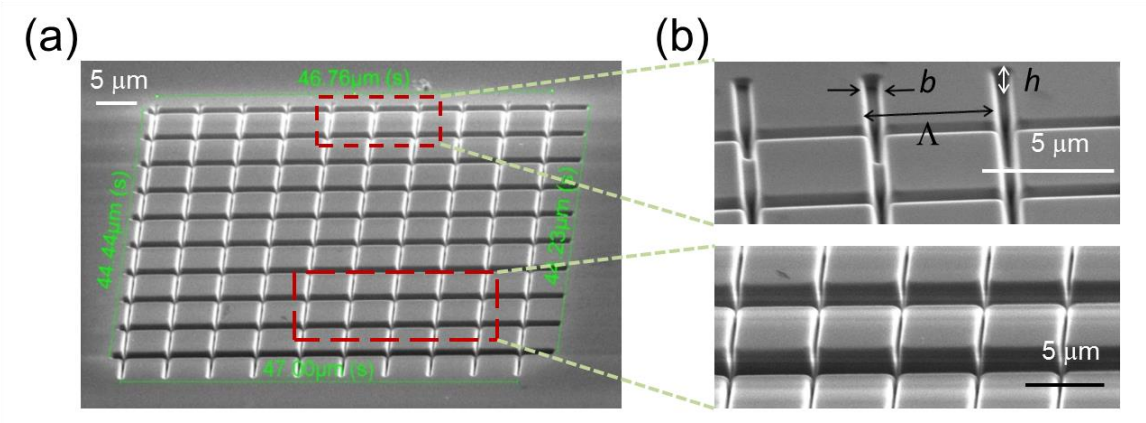

Figure 3.17 (a) SEM image of a 2D SiC grating pattern fabricated by focused ion beam technique on the surface of a thick SiC film. (b) The close-up SEM images of the pattern edge and center areas. The SiC grating geometry parameters of period (Λ), depth (*h*) and slit width (*b*) are presented as well.

As shown in Fig. 3.17(a), the size for one grating pattern is around 45 μm × 45 μm with nine periods at each direction with symmetry along both directions. The grating pattern has three geometry parameters of period (Λ), slit width (*b*) and depth (*h*) as presented in Fig. 3.17(b), all of which were measured at different locations and then averaged to obtain the grating dimension. In order to investigate the grating geometry effect on the MP resonance, three different grating patterns were fabricated. Pattern 1 has the geometry of Λ = 5.20 μm, *b* = 0.41 μm, *h* = 1.15 μm, and pattern 2 has Λ = 5.20 μm, *b* = 0.37 μm, *h* = 1.26 μm, while pattern 3 is equipped with multiple depths of Λ = 5.20 μm, *b* = 0.40 μm, h_1 = 0.68 μm, h_2 = 1.10 μm, h_3 = 1.50 μm. Note that the SEM images shown in Fig. 3.17 is for pattern 3 with multiple grating depths.

3.4.2 Optical properties measurement in infrared region

After sample fabrication, the optical properties including spectral reflectance and transmittance were characterized by the iS50 Fourier transform infrared (FT-IR) spectrometer as shown in Fig. 3.18(a). The FT-IR bench is used to measure the optical properties of samples in mm or cm sizes. Due to the small size of SiC grating patterns around 45 μm × 45 μm, the FT-IR microscope, which could measure the sample as small as 30 μm × 30 μm, was used to measure the spectral reflectance and transmittance. The light spot needs to be focused on the sample surface and shrunk to be smaller than the sample area before collecting data. Because of that the FT-IR microscope measurement is very sensitive to the sample thickness, which would change the beam focus and light path, the SiC clean surface, i.e. SiC film without Ga^+ doping, was set as the background sample for the purpose of keeping the same light path for the background and other samples.

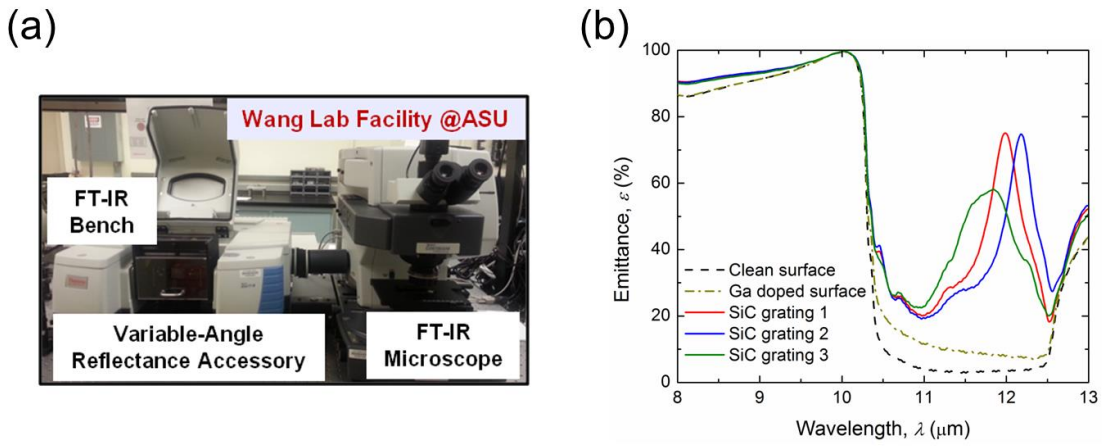

Figure 3.18 (a) Picture of FT-IR spectrometer with both the bench and microscope parts. (b) The emittance as a function of the wavelength for different samples, including three SiC grating patterns, SiC film with and without Ga^+ ion doping on the surface.

On the other hand, the absolute reflectance and transmittance of SiC clean surface in the size of 1 inch by 1 inch, were characterized by the FT-IR bench, denoted as $R_{film,bench}$ ($T_{film,bench}$). The absolute reflectance or transmittance of patterned samples, i.e. $R_{gratings,abs}$ ($T_{gratings,abs}$), could be obtained as the product of those of SiC clean surface absolute reflectance or transmittance measured in FT-IR bench and the relative reflectance or transmittance of the sample measured in FT-IR microscope using SiC clean surface as the background, which is $R_{grating,micro}/R_{film,micro}$ ($R_{grating,micro}/R_{film,micro}$). Therefore, it can be derived as $R_{gratings,abs} = R_{film,bench} \times R_{grating,micro}/R_{film,micro}$ ($T_{gratings,abs} = T_{film,bench} \times T_{grating,micro}/T_{film,micro}$). 16 scans were averaged to get one measurement and the data point resolution is 1 cm^{-1} in wavenumber. Note that the numerical aperture of the microscope objective is 0.58, which corresponds to the incidence angle up to 35º, so the measured optical properties are based on the averaged ones for the incidence angle from 0 to 35º. However, from the theoretical calculations as shown later, the difference between different incidence angles from 0 up to 45 º is quite small, so the measured optical properties are considered as the normal ones for the following discussions.

The spectral emittance (ε), which is calculated by $\varepsilon = 1-R-T$ (R and T are respectively spectral reflectance and transmittance measured in the FT-IR spectrometer) due to Kirchhoff's law and energy balance, is presented in Fig. 3.18(b) for different samples. Actually, all the samples are opaque during the wavelength range shown in Fig. 3.18(b) with the transmittance equal to zero. For the case of SiC clean surface, which refers to the intrinsic 340-μm-thick SiC film, it is highly emissive from 8 μm to 10 μm, and then the emittance becomes very low from 10.5 μm to 12.5 μm and increases a little bit after 12.5 μm. This is the typical behavior of the optical properties when SiC supports

phonon modes from 10.5 μm to 12.5 μm, during which it is highly reflective with low emittance.

Compared to SiC clean surface, the SiC gratings, which represent the samples with 2D gratings etched on the surface of the intrinsic SiC film, can follow almost the same trend except the additional emittance peaks occurring in SiC phonon bands. These additional peaks are caused by the excitation of MP, which will be verified later from theoretical calculations. Comparing the MP resonance of SiC grating 1 and 2, they have almost the same peak value as large as 0.8, while the resonance wavelength is shifted a little bit. This is mainly caused by the difference of the slit width and grating depth between grating 1 and 2, which play an important role in determining the MP resonance wavelength. Different from grating 1 and 2 with a single grating depth, grating 3 has multiple depths as mentioned above. The emittance peak due to MP excitation for grating 3 is broadened compared with grating 1 and 2, which is because MP is excited at multiple wavelengths with multiple grating depths. The peak value is however smaller due to that each MP resonance emits less when occupying only 1/3 number of the gratings.

Besides the existence of additional MP resonance peaks for SiC gratings discussed above, the emittance for the whole spectral range from 10.5 to 12.5 μm is higher than that of SiC clean surface. This enhanced emission is caused by the Ga^+ ion left on the surface of SiC gratings when fabricating them through focused ion beam technique. In order to confirm this reason, we made another sample with Ga^+ ion beam just shining on one area of the intrinsic SiC film surface without any pattern. The optical properties were characterized and the spectral emittance is also presented in Fig. 3.18(b), which is denoted as “Ga doped surface”. Compared to SiC clean surface, Ga doped

surface emits more energy from 10.5 to 12.5 μm, and different doping levels possess different emission enhancements.

3.4.3 Optical properties measurement in both infrared and visible regions

In addition to the optical properties characterization in the infrared region using FT-IR spectrometer discussed above, we also built a platform to measure the visible transmittance and reflectance of SiC gratings. Figure 3.19(a) shows the schematic for the light path of this platform, which mainly consists of a tungsten broadband light source, a beam splitter, optical fibers, several collimators and focusing lens, an objective, a camera and a CCD spectrometer. The light emitted from the tungsten lamp is collimated at first, then incident on the beam splitter through optical fibers, and then the light is reflected and focused through an objective on the sample placed on a holder. The light going through the sample will be collected by a CCD spectrometer for the transmittance measurement, and part of the light will be reflected to the camera for the purpose of image. Note that for transmittance measurement, the background signal was taken when no sample was placed on the holder. Similar to the infrared measurement through FT-IR microscope, due to the focus effect of the objective, the measured optical properties were based on the averaged ones for different incident angles. The numerical aperture for the objective is 0.6, which means that the incident angle varies from 0 up to 37º.

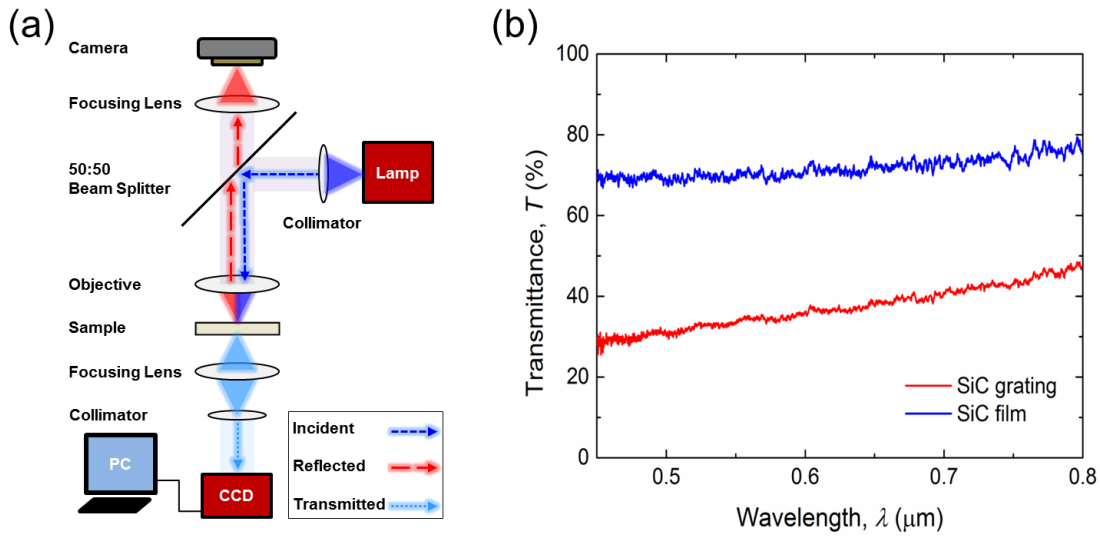

Figure 3.19 (a) Schematic for the light path of a home-made platform to measure visible transmittance of microstructures. (b) Measured visible transmittance for both intrinsic SiC film and SiC grating samples.

The visible transmittance measurements for both SiC grating, which refers to the grating 1, and intrinsic SiC film are presented in Fig. 3.19(b). For the intrinsic SiC film, the transmittance from 450 nm to 800 nm could be as high as 70%, while that for SiC grating 1 varies from 30% to 50%. The correctness of the measurements using this platform was verified through comparing the visible transmittance of the SiC film measured in this platform with that from FT-IR bench, and the difference is within 5% at most wavelengths. The low transmittance for SiC grating is mainly due to the Ga^+ ion absorption, which also affects the infrared optical properties measurement as discussed in Fig. 3.18(b). From the theoretical calculations, which will be introduced in the following, the visible transmittance difference between SiC film and SiC grating without considering Ga^+ doping effect is negligible. We also want to mention that when we were doing the transmittance measurement for SiC grating, the spot size after focus is 100 μm in diameter, which is larger than the grating pattern size of 45 μm×45 μm. This means

that the measured transmittance of SiC grating shown in Fig. 3.19(b) include both the patterned areas and the surroundings without patterns, which is not exactly the transmittance of single SiC grating. The main reason to still present Fig. 3.19(b) here is to show the high visible transmittance of SiC film and illustrate the Ga^+ doping effect in visible range, and the next step will be trying to reduce the spot size to be smaller than the pattern.

3.4.4 Comparison between experimental measurement and theoretical calculation

After introducing the experimental measurements for different SiC samples, we also conducted the theoretical calculations through RCWA and compared them with the measured data. Besides the spectral emittance coming from the experimental measurement, the results of theoretical calculations from three different fitting models are also presented in Fig. 3.20. For RCWA calculations, a total of 81 diffraction orders were used after the convergence check, and it was assumed as normal incidence. An objective function is firstly introduced as follows [14]

$$f = \sum_{i=1}^{N} \left(\varepsilon_{i,\text{theo}} - \varepsilon_{i,\text{exp}} \right)^2 \tag{3.12}$$

where $\varepsilon_{i,\text{theo}}$ and $\varepsilon_{i,\text{exp}}$ represent the spectral emittance from theoretical calculations and experimental measurements, respectively. N is the number of data points in the spectral range. Note that the objective function f also depends on N and $N = 609$ is applied here. For different fitting models, the optimization principle is basically minimizing the objective function to get the minimum difference between theoretical calculations and experimental measurements.

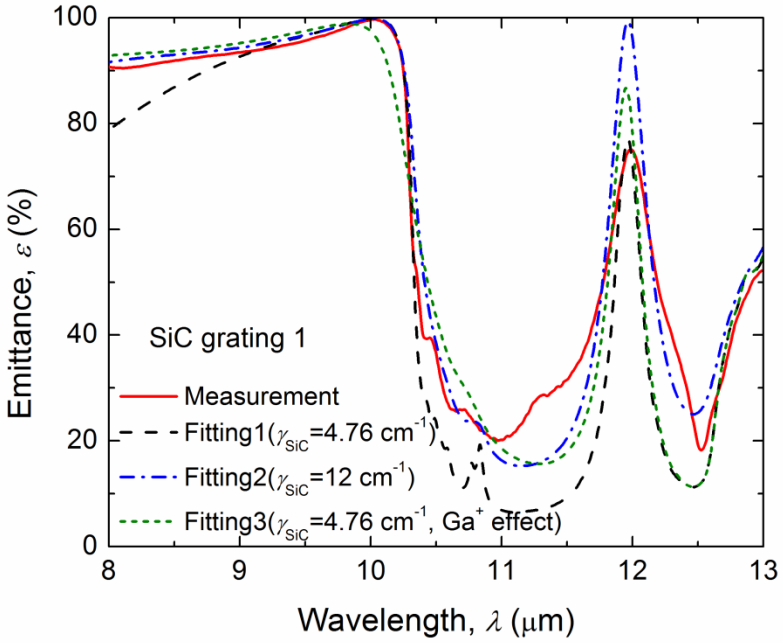

Figure 3.20 Comparison of spectral emittance between experimental measurement and theoretical calculations with different fitting models.

For the fitting model 1, the intrinsic SiC dielectric function with a Lorentz model is assigned.

$$\varepsilon_{\mathrm{SiC}} = \varepsilon_{\infty}\left(1+\frac{\nu_{LO}^2-\nu_{TO}^2}{\nu_{TO}^2-i\gamma_{\mathrm{SiC}}\nu-\nu^2}\right) \tag{3.13}$$

where the constants are set as $\varepsilon_{\infty}=6.7$, $\omega_{LO}=969\,\mathrm{cm}^{-1}$, and $\omega_{TO}=793\,\mathrm{cm}^{-1}$, and ν is the wavenumber. The intrinsic SiC scattering rate of $\gamma_{\mathrm{SiC}}=4.76\,\mathrm{cm}^{-1}$ is set for fitting model 1. Comparing the measured data and the theoretical one based on fitting model 1 in Fig. 3.20, it can be clearly observed that the theoretical one can capture the experimental data very well, especially the MP resonance in both wavelength and peak value. However, the enhanced emittance for the whole spectral range from 10.5 to 12.5 μm due to Ga^+ ion doping can't be captured in this model. The objective function for

fitting model 1 is 1.12×10^5. To include the Ga^+ ion doping effect in the theoretical model, we considered the scattering between Ga^+ ions and SiC phonons, which would change the scattering rate of intrinsic SiC [14]. Therefore, for the fitting model 2, instead of using intrinsic SiC scattering rate, we tried to fit it to minimize the objective function. It was found that *f* is minimized with a value of 3.40×10^4 when γ_{SiC} = 12 cm^{-1}. Compared with the fitting model 1, the model 2 has a better prediction for the enhanced emittance coming from Ga^+ ion doping, but the emittance peak value from MP excitation is much higher than the measured one.

On the other hand, another way to consider the Ga+ ion doping effect is adding a Drude model to the material dielectric function as illustrated in fitting model 3.

$$\varepsilon = \varepsilon_{SiC} + \varepsilon_{Ga^+} \tag{3.14}$$

where the Lorentz model for SiC dielectric function ε_{SiC} is still used with the intrinsic scattering rate of $\gamma_{SiC} = 4.76\,cm^{-1}$. The Drude model $\varepsilon_{Ga^+} = -\nu_{p,Ga^+}^2 / (\nu^2 + i\gamma_{Ga^+}\nu)$ is assigned to consider the additional emission from Ga^+ ion doping. Both the plasma frequency ν_{p,Ga^+} and scattering rate γ_{Ga^+} need to be fitted to obtain the minimum objective function. When $\nu_{p,Ga^+} = 950\,cm^{-1}$ and $\gamma_{Ga^+} = 1050\,cm^{-1}$ are set, the minimum objective function of $f = 6.02\times10^4$ is obtained.

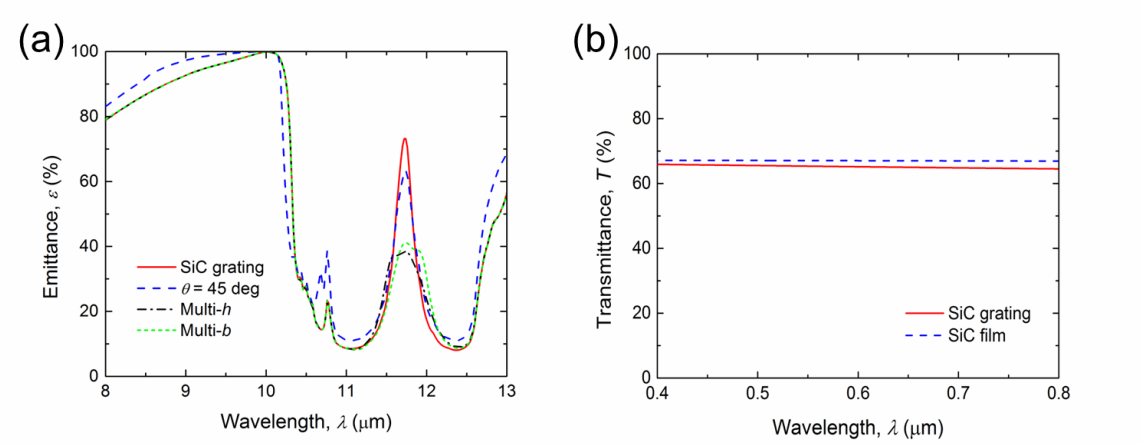

Figure 3.21 (a) Theoretical calculation of spectral emittance for SiC grating with different incident angles or geometries in the infrared region. The SiC grating base geometry is set as Λ = 5 μm, b = 0.5 μm and h = 1 μm. (b) Theoretical calculation of spectral transmittance for both SiC grating and film in the visible region.

The FDTD simulations were conducted to calculate the spectral emittance for SiC grating with different incident angles or geometries in the infrared region as shown in Fig. 3.21(a). The SiC grating base geometry is set as Λ = 5 μm, b = 0.5 μm and h = 1 μm, and it is assumed as normal incidence by default. Comparing the spectral emittances of the SiC grating with the base geometry at different incident angles of 0 and 45º, they are almost the same, even at the MP resonance wavelength. The independence of MP resonance on the incident angle has already been verified previously [81, 85]. As mentioned above, due to the focus cone of the objective, the measured optical properties using FT-IR microscope or home-made platform are actually averaged on the incident angles varying from 0 to 35 or 37º. The negligible difference between the optical properties of the SiC grating at different incident angles also explains the reasonability for the comparison between the measured data and theoretical calculations under normal incidence as shown in Fig. 3.20.

Figure 3.21(a) also presents the spectral emittance for the SiC grating with multiple grating depths of h = 0.8, 1, 1.2 μm or grating widths of b = 0.3, 0.5, 0.7 μm. Consistent with the measured spectral emittance of grating 3 shown in Fig. 3.18(b), the emittance peak due to MP resonance is broadened with a smaller value when the grating possesses multiple grating depths or slit widths. Figure 3.21(b) presents the visible transmittance for both SiC grating and film through RCWA simulations. Both the SiC grating and film are quite transparent in the visible range with the transmittance as high as 70%. Comparing these calculated visible transmittances with the measured ones in Fig. 3.19(b), we can see that for SiC film, the visible transmittances from experimental measurement and theoretical calculation are consistent, while those for the SiC grating are not. This big difference is caused by the additional absorption from the Ga^+ ion, which is not considered in theoretical calculations. One possible way to get rid of the Ga^+ ion doping effect is using a different method to fabricate the SiC grating, like photo or electron-beam lithography.

3.4.4 Raman spectrum of graphene covered SiC film

One potential application for the fabricated 2D SiC gratings is to demonstrate the tunable infrared emittance shown in Fig. 3.10 in experiment by covering graphene on top of it. Figure 3.24 shows the preliminary experimental results we have obtained. By collaborating with Prof. Sefaattin Tongay's group at ASU, graphene sheet was successfully fabricated on the copper substrate by the chemical vapor deposition method. A PMMA film was used to transfer the graphene from the copper substrate to the SiC film.

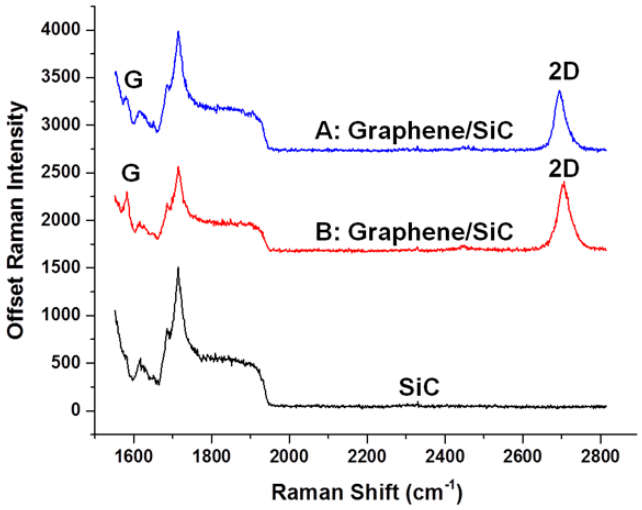

Figure 3.22 The offset Raman intensity for bare SiC film and graphene covered SiC film.

Raman spectroscopy was then applied to detect the existence of graphene and the number of carbon atom layers. As shown in Fig. 3.22, for bare SiC film, there are only several Raman intensity peaks for the Raman shift from 1600 to 2000 cm^{-1}. However, for the SiC film with graphene attached, besides the intrinsic Raman intensity peaks from SiC film, additional ones occur, which can be easily identified as the typical G and 2D peaks from the graphene. Considering the similar magnitude between the G and 2D peaks shown in Fig. 3.22, there is only one layer of graphene and it is attached very well on the SiC film. The next steps will be transferring the graphene to the top of SiC grating sample, depositing electrodes on both sides of the sample, then applying external bias to tune graphene chemical potential and finally charactering the optical properties in the infrared region through FT-IR microscope.

3.4.5 Application of visibly transparent radiative cooling device

As discussed above, the 2D SiC grating possesses high transmittance together with low absorptance in the visible region if not considering the Ga^{+} ion doping effect from the fabrication process, and relatively high emittance in the infrared region. This particular optical properties selectivity holds great potential for the application of visibly transparent radiative cooling devices. Figure 3.23(a) presents the idea to achieve a cooling device with temperature below the ambient through radiative heat transfer while keeping visibly transparent.

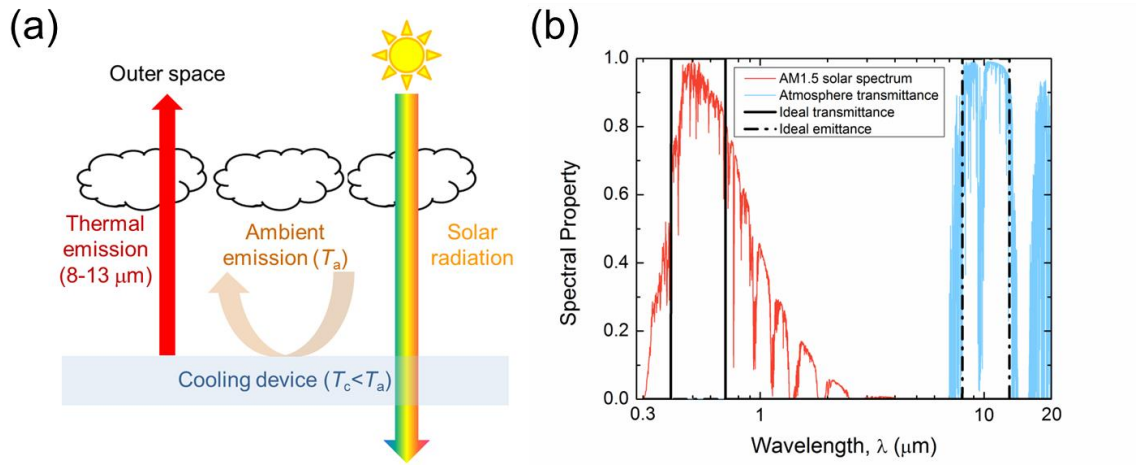

Figure 3.23 (a) Schematic to show the idea of a visibly transparent radiative cooling device. (b) The required spectral properties for an ideal cooling device along with the solar spectrum and the transmittance of atmosphere.

It contains three main requirements for the spectral properties of the cooling device at different spectrum ranges. In the solar radiation, especially the range of visible light, we want the light to be transmitted for the purpose of illumination. In order to enhance the thermal emission directly to the outer space, the emissivity of the cooling device during the atmospheric window from 8 μm to 13 μm needs to be as high as possible. However,

the emissivity in the infrared region while outside the atmospheric window range has to be minimized to reduce the absorbed energy from the ambient emission. To better illustrate the above idea, the spectral properties required for an ideal cooling device are plotted in Fig. 3.23(b) along with the normalized solar spectrum and the transmittance of atmosphere. Note that the data for Global Tilt AM1.5 solar spectrum is available on NREL's website, and the transmittance of atmosphere is obtained from Gemini Observatory in Mauna Kea. As shown in Fig. 3.23(b), for an ideal visibly transparent cooling device, it should have unity transmittance in the visible region while none transmittance outside. The ideal cooling device also needs to possess unity emittance during the atmospheric window from 8 μm to 13 μm and be non-absorbing out of the window. Note that the reflectance can be derived from the emittance and transmittance due to the energy balance.

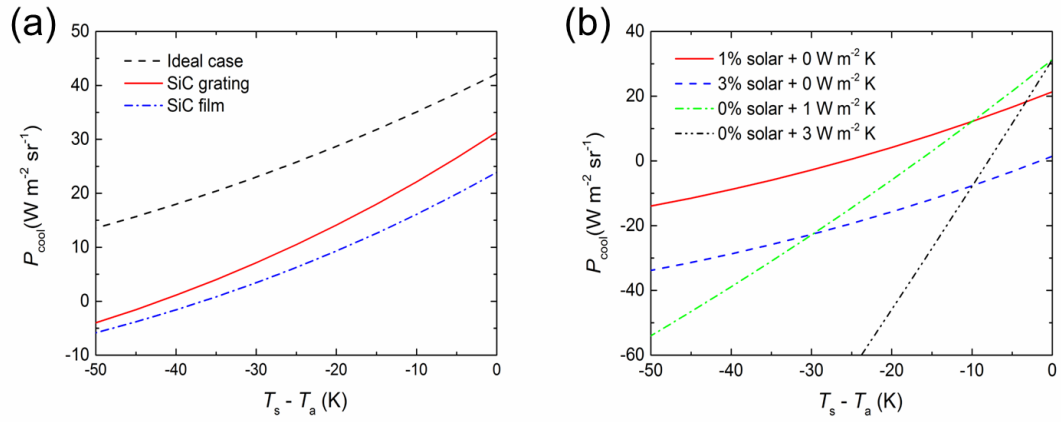

Figure 3.24 Net radiative cooling power vs the temperature difference between the cooling device and the ambient for (a) different samples without considering solar absorption and convective heat transfer and (b) SiC grating sample considering solar absorption and convective heat transfer with different levels. Note that the SiC grating refers to the pattern 1.

We now consider the potential cooling efficiency that can be offered by the SiC grating. Note that only the measured optical properties of SiC grating 1 are applied here to be taken as an example. The net radiative cooling power at normal direction emitted from the device can be defined as [3]

$$P_{\text{cool}}(T_{\text{c}}) = P_{\text{rad}}(T_{\text{c}}) - P_{\text{sun}} - P_{\text{atm}}(T_{\text{a}}) \tag{3.15}$$

where

$$P_{\text{rad}}(T) = \int_{5\mu\text{m}}^{15\mu\text{m}} d\lambda I_{\text{BB}}(T,\lambda)\varepsilon(\lambda) \tag{3.16}$$

is the heat flux radiated by the cooling device at normal direction

$$P_{\text{atm}}(T_{\text{a}}) = \int_{5\mu\text{m}}^{15\mu\text{m}} d\lambda I_{\text{BB}}(T_{\text{a}},\lambda)\varepsilon(\lambda)\varepsilon_{\text{atm}}(\lambda) \tag{3.17}$$

is the absorbed heat flux by the cooling device emitted from atmospheric radiation at normal incidence, and

$$P_{\text{sun}} = \int_{0.2\mu\text{m}}^{2\mu\text{m}} d\lambda\varepsilon(\lambda) I_{\text{AM1.5}}(\lambda) \tag{3.18}$$

is the incident solar heat flux absorbed by the cooling device at normal direction. Here only the direction of normal incidence is considered. $I_{\text{BB}}(T,\lambda) = (2hc^2/\lambda^5)[1/(e^{hc/(\lambda k_{\text{B}}T)} - 1)]$ is the spectral radiance of a blackbody at temperature T according to Planck's law. $\varepsilon(\lambda)$ is the spectral emissivity of the sample. The emissivity of the atmosphere at normal incidence is calculated by $\varepsilon_{\text{atm}}(\lambda) = 1 - t(\lambda)$, where $t(\lambda)$ is the atmospheric transmittance in the zenith direction presented in Fig. 3.23(b). The ambient and cooling device temperature are assumed as T_{c}, and T_{a}, respectively. The AM1.5 Global Tilt spectrum $I_{\text{AM1.5}}(\lambda)$ shown in Fig. 3.23(b) represents the solar radiation incident on the cooling device. Note that all the spectrums are

integrated from 5 μm to 15 μm to consider thermal emission and from 0.2 μm to 2 μm to consider solar radiation, which are enough to cover almost of the thermal emission and solar radiation, respectively.

Figure 3.24(a) shows the net radiative cooling power at normal direction as a function of the temperature difference between the cooling device and ambient for three different samples of the ideal one with the optical properties shown in Fig. 3.23(b), and the SiC grating and film with measured infrared emittance shown in Fig. 3.18(b). Although the optical properties of SiC grating and film were measured through the whole spectral range from 5 μm to 15 μm, only part of it from 8 μm to 13 μm is presented in Fig. 3.18(b) to emphasize the MP resonance effect. Note that the solar absorption and convective heat transfer are not considered in Fig. 3.24(a). The ideal sample can emit the most radiative cooling power, and the SiC grating has better cooling performance than the SiC film. When the net radiative cooling power equals to zero, which corresponds to the equilibrium temperature that could be achieved through radiative heat transfer between the cooling device and the ambient, the temperature of SiC grating is 40 K below the ambient, while that for SiC film is 35 K.

Considering the solar absorption and convective heat transfer, the net radiative cooling power emitted from the SiC grating sample is illustrated in Fig. 3.24(b). When 1% solar absorption is considered, i.e. $\varepsilon(\lambda)$ = 1% from 0.2 μm to 2 μm, the temperature difference between the SiC grating sample and the ambient decreases from 40 K for none solar absorption case to 20 K. However, when the solar absorption increases to 3%, the sample temperature is almost the same with the ambient when the radiative cooling

power is equal to zero. Similarly, when the convective heat transfer is applied, the radiative cooling performance will be degraded significantly.

CHAPTER 4 NEAR-FIELD TUNABLE RADIATIVE HEAT TRANSFER

As mentioned in the introduction, the significant near-field radiative heat transfer enhancement due to evanescent waves coupling makes it possible to have thermal management through photon transport, which has a much faster speed compared to phonon transport. For the purpose of implementing tunable near-field radiative heat transfer in practice, a VO_2-based thermal rectifier and thermal switch, which are achievable around room temperature, and a graphene-based thermal transistor, which consists of only two plates and shows less challenge in experiment compared to three-body one, are proposed in this study. The radiation-based near-field thermal rectifier is made of a VO_2 plate and a SiO_2 plate, and due to the SPhP coupling, the energy transfer will be greatly enhanced when VO_2 is the receiver and SiO_2 is the emitter compared to the reverse case, which provides the thermal rectification effect. Similarly, a radiation-based near-field thermal switch considering VO_2 as both emitter and receiver will also be introduced. Next, because of the more flexible tunability of graphene, an electrically-gated near-field thermal transistor with two graphene covered plates will be theoretically studied. Finally, an initial design of the platform used to measure near-field radiative heat transfer between two plates will be discussed as well.

4.1 VO_2 Based Near-Field Radiative Thermal Rectification

In the present study, we investigate the near-field thermal rectification effect enabled by the phase transition of VO_2. Consider a vacuum thermal rectifier made of a semi-infinite SiO_2 and a semi-infinite VO_2 plates separated by a vacuum gap d, depicted as the Fig. 4.1(a). In the forward-biased scenario, SiO_2 is the emitter at T_h = 400 K, while

the receiver VO_2 is maintained at T_c = 300 K as an insulator. The radiative heat flux between the SiO_2 and VO_2 insulator is denoted as q_f, while it becomes as q_r when the temperatures are reversed, in which case VO_2 is the emitter at T_h = 400 K as a metallic material. The thermal rectification factor can be defined as the relative enhancement of the radiative heat transfer in the forward-biased scenario to that in the reverse-biased scenario,

$$R = q_f / q_r - 1 \tag{4.1}$$

Fluctuational electrodynamics [63], based on the stochastic nature of thermal emission, is used to calculate the near-field radiative heat fluxes for both scenarios. Figure 4.1(b) shows the net radiative heat fluxes calculated for both forward- and reverse-biased scenarios as a function of vacuum gap d, which varies from 10 nm to 1 μm. In both cases the heat flux monotonically increases due to stronger coupling of evanescent waves as the separation distance between the SiO_2 and VO_2 decreases. More importantly, the forward heat flux q_f is much larger than the reversed one q_r, and could be more than 10^3 W/m^2 at a 1-μm vacuum gap, and approaches to 10^6 W/m^2 at d = 10 nm. The calculated rectification factor is as high as 0.98 at a vacuum gap of 1 μm, decreases to 0.9 at the gap of approximately 300 nm, and then increases quickly when the vacuum gap further decreases. The rectification factor of 1.31 can be obtained at a 100-nm vacuum gap, 1.67 at d = 50 nm, and 1.95 at d = 10 nm. The rates of change of heat flux with respect to the vacuum gap in the forward- and reverse-biased cases are different. Consequently thermal rectification does not vary linearly with vacuum gap. Unlike previous studies [47-50], such strong rectification is achieved when the temperatures of emitter and receiver are close to room temperature.

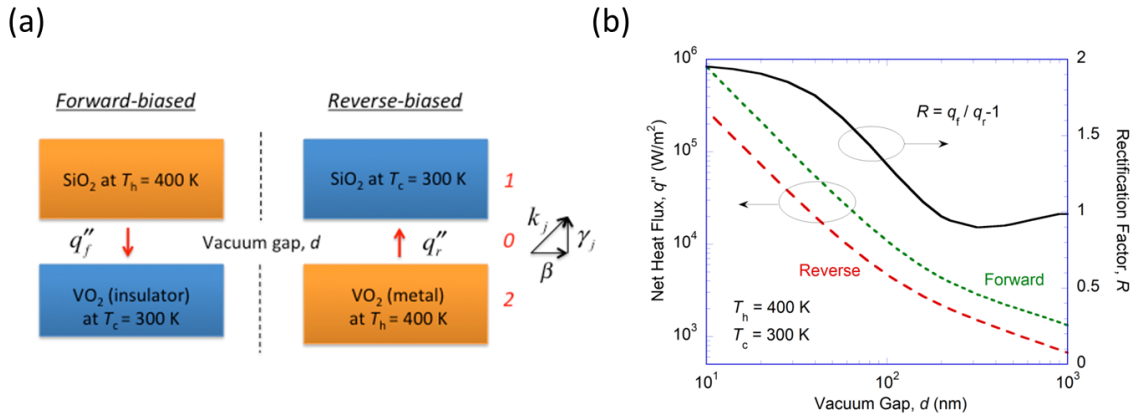

Figure 4.1 The total heat fluxes in both scenarios and the resulting rectification factor with different vacuum gap distances. The temperatures of the emitter and receiver are 400 K and 300 K, respectively. The inset depicts the proposed vacuum thermal rectifier made of semi-infinite SiO_2 and VO_2 separated by a vacuum gap d in forward- or reverse-biased scenario.

The strong rectification effect is believed to be due to the insulator-metal phase transition of VO_2 between the forward- and reverse-biased scenarios. During the forward bias, VO_2 behaves as an insulator with several optical phonon modes in the infrared, while in the reverse bias it behaves as a metal. To further understand the effect of the phase transition on the radiative heat fluxes in both scenarios, the exchange function $s(\omega, \beta)$ between SiO_2 and VO_2 insulator and between SiO_2 and VO_2 metal are plotted at d = 100 nm as a function of ω and β in Figs. 4.2(a) and 4.2(b), respectively . Note that β is normalized to the free-space wavevector ω/c_0. For the insulating VO_2, it can be clearly seen that, there exist several enhancements indicated by the bright color and high values of the contour, suggesting strong coupling of the evanescent waves across the vacuum gap between SiO_2 and VO_2 insulator. Moreover, the strongest enhancement peak occurs

around ω = 8.5×10^{13} rad/s, and the associated β values can reach as high as 80ω/c, implying that the near-field enhancement can be supported over a large number of modes.

Another two enhancements with relative weaker strengths occur around ω = 1.1×10^{14} rad/s and 1.5×10^{14} rad/s. As discussed by Basu et al. [86], the enhancement of near-field heat transfer due to coupled SPPs or SPhPs is dominated by the *p*-polarized evanescent waves. Also, the reflection coefficient for *p* polarization strongly depends on both the ordinary and extraordinary dielectric functions of VO_2 insulator. As such, the spectral locations for near-field enhancement in Fig. 4.2(a) corresponds to the frequency values at which $\varepsilon_E = -1$. In addition, both VO_2 insulator and SiO_2 have phonon modes within this frequency range. The strong enhancement in the *s* function and thus the radiative heat flux q_r is also the result of the strong phonon-phonon coupling between the SiO_2 and VO_2 insulator inside the vacuum gap. On the other hand, in the reverse case, the *s* function only shows two weaker enhancements around ω = 8.5×10^{13} rad/s and 2×10^{14} rad/s, corresponding to the two major phonon modes of SiO_2, as seen in Fig. 4.2(b). The weaker coupling as shown by the *s* function is because the metallic VO_2 does not have the phonon modes to resonate with those of SiO_2 in the same frequency region.

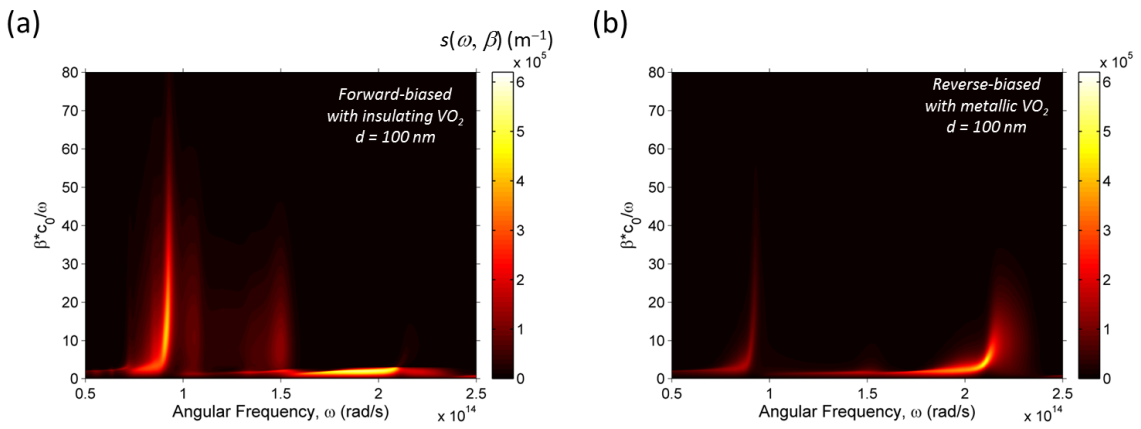

Figure 4.2 Contour plots of the exchange function $s(\omega, \beta)$ between semi-infinite SiO_2 and VO_2 separated by the vacuum gap of d = 100 nm for (a) forward-biased scenario with insulating VO_2 and (b) reverse-biased scenario with metallic VO_2.

So far, we have demonstrated that strong thermal rectification effect can be obtained from the near-field radiation between semi-infinite SiO_2 and VO_2 separated by a vacuum gap from 10 nm to 1000 nm. An interesting question is: could the rectification effect be further enhanced? Here, we consider SiO_2 as a thin film and investigate how the film thickness affects the radiative heat flux in both scenarios and thus the rectification factor. The inset in Fig. 4.3(a) shows the schematic of the near-field heat transfer between a freestanding SiO_2 thin film with thickness t and bulk VO_2 for both forward- and reverse-biased scenarios. Francoeur et al. [66, 87] have derived an analytical expression for calculating the near-field thermal radiation between two freestanding SiC thin films. Basu and Francoeur [49] used a similar analytical expression to investigate the near-field radiation between a film and a semi-infinite plate of doped silicon. This analytical expression considers the wave propagation inside the thin film, and is valid as long as the substrate that the thin film is deposited on is non-emitting. Therefore, the near-field

radiative transfer between the SiO_2 film and the semi-infinite VO_2 can be obtained by simply replacing the Fresnel reflection coefficient at the interface of vacuum and SiO_2 in with the reflection coefficient of the SiO_2 thin film based on the thin-film optics by[49, 58]

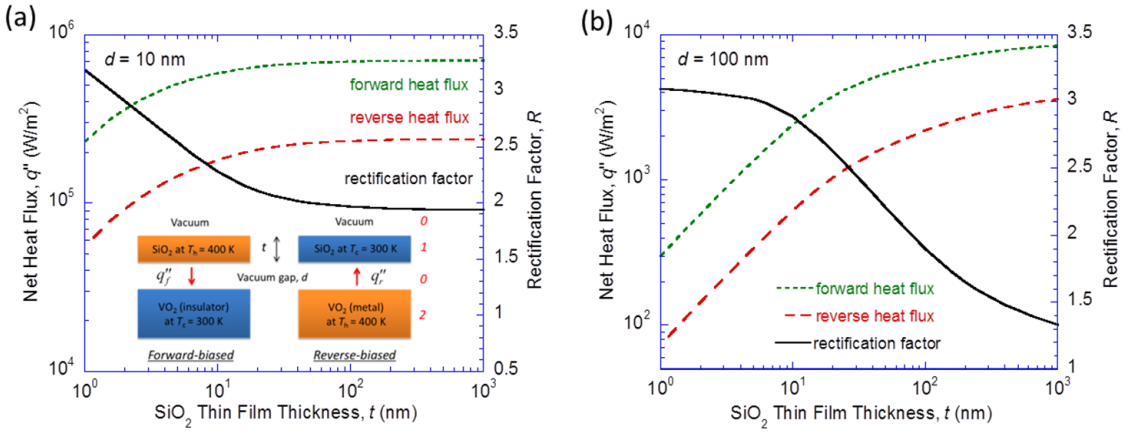

Figure 4.3 The SiO_2 film thickness effect on the radiative heat fluxes for both scenarios and rectification factor at the vacuum gap of (a) 10 nm and (b) 100 nm, from a vacuum rectifier consisting of a SiO_2 thin film with thickness t and semi-infinite VO_2 shown as the inset.

Figure 4.3(a) shows the near-field radiative heat fluxes between the SiO_2 thin film and the VO_2 at the vacuum gap of d = 10 nm in both scenarios as a function of the film thickness t. Both forward and reverse heat fluxes increase monotonically when the film thickness increases from 1 nm to 30 nm or so, and then saturate with further increase in the film thickness. This is because at a vacuum gap of 10 nm, a 30-nm-thick SiO_2 film can act as a semi-infinite medium for near-field thermal radiation [88]. As a result, R is independent of the film thickness t and saturates around 2 when t > 30 nm. When the

SiO_2 film thickness further decreases, both forward and reverses heat fluxes decreases but the rectification factor *R* increases almost linearly.

When the film thickness is less than the penetration depth, SPhPs on both interfaces of the SiO_2 film can be excited and couple with each other inside the thin film. However, at d = 10 nm, the coupling of evanescent waves inside the vacuum gap dominates the near-field heat transfer [89], and the resulting radiative heat transfer depends strongly on the strength of the coupling. At forward- or reserve-biased scenarios, the strength of the coupling of evanescent waves is significantly different as explained above between the semi-infinite SiO_2 and VO_2. Therefore, the radiative heat flux depends differently on the film thickness between the two scenarios, resulting in the linear relationship between rectification factor and film thickness when t < 30 nm at d = 10 nm. The decrease of the heat fluxes in both scenarios is mainly due to less emitting (or absorbing) material when the SiO_2 film becomes thinner.

However, the rectification effect on the film thickness behaves totally different when the vacuum gap is set to 100 nm, as shown in Fig. 4.3(b). Both forward and reverse heat fluxes decrease when the SiO_2 film thickness changes from 1 μm to 1 nm, but the rectification factor increases gradually with thinner films and saturates around 3 when t < 10 nm. For ultra-thin film with sub-10-nm thickness, $t << d$ and the SPhPs at both interfaces of the SiO_2 film inside the thin film dominates the near-field radiative heat transfer, rather than the coupling of evanescent waves inside the vacuum gap [89]. The splitting of the near-field heat flux into symmetric and antisymmetric resonant modes could increase the number of modes in the near field, but on the other hand, the heat fluxes in both scenarios decrease with smaller films mainly because of less emitting (or

absorbing) material of the SiO_2 film. However, since the coupling of SPhPs inside the SiO_2 film dominates the near-field radiative transfer when $t << d$, both heat fluxes have the same dependence on the film thickness, which affects the symmetric and antisymmetric resonant modes of coupled SPhPs inside the film. Therefore, the resulting rectification effect is independent of the film thickness when $t < 10$ nm. When the film thickness is beyond 10 nm, the coupling between symmetric and antisymmetric modes becomes weaker and the coupling of evanescent waves inside the vacuum gap becomes stronger as the thickness increases. For $t/d > 1$, the thin film effect decreases and the heat transfer approaches to that between two bulks. As a result, the thermal rectification decreases and then eventually becomes constant when the SiO_2 film thickness is greater than 1 micron. Comparison between Figs. 4.1(b) and 4.3(b) indicates that at a vacuum gap of 100 nm, replacing bulk SiO_2 even with a 100-nm thin film will result in higher thermal rectification.

4.2 VO_2 Based Near-Field Radiative Thermal Switching

4.2.1 Total radiative heat flux

In the present study, we will first quantitatively show the near-field thermal switching effect between two semi-infinite VO_2 plates, one of which is maintained at room temperature as an insulator while the other serves as an emitter to experience insulator-metal transition when its temperature varies.

Let us first consider the 3-layer configuration of the proposal near-field thermal switch made of semi-infinite VO_2 emitter and receiver, as shown in Fig. 4.4(a), which presents the net radiative heat flux between the VO_2 plates separated by a vacuum gap of

d = 50 nm as shown in Fig. 4.4(b), when the emitter temperature changes from T_H = 330 K to 350 K. The VO_2 emitter is insulating at the beginning when T_H < 341 K, while the VO_2 receiver, whose temperature is fixed at T_L = 300 K, is always an insulator. The radiative heat flux is q'' = 15 kW/m^2 at T_H = 330 K, increases almost linearly with the emitter temperature, and reaches q'' = 21 kW/m^2 at T_H = 341 K. However, when the emitter temperature exceeds 341 K, the emitter becomes metallic. As a result, the radiative heat flux decreases abruptly to q'' = 5.2 kW/m^2 at T_H = 342 K, and increases slightly to q'' = 6.3 kW/m^2 at T_H = 350 K. Therefore, it can be clearly seen that, when crossing the phase transition of VO_2 at 341 K, near-field radiative heat transfer significantly reduces from q'' = 21 kW/m^2 to 5 kW/m^2, resulting in a switching factor of Φ = 76.2% at d = 50 nm. When the emitter temperature is below the phase transition point, it can be treated as the "on" mode for this vacuum thermal switch made of VO_2, while the "off" mode can be activated when the temperature is above the phase transition.

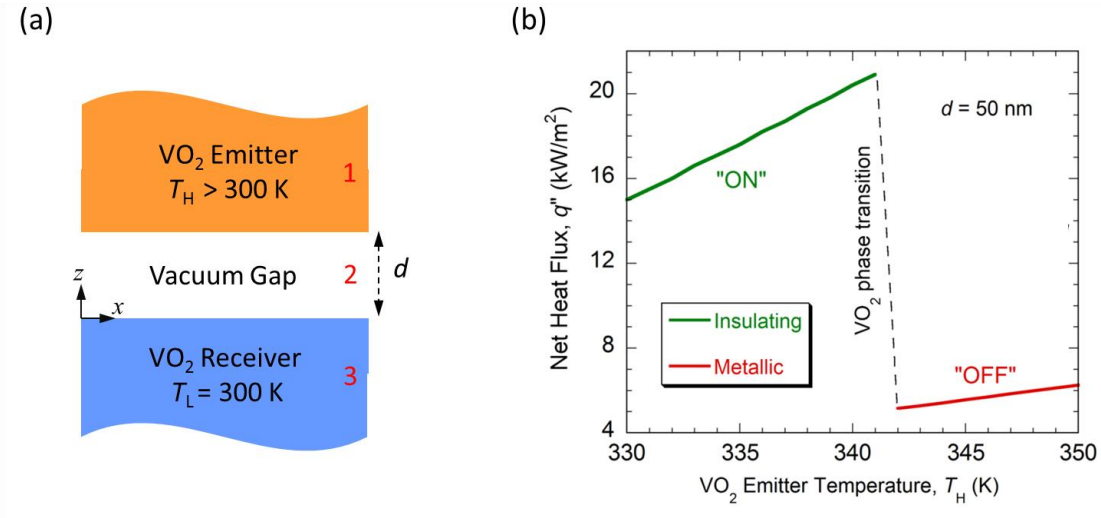

Figure 4.4 (a) Schematic of near-field thermal switch. (b) The total radiative heat fluxes between two semi-infinite VO_2 plates with different emitter temperatures T_H at the gap distance of d = 50 nm with the receiver temperature fixed at T_L = 300 K. The thermal switch is at the "on" mode when $T_H \leq 341$ K, while it turns to the "off" mode when $T_H \geq$ 342 K.

4.2.2 Contour plot of transmission coefficient

In order to have a better understanding of the physical mechanism of thermal switching effect realized by the near-field radiative transfer between two VO_2 plates, the energy transmission coefficient $\xi(\omega,\beta)$ is plotted for both TM and TE waves in either the "on" or "off" mode as shown in Fig. 4.5 at the same vacuum gap distance (d = 50 nm). The color bar shows the scale for $\xi(\omega,\beta)$ with the brightest color representing the peak value. As shown in Fig. 4.5(a) for the "on" mode in TM waves, strong enhancement suggested by the bright contour can be clearly seen, with a major one around ω_m = 1.5×10^{14} rad/s and several other peaks at smaller angular frequencies. The enhancement in the energy transmission coefficient, which results in the increase in radiative heat flux, is due to the strong phonon-phonon coupling, i.e., the excitation of SPhPs, between the insulating VO_2 plates across the small vacuum gap. Note that, for the "on" mode, both the emitter and the receiver are insulating VO_2 with several phonon modes in the infrared region. Those phonons could constructively resonate across the vacuum gap, resulting in increase of radiative heat transfer modes in the near field. The strongest enhancement occurs at ω_m=1.5×10^{14} rad/s in the energy transmission coefficient contour. Because

SPhPs cannot be excited in TE waves, the energy transmission coefficient in TE waves shown in Fig. 4.5(b) is much weaker than that in TM waves.

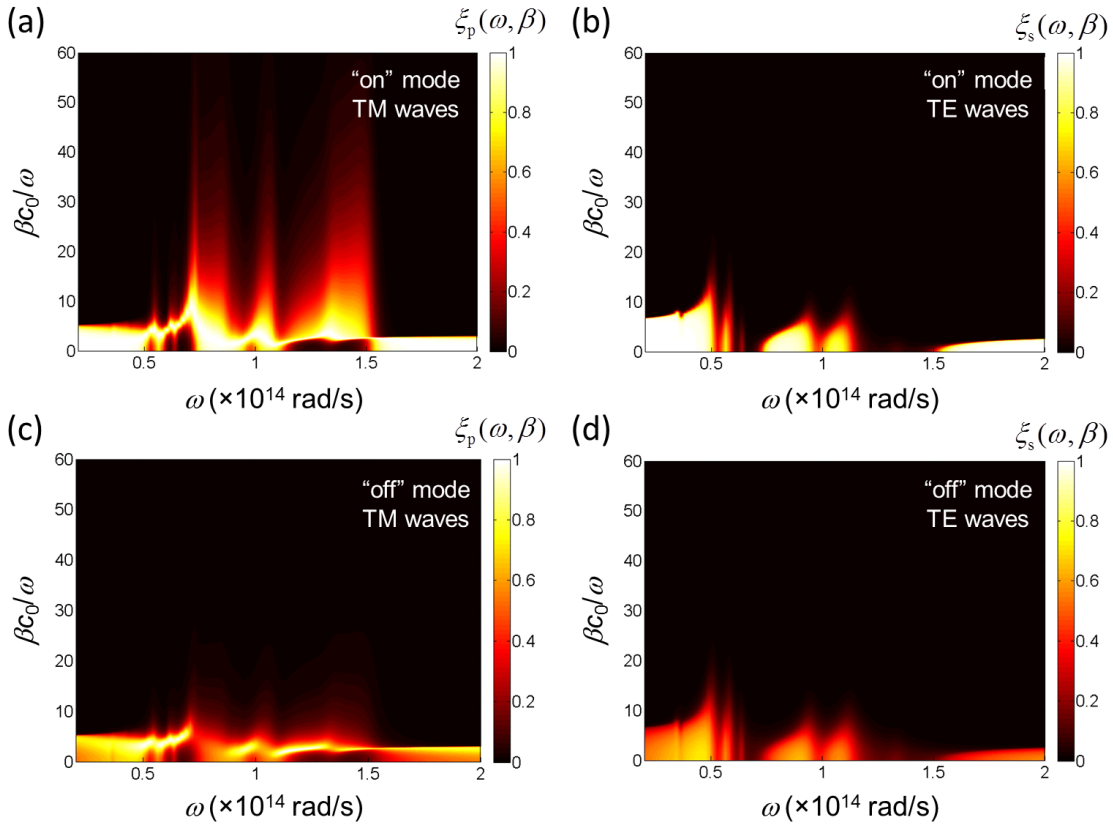

Figure 4.5 Contour plots of the energy transmission coefficient $\xi(\omega,\beta)$ between two semi-infinite VO_2 plates separated by a vacuum gap of d = 50 nm at the "on" mode between two insulating VO_2 for (a) TM waves and (b) TE waves and at the "off" mode between one metallic VO_2 and one insulating VO_2 for (c) TM waves and (d) TE waves.

On the other hand, when the emitter becomes metallic, which is the case for the "off" mode, the energy transmission coefficient between an insulating VO_2 and a metallic VO_2 is greatly suppressed as shown in Fig. 4.5(c) for TM waves. The phonon modes of

the insulating VO_2 could not constructively couple to the other metallic interface that does not support any phonon modes. Therefore, the radiative heat transfer is greatly reduced for the "off" mode, resulting in strong thermal switching effect upon phase change of VO_2. For the "off" mode, due to the fact that no SPhP is excited, the energy transmission coefficients in both TM and TE waves, respectively shown in Figs. 4.5(c) and 4.5(d), are comparable. Furthermore, due to the highly reflective nature of the metallic VO_2 emitter, the energy transmission coefficient in TE waves for the "off" mode shown in Fig. 4.5(d) is weaker than that for the "on" mode presented in Fig. 4.5(b).

4.2.3 Thermal switching factors at different vacuum gap distances

A switching factor can be defined as:

$$\Phi = 1 - q''_{\text{off}} / q''_{\text{on}} \tag{4.2}$$

where q''_{on} and q''_{off} refer to the net heat flux for the "on" and "off" modes of thermal switch, respectively. Fluctuational electrodynamics [90], based on the stochastic nature of thermal emission, was used to calculate the near-field radiative heat fluxes for both "on" and "off" modes of the proposed vacuum thermal switch.

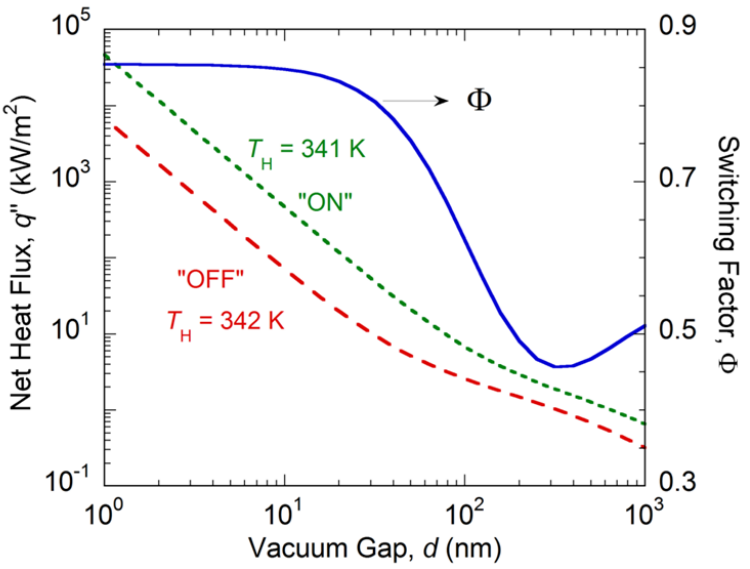

Figure 4.6 The total heat fluxes at both the "on" and "off" modes as well as the resulting switching factor at different vacuum gap distances. The receiver temperature T_L is 300 K. The emitter temperature T_H is set as 341 K and 342 K for the "on" and "off" modes, respectively.

To have a better idea of how the thermal switching effect varies with vacuum gap distances, Figure 4.6 plots the total net heat fluxes with different vacuum gap distances for both "on" and "off" modes, as well as the switching factor defined in Eq. (4.2). Here, the "on" and "off" modes respectively correspond to the emitter temperature T_H of 341 K and 342 K, while the receiver is fixed at T_L = 300 K. The switching factor can be as large as Φ_{max} = 0.85 when gap distance d < 10 nm, indicating that 85% of heat flux could be cut off when the thermal switch turns from the "on" mode to "off" mode. In addition, the high heat flux between two VO_2 plates with q'' > 500 kW/m^2 for the "on" mode at sub-10-nm vacuum gaps, suggesting potential applications for high-density heat dissipation in microelectronics. Since the dependence of the near-field radiative transfer on the vacuum

gaps is different between "on" and "off" modes, the switching factor starts to decrease when the gap distance d > 30 nm, reaches a minimum of Φ_{min} = 0.46 around d = 300 nm, and increases again to Φ = 0.51 at d = 1 μm.

4.2.4 Penetration depth inside uniaxial insulating VO_2

To obtain insight into how the near-field radiative energy is transferred, the z component of Poynting vector $S_z(\omega,z)$ is plotted in Fig. 4.7 at different depths inside the insulating VO_2 emitter and receiver separated by a vacuum gap of d = 50 nm. The penetration depth inside isotropic media has already been investigated, but when it comes to a uniaxial medium, we need to separate s and p polarizations and apply different expressions of vertical wavevector and reflection coefficient as described above. The Poynting vector $S_z(\omega,z)$ normalized to that in the vacuum is calculated at several angular frequencies such as $\omega = 0.7\times10^{14}$ rad/s, 1.05×10^{14} rad/s and 1.5×10^{14} rad/s, at which coupled SPhPs occur as shown in Fig. 4.5(a). From Fig. 4.7, we can clearly see that the penetration depth, i.e., a distance at which the radiation power is attenuated by a factor of 1/e (approximately 37%), varies with different resonance frequencies. The penetration depth for the spectral energy at $\omega = 0.7\times10^{14}$ rad/s is the largest, which is about 10 times of vacuum gap distance, while that for resonance frequency $\omega = 1.05\times10^{14}$ rad/s is the shortest, which is about the same with vacuum gap distance. The penetration depth for total radiative energy after the integration over ω is about 3 times of vacuum gap distance, similar to that for spectral energy of resonance frequency at $\omega = 1.5\times10^{14}$ rad/s, indicating that most of the energy transfer is concentrated at this resonance frequency.

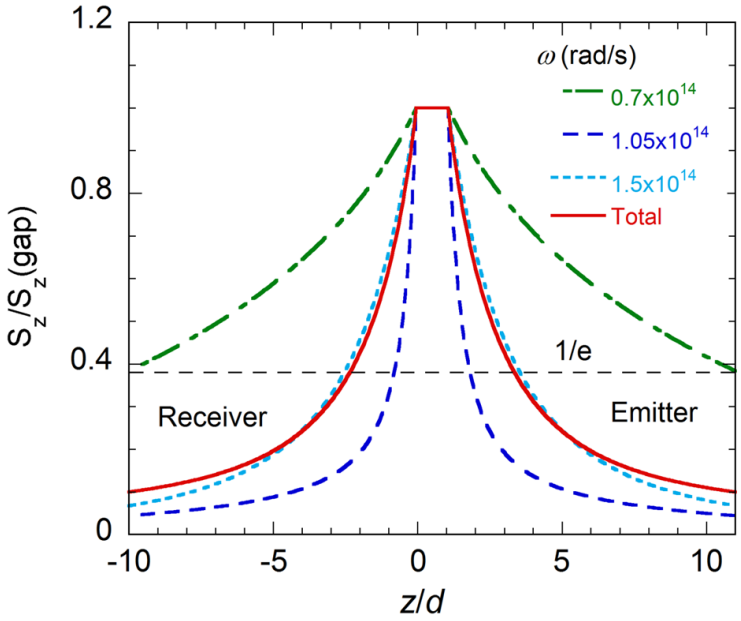

Figure 4.7 The field distribution of the spectral Poynting vector (z component) near the surfaces of the semi-infinite VO_2 emitter and receiver across a vacuum gap at several phonon frequencies of insulating VO_2 as well as the total one after integration over the frequency. The Poynting vector is normalized to that in the vacuum and the two semi-infinite insulating VO_2 plates is separated by d = 50 nm.

With a thickness of several times of the penetration depth, an insulating VO_2 film can be reasonably treated to be semi-infinite. On the other hand, if the film thickness is comparable or smaller than the penetration depth, the thin-film wave propagation has to be considered, which could influence the near-field radiative transfer and thereby possibly further enhance the thermal switching effect.

4.2.5 Thermal switching effect with a thin-film receiver

To investigate the thin-film effect on the near-field radiative thermal switching, a 4-layer configuration with a thin-film receiver of thickness t_3, as shown in the inset of Fig. 4.8, is considered. The near-field heat transfer along with the switching factor between a semi-infinite VO_2 emitter and a free-standing VO_2 thin-film receiver (i.e., vacuum substrate) is calculated as a function of the film thickness for both the "on" (i.e., T_H = 341 K) and "off" modes (i.e., T_H = 342 K). The gap distance is considered to be d = 300 nm, at which the switching factor has a minimum between two semi-infinite VO_2 plates as shown in Fig. 4.6, aiming to further enhance thermal switching effect with the thin-film effect.

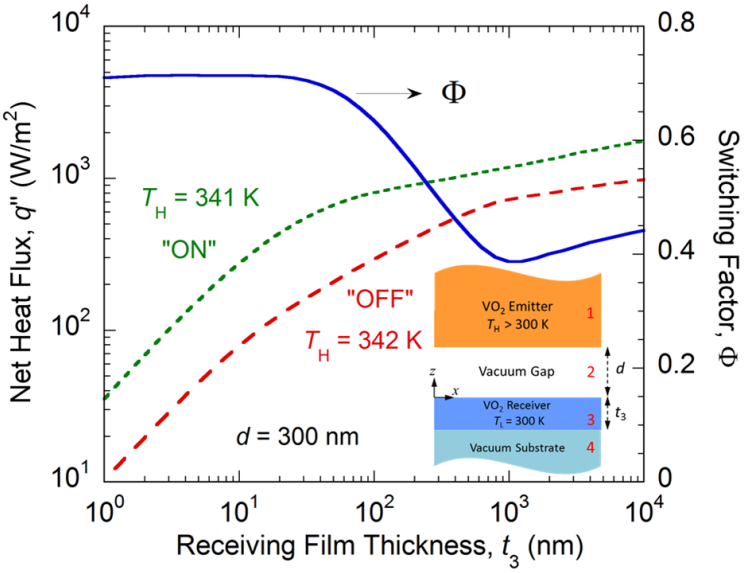

Figure 4.8 The thickness effect of the thin VO_2 receiver on the radiative heat fluxes for both "on" and "off" modes as well as the switching factor at the vacuum gap of d = 300 nm. Inset is the schematic of the 4-layer vacuum thermal switch consisting of a semi-infinite VO_2 emitter and a free-standing VO_2 thin receiver with thickness t_3.

As shown in Fig. 4.8, both the radiative heat fluxes for the "on" and "off" modes increase monotonically when the film thickness t_3 increases from 1 nm to 10 μm, which is simply due to the increase in the volume of receiving material. At the vacuum gap d = 300 nm, a uniaxial insulating VO_2 film with 10-μm thickness can still not be considered to be semi-infinite. For thin-film thickness smaller than the penetration depth, the SPhPs at both interfaces of thin-film VO_2 receiver can also couple with each other inside the thin film, in addition to the coupled SPhPs across the vacuum gap between two insulating VO_2 [19]. When t_3 increases from 1 nm to 20 nm, both the heat fluxes have the same dependence on the film thickness, which results in a nearly constant switching factor of Φ = 0.7. For sub-20-nm films, when the thickness is much smaller than the vacuum gap distance (i.e. $t_3 \ll d$), the SPhPs coupling inside the thin film will dominate near-field heat transfer [89], for which the splitting of the near-field heat flux into symmetric and anti-symmetric resonant modes could increase the number of modes in the near field. When t_3 > 20 nm, the coupling between symmetric and anti-symmetric modes becomes weaker and the coupling of evanescent waves inside the vacuum gap becomes stronger as the film thickness increases. Thus, the radiative heat flux at the "on" mode starts to increase with a smaller slope around t_3 = 50 nm, while this occurs for the "off" mode around t_3 = 1 μm or so. As a result, the switch factor Φ starts to experience a reduction with a VO_2 thin film at t_3 = 50 nm and reaches a minimum of 0.39 at t_3 = 1 μm. When the film thickness further increases, the thin-film effect is vanishing and the heat transfer approaches to that between two bulks. The switching factor increases to Φ = 0.44 for a 10-μm-thick VO_2 film. Clearly, the switching factor Φ becomes larger when the receiving VO_2 made of a thin film with thickness below 50 nm than a semi-infinite plate.

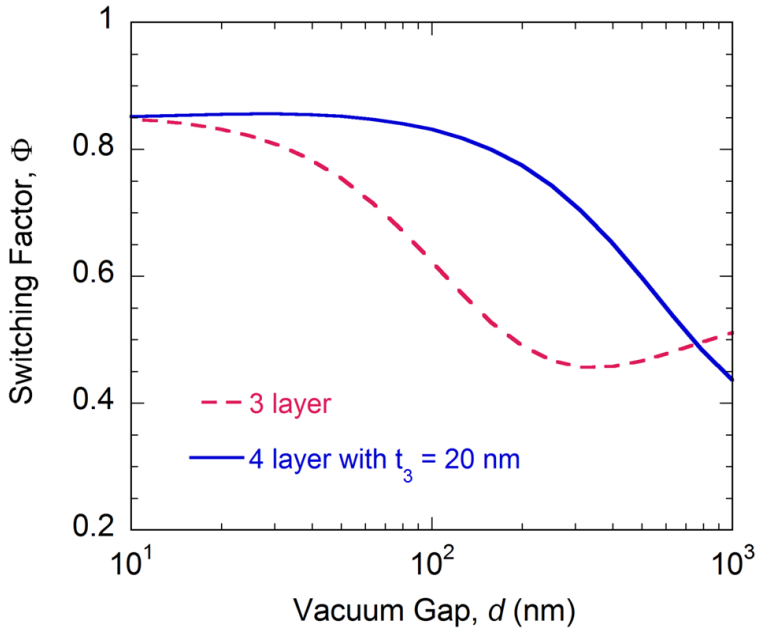

Figure 4.9 Comparison of the switching factor between the 3-layer vacuum switch and the 4-layer one with a 20-nm-thick free-standing thin-film receiver at different vacuum gaps. The emitter temperature T_H is set as 341 K and 342 K for the "on" and "off" modes, respectively.

The dependence of the film thickness clearly suggests further enhancement of the switching effect by using a thin-film receiver. Figure 4.9 compares the switching factors from a vacuum thermal switch in a 3-layer configuration with those from a 4-layer configuration with a thin-film receiver of 20 nm, at a wide range of vacuum gap distances. Clearly, when using a thin-film receiver, the thermal switching effect is greatly enhanced over a broad range of vacuum distances from d = 10 nm to nearly 1 μm. A maximal switching factor over 0.83 can be achieved at sub-100-nm gap. Moreover, the switching factor is improved from Φ = 0.62 to 0.83 at d = 100 nm, and from Φ = 0.49 to 0.78 at d = 200 nm with more than 50% relative increase. Note that, vacuum gaps of a few hundred

of nanometers could be practically achievable. The optimized vacuum thermal switch with a thin-film receiver would facilitate practical applications in thermal management and thermal circuits.

4.2.6 Effect of SiO_2 substrate on near-field thermal switching

From a practical perspective, the thin-film VO_2 receiver has to be deposited on a real substrate rather than thermal vacuum. Therefore, the effect of film substrate needs to be studied for a practical design of a vacuum thermal switch made of VO_2. Here, we consider SiO_2 as the substrate material for the VO_2 films as an example, while other substrate materials like Al_2O_3, silicon, and even metals can be analyzed in a similar approach. The optical properties of SiO_2 were taken from Palik's data [71]. Besides considering a 4-layer vacuum thermal switch with a thin receiving film on SiO_2 substrate, a 5-layer vacuum thermal switch design with both thin-film emitter and receiver on SiO_2 substrate will be also investigated. The theoretical model described in Section 2.2 will be employed for calculating the near-field radiative heat transfer between two uniaxial films on substrates.

With SiO_2 substrate, the receiving film thickness (t_3) effect on the radiative heat fluxes for both "on" and "off" modes as well as the switching factor at the vacuum gap of d = 300 nm is shown in Fig. 4.10(a). Similar to the case with vacuum substrate shown in Fig. 4.8, the heat fluxes for both "on" and "off" modes will increase with thicker films. However, due to the presence of SiO_2 substrate, the growth rate (i.e., the slope) of heat flux as a function of t_3 becomes smaller, while the amplitude of heat fluxes is higher, which can be understood by the modified reflection coefficients across the thin receiving

film due to the SiO_2 substrate. Moreover, SiO_2 is a polar material with strong phonon modes in the infrared region, which also helps the energy absorption in addition to the VO_2 thin film. As a result, the thermal switching factor at d = 300 nm increases slightly to Φ = 0.48 with the SiO_2 substrate compared to Φ = 0.45 with vacuum substrate at the same receiving film thickness t_3 = 50 nm.

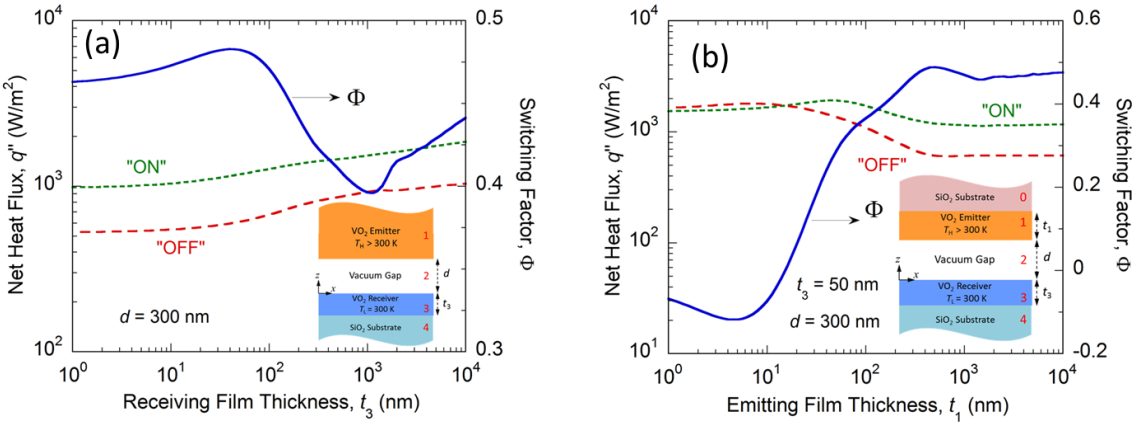

Figure 4.10 The radiative heat fluxes for both "on" (T_H = 341 K) and "off" modes (T_H = 342 K) as well as the switching factor at the vacuum gap of d = 300 nm: (a) the thickness effect of the thin VO_2 receiver (t_3) on SiO_2 substrate with a semi-infinite VO_2 emitter; (b) the thickness effect of the thin VO_2 emitter (t_1) with receiver thickness t_3 = 50 nm, both of which are deposited on SiO_2 substrate.

Finally, the thin-film and substrate effects for the emitter at the same vacuum gap distance d = 300 nm are also investigated. Figure 4.10(b) plots the radiative heat fluxes at varying emitting film thickness t_1 with the receiving film thickness t_3 = 50 nm for the proposed 5-layer radiative thermal switch design as illustrated in the inset. The radiative heat transfer is enhanced with a thin-film emitting VO_2 on SiO_2 substrate, in particular,

for the "off" mode for which the emitting VO_2 film is metallic. More interestingly, the radiative heat flux for the "off" mode (T_H = 342 K) actually becomes larger than that for the "on" mode (T_H = 341 K) with sub-10-nm ultrathin emitting films. Note that, as both the emitter and receiver are on SiO_2 substrate, the coupling between the emitting SiO_2 substrate to the receiver start to dominate the near-field radiative transport across the vacuum gap when the emitting VO_2 is extremely thin. Therefore, the optical property change due to the phase transition of the ultrathin VO_2 emitting film has negligible effect on the near-field heat transfer. The larger heat flux at the "off" mode than the "on" mode is simply due to the higher emitter temperature, resulting in negative switching factors. However, when the emitting VO_2 film is thicker, the coupling of the VO_2 film to the receiver becomes dominating. As a result, radiative heat fluxes at both modes decreases, and more importantly, the heat flux at the "off" mode decreases in a faster pace, which can be easily understood by the growing phase transition effect of VO_2 on modulating radiative heat transfer. The switching factor Φ increases with larger emitting film thickness, reaches a maximum of almost 0.5 at t_1 = 500 nm, and then saturates around 0.48, approaching the semi-infinite emitting VO_2 case with disappearing effect of film thickness. The effects of thin-film and substrates provide practical insights for experimental demonstration and further optimization of the proposed near-field radiative thermal switch in the future.

4.3 Graphene Based Near-Field Radiative Thermal Modulator

In this study, a hybrid near-field radiative thermal modulator made of two graphene-covered SiC plates separated by a nanometer vacuum gap is proposed. SiC is

chosen because it can support surface phonon polaritons in the mid-infrared, and graphene layers can be directly synthesized on the C-terminated SiC surface by thermally evaporating Si atoms [91, 92]. Similar to other graphene based near-field radiative transfer modulation, the proposed opto-electronic thermal modulator possesses fast operating speed, which is in principle only limited by electronics and not by the thermal inertia. To analyze the thermal modulation and switching functionalities, newly introduced quantities of the modulation factor, the sensitivity factor and the switching factor are studied extensively in a large parameter range for both graphene chemical potential and vacuum gap distance. As shown in Fig. 4.11, the SiC plate with a higher temperature (T_S = 400 K) and that with a lower temperature (T_D = 300 K) respectively act as the thermal emitter and receiver, separated by a vacuum gap with distance d.

The proposed radiative thermal modulator is realized via external voltage biases (i.e., V_{GE} for the emitter graphene and V_{GR} for the receiver graphene as depicted in Fig. 4.11) to tune chemical potentials of these two graphene sheets, which in turn modulate the near-field radiative heat flux, to be explained in detail below. Metallic layers deposited at the backsides of SiC plates are used as ground electrodes. Recent experimental progresses have succesfully demonstrated near-field radiation measurements between two flat surfaces separated by nanometer gaps [93-95]. Modulation of near-field spectral radiative flux with graphene chemical potentials will be first presented and the underlying physical mechanism is elucidated with fluctuational electrodynamics and dispersion relation of surface modes. Thermal modulation and switching effects, which are the key functionalities required for a thermal modulator, are

quantitatively realized and analyzed when the chemical potentials of emitter graphene and receiver graphene are the same or varied independently.

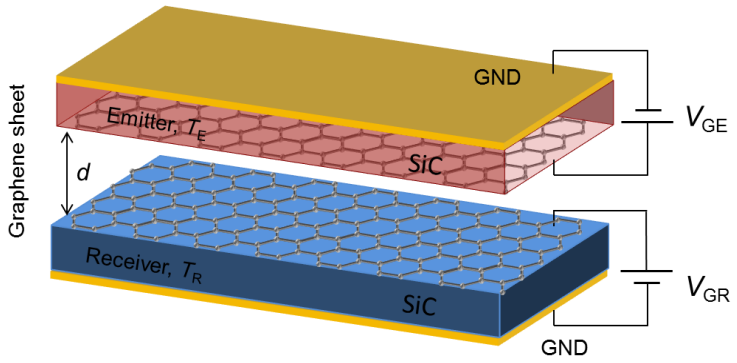

Figure 4.11 Schematic of proposed near-field radiative thermal modulator. The two SiC plates covered with monolayer graphene represent the thermal emitter and receiver, whose temperatures are set as T_E = 400 K and T_R = 300 K, respectively. The vacuum gap distance between the thermal emitter and receiver is denoted as d. Metal plates deposited at the backsides of SiC plates work as ground electrodes, for which voltage biases V_{GE} and V_{GR} are applied to respectively tune the chemical potentials of the emitter and receiver graphene sheets.

Fluctuational electrodynamics based on the stochastic nature of thermal emission [63] is used to calculate the near-field radiative heat flux of proposed radiative thermal modulator at different chemical potentials of both graphene sheets. When the SiC substrates are covered with graphene sheets, the Fresnel reflection coefficient at the interface between vacuum and medium i separated by a monolayer of graphene can be expressed as follows with the graphene surface conductivity [55, 96, 97]

$$r_{0i}^{p} = \frac{\varepsilon_i \gamma_0 - \gamma_i + \sigma(\omega)\gamma_0\gamma_i / (\omega\varepsilon_0)}{\varepsilon_i \gamma_0 + \gamma_i + \sigma(\omega)\gamma_0\gamma_i / (\omega\varepsilon_0)} \tag{4.3a}$$

$$r_{0i}^{s} = \frac{\gamma_0 - \gamma_i - \sigma(\omega)\mu_0\omega}{\gamma_0 + \gamma_i + \sigma(\omega)\mu_0\omega} \tag{4.3b}$$

where ε_0 and μ_0 are respectively the absolute electric permittivity and magnetic permeability of vacuum, and σ is the electrical conductivity of graphene sheet, whose expression can be found in Section 2.1. The dielectric function of bulk SiC is described by a Lorentz oscillator model as [64]

$$\varepsilon_{\mathrm{SiC}}(\omega) = \varepsilon_\infty \left(1 + \frac{\omega_{\mathrm{LO}}^2 - \omega_{\mathrm{TO}}^2}{\omega_{\mathrm{TO}}^2 - i\gamma\omega - \omega^2}\right) \tag{4.4}$$

where ε_∞ = 6.7 is the high-frequency constant, ω_{LO} = 1.83×10^{14} rad/s is the longitudinal optical-phonon frequency, ω_{TO} = 1.49×10^{14} rad/s is the transverse optical-phonon frequency, and γ = 8.97×10^{11} rad/s is the scattering rate at room temperature.

4.3.1 Modulation of spectral near-field radiative flux with μ

Let us first consider the symmetric case, in which both graphene sheets have the same chemical potentials, i.e., $\mu_{\mathrm{E}} = \mu_{\mathrm{R}} = \mu$. Figure 4.12(a) shows the spectral heat fluxes at d = 10 nm between the thermal emitter and receiver both covered by monolayer graphene with different μ values from 0 to 0.5 eV. Note that, the near-field spectral heat flux q_ω between two bare SiC plates exhibits a narrow peak with an amplitude around 300 $\mathrm{nW\cdot m^{-2}\cdot(rad/s)^{-1}}$ at ω_{SPhP} = 1.78×10^{14} rad/s, which was well understood as the surface phonon polariton (SPhP) coupling between SiC plates [7]. However, when

graphene with μ = 0 eV is coated onto both SiC plates, the high narrow peak at ω_{SPhP} disappears, while two broad spectral peaks with smaller magnitude around q_ω = 10 nW·m^{-2}·(rad/s)$^{-1}$ emerge with each at lower or higher frequencies along with a dip around ω_{ph}. The decrease of the spectral heat flux is caused by the suppression of SPhP coupling by the graphene plasmon, while similar behavior was observed for graphene covered SiO_2 plates [52]. Similar to the peak splitting of near-field spectral heat flux between two graphene-covered SiC plates, the splitting of local density of state at small distances from graphene covered SiC surface was also observed previously from the dispersion relations of surface modes [98]. The replacement of a single sharp spectral heat flux peak between bare SiC plates with two broad ones after covering graphene will enhance the total near-field radiative heat flux. When graphene chemical potential increases from μ = 0 to 0.5 eV, the low-frequency spectral peak becomes narrower and shifts from ω_1 = 4.5×10^{13} rad/s to 1.3×10^{14} rad/s, while the high-frequency mode becomes broader and moves from ω_2 = 1.8×10^{14} rad/s to 2.7×10^{14} rad/s. The shift of spectral heat flux peak to higher frequencies with greater chemical potentials is due to the μ effect on graphene plasmon, which varies the optical properties of graphene in the infrared regime. One the other hand, the chemical potential has little influence on the spectral heat flux dip around ω_{ph}.

It is known that the near-field radiative transfer between bare SiC plates is dominated by p-polarized evanescent waves where the SPhP coupling can be excited. For graphene-coated SiC plates, it is clearly shown in Fig. 4.12(b) that the p-polarized waves dominate the total near-field radiative transfer. The spectral heat flux q_ω from *p* polarization could be up to six orders of magnitude higher than that from *s* polarization in

most of spectral range considered here except at ω = 1.47×10^{14} rad/s, where the spectral heat flux from *s* polarization is slightly larger due to epsilon-near-pole mode of bulk SiC. Similar phenomenon is also observed in the local density of state near the graphene-covered SiC surface [98].

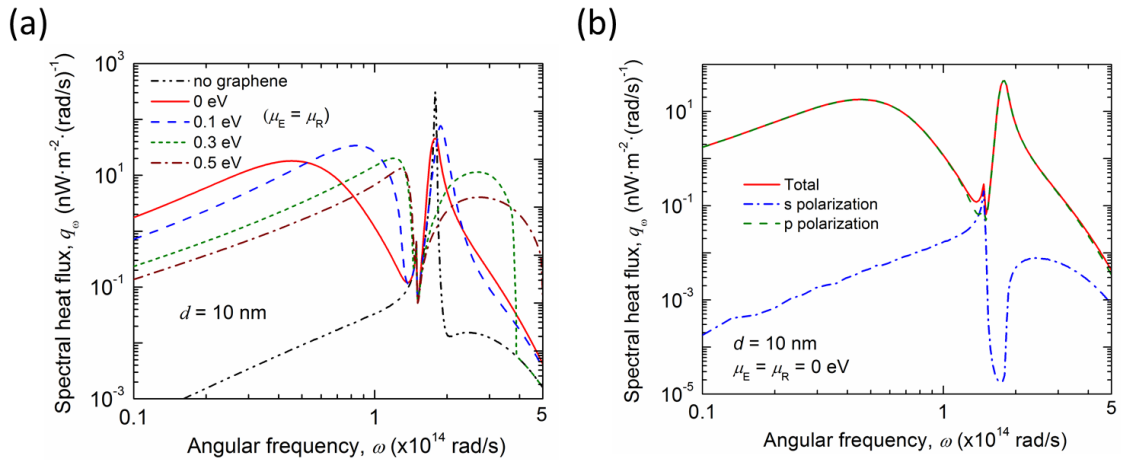

Figure 4.12 (a) Near-field spectral radiative heat fluxes q_ω between the thermal emitter and receiver at a vacuum gap of d = 10 nm when both the graphene sheets have the same chemical potential, i.e., $\mu_E = \mu_R$. The spectral heat flux between two bare SiC plates without graphene is also plotted for comparison. (b) The spectral heat flux from s-polarized, p-polarized, and unpolarized waves are presented separately for graphene-covered SiC plates with $\mu_E = \mu_R$ = 0 eV at d = 10 nm.

4.3.2 Near-field transmission probability and dispersion relation

The underlying mechanism for the peak splitting and shifting on q_ω with graphene coating is investigated through the contour plots of p-polarized transmission probability function at different chemical potential μ values, as presented in Fig. 4.13. The bright region represents the photon tunneling enhancement, which would lead to the

total heat transfer improvement. The vacuum gap distance is still set at d = 10 nm. It is well known that between two bare SiC plates, two branches of SPhP coupling exist around $\omega_{SPhP} = 1.78\times10^{14}$ rad/s [7]. However, due to the existence of graphene, the SPhP coupling disappears. Instead, four resonance branches that form two enhancement bands are observed from graphene-covered SiC plates for a given graphene chemical potential. Previous studies on the near-field coupling of graphene plasmon between graphene sheets on vacuum, doped silicon, or silica substrates only exhibited two resonant modes in the frequency-wavevector domain [52, 53, 55].

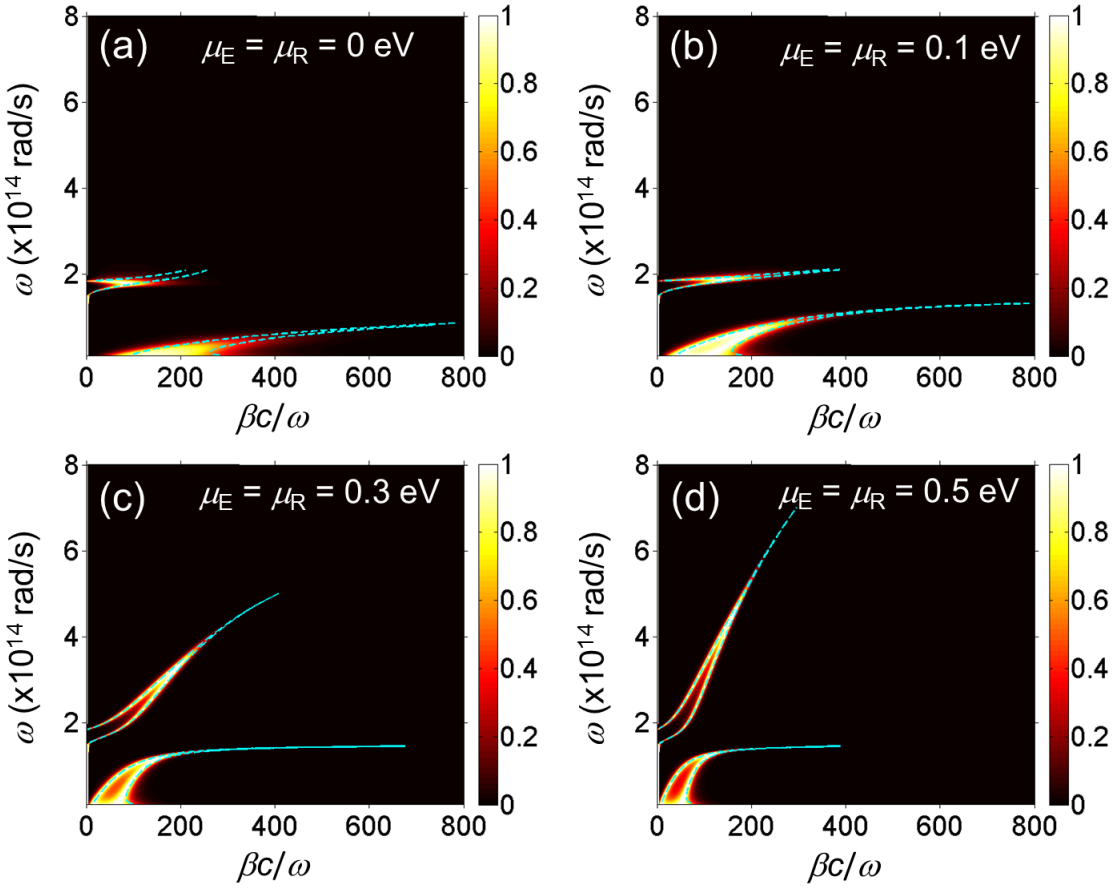

Figure 4.13 Contour plots of near-field transmission probability function between the thermal emitter and receiver at different chemical potentials applied to both graphene

sheets with the values of $\mu_E = \mu_R$ as: (a) 0 eV, (b) 0.1 eV, (c) 0.3 eV, and (d) 0.5 eV. The dispersion curves at the vacuum gap d = 10 nm are also plotted for confirmation of excitation of surface plasmon between graphene-covered SiC plates.

As the graphene chemical potential μ increases from 0 eV to 0.5 eV, both enhancement bands shift towards higher frequencies. For the high-frequency modes starting from around $\omega_2 = 2\times10^{14}$ rad/s, it will extend to around $\omega_2 = 5\times10^{14}$ rad/s at μ = 0.5 eV. The enhancement band becomes broader and transmission coefficient peak shifts to higher frequency, which is consistent with the observation in Fig. 4.12(a). However, for the low-frequency modes, a further increase of chemical potential beyond μ = 0.3 eV will not shift the resonance modes any more. Due to the suppression of SPhP modes, the low-frequency resonance modes caused by graphene SPP coupling have a saturation frequency around ω_{ph}.

To further confirm the effect of graphene plasmon on the near-field resonance modes, the SPP coupling dispersion curves between two graphene-coated SiC plates are plotted by zeroing the denominator of p-polarized transmission coefficient [99]

$$1 - r_{01}^{p} r_{02}^{p} e^{i2\gamma_0 d} = 0 \tag{4.5}$$

As shown in Fig. 4.13, there are four dispersion curves for a given μ value, which matches well with the four branches of enhanced transmission coefficient, confirming the effects of graphene plasmon on the near-field radiative transfer. When $\beta >> \omega/c_0$, $\gamma_0 \approx \gamma_1 \approx i\beta$. The Fresnel reflection coefficient for *p*-polarized waves in Eq. (4.3a) can be simplified to $r_{0i}^{p} \approx \dfrac{\varepsilon_i - 1 + i\beta\sigma(\omega)/(\omega\varepsilon_0)}{\varepsilon_i + 1 + i\beta\sigma(\omega)/(\omega\varepsilon_0)}$. Furthermore, if $\mathrm{Im}(\sigma)\beta/(\omega\varepsilon_0) >> 1$, r_{0i}^{p}

will be approaching to 1 with diminishing imaginary part, which will result in the decrease of transmission probability function to zero. As graphene chemical potential increases, Im(σ) will also increase, which results in the shift of the transmission probability function enhancement to higher angular frequency as presented in Fig. 4.13.

4.3.3 Characteristics of a near-field radiative thermal modulator

Let us now investigate major functionalities like thermal modulation and switching of heat flow from the proposed structure as a near-field radiative thermal modulator. The total radiative flux $q = \int_0^\infty q_\omega d\omega$ is obtained after integration with respect to angular frequency from ω = 1×10^{13} rad/s to 5×10^{14} rad/s as a function of chemical potential ($\mu = \mu_E = \mu_R$). The angular frequency integration range is chosen to include both SiC surface phonon and graphene plasmon, which can significantly enhance near-field radiative heat transfer as shown in Fig. 4.12. The spectral heat flux outside the considered frequency range is more than 2 orders of magnitude smaller than the spectral peak values, and therefore is negligible to the total heat flux. In order to quantify the thermal modulation effect of total radiative flux with graphene chemical potential μ, we introduce a dimensionless modulation factor as,

$$\Omega = q(\mu_S, \mu_D) / q_0 \tag{4.6}$$

where q_0 is the total heat flux when $\mu_E = \mu_R = 0$, which is considered as a reference here. At the vacuum gap of d = 10 nm, $q_0 = 1.8\ \mathrm{MW/m^2}$ for graphene-covered SiC plates in comparison with q_{SiC} = 1.05 MW/m^2 between two bare SiC plates. Instead of total radiative heat flux, the normalized modulation factor Ω is shown in Fig. 4.14(a) as a

function of graphene chemical potentials $\mu_E = \mu_R$. When μ increases from 0 eV, the modulation factor monotonically increases from 1 to the maximum $\Omega_{max} = 2.18$ at $\mu = 0.15$ eV, and then decreases to the minimum $\Omega_{min} = 0.29$ at $\mu = 1$ eV. In addition, the total radiative heat flux q at a vacuum gap of 100 nm, which is more practical to achieve than a 10-nm gap, is also calculated with different graphene chemical potentials while q_0 has a smaller value of 22.6 kW/m^2 under $\mu_E = \mu_R = 0$. However, the modulation factor Ω at $d = 100$ nm increases up to $\Omega_{max} = 2.52$ at $\mu = 0.75$ eV and then saturates around 2.5 up to 1 eV. Interestingly, by applying non-zero symmetric chemical potentials on graphene sheets, the radiative flux can be either amplified (i.e., $\Omega > 1$) or suppressed (i.e., $\Omega < 1$) at 10 nm vacuum gap. On the other hand, the radiative heat transfer can only be amplified at 100 nm gap distance if μ_E and μ_R are tuned identically.

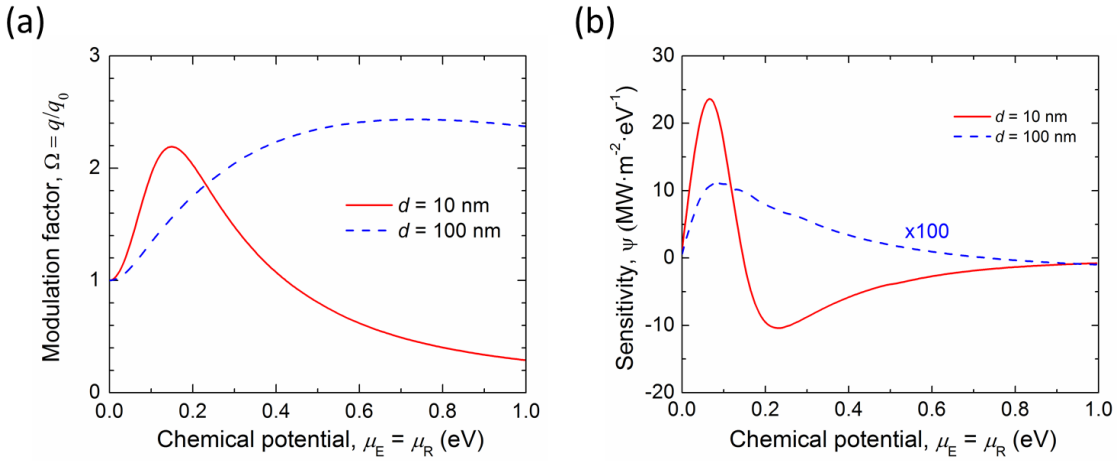

Figure 4.14 (a) Radiative heat modulation factor $\Omega = q/q_0$ and (b) sensitivity factor Ψ as a function of the identical chemical potential applied to both graphene sheets, i.e., $\mu_E = \mu_R$, at different vacuum gap distances of $d = 10$ nm and 100 nm.

In order to describe how sensitive the change of radiative heat flux is to the increment of graphene chemical potential, a sensitivity factor Ψ is defined as

$$\Psi = \partial q / \partial \mu_{\mathrm{D}} \tag{4.7}$$

which is essentially the slope of the total heat flux curve as a function of chemical potential. As shown in Fig. 4.14(b), at d = 10 nm when μ_{R} increases from 0 eV to 1 eV, the sensitivity factor increases first to the maximum $\Psi_{\max}$ = 24.4 MW·m^{-2}·eV^{-1} at μ_{R} = 0.06 eV, then decreases to 0 at 0.15 eV, where the total heat flux q reaches the maximum. As μ_{R} is beyond 0.15 eV, the sensitivity factor becomes negative due to the monotonous decrease of total heat flux with the increase of graphene chemical potential. The sensitivity factor achieves the minimum value of $\Psi_{\min}$ = –10.4 MW·m^{-2}·eV^{-1} at μ_{R} = 0.06 eV, and then monotonically increases to –0.77 MW·m^{-2}·eV^{-1}at 1 eV. When the vacuum gap distance changes to d = 100 nm, the total heat flux is about 2 orders of magnitude smaller than that at d = 10 nm due to the weaker surface plasmon coupling when the thermal source and drain are further apart. The sensitivity factor achieves $\Psi_{\max}$ = 0.12 MW·m^{-2}·eV^{-1} at μ_{R} = 0.08 eV, monotonically decreases to zero at μ_{R} = 0.75 eV, and finally reaches $\Psi_{\min}$ = –9.7 kW·m^{-2}·eV^{-1} at μ_{R} = 1 eV.

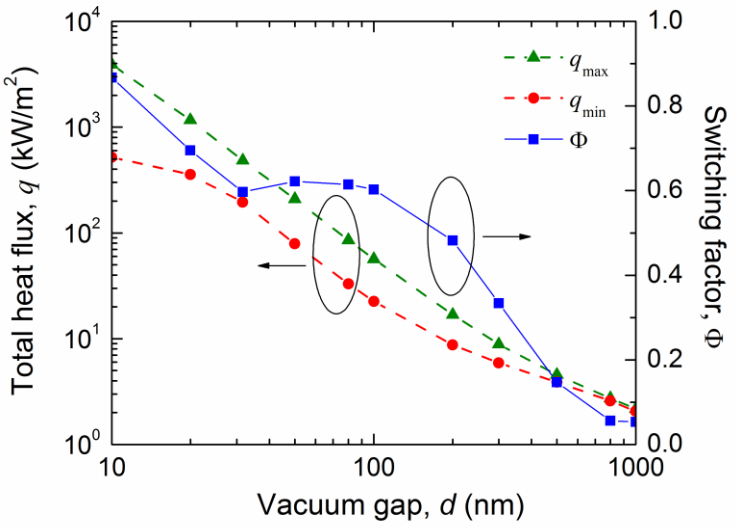

Figure 4.15 The maximum and minimum total heat fluxes along with the resulting thermal switching factor Φ as a function of vacuum gap distance d when the symmetric graphene chemical potentials ($\mu_E = \mu_R$) vary between 0 and 1 eV.

If the maximum $q_{max} = \Omega_{max} q_0$ and minimum total radiative flux $q_{min} = \Omega_{min} q_0$ are respectively treated to be the "on" or "off" mode to allow or forbid the heat flow to pass, the proposed thermal modulator could realize the function of thermal switching. To quantify how effectively the device could switch the heat flow, a switching factor defined as

$$\Phi = 1 - q_{min} / q_{max} = 1 - \Omega_{min} / \Omega_{max} \tag{4.8}$$

Therefore, a switching factor Φ = 0.87 is achieved at d = 10 nm with q_{max} = 3.92 MW/m^2 ($\mu_E = \mu_R$ = 0.15 eV) and q_{min} = 0.52 MW/m^2 ($\mu_E = \mu_R$ = 1 eV). Φ = 0.60 is for d = 100 nm where q_{max} = 56.7 kW/m^2 ($\mu_E = \mu_R$ = 0.75 eV) and q_{min} = 22.6 kW/m^2 ($\mu_E = \mu_R$ = 0 eV).

Figure 6 presents $q_{\max}$, $q_{\min}$, and Φ at different vacuum gap d from 10 nm to 1 μm when both graphene chemical potentials $\mu_E = \mu_R$ are varied symmetrically between 0 to 1 eV. The monotonic decrease of both $q_{\max}$ and $q_{\min}$ can be understood by weaker near-field coupling across the vacuum gap as the thermal emitter and receiver move further away. However, different from $q_{\max}$, which keeps increasing monotonically as d decreases, $q_{\min}$ saturates at d < 20 nm. The reason can be explained as that due to the strong SPP coupling between graphene sheets for $q_{\max}$, additional heat transfer modes are always available as d decreases, while for $q_{\min}$, the weakest SPP coupling sets a limit to the number of heat transfer modes, which results in the saturation of $q_{\min}$ at d < 20 nm [99]. Consequently, the switching factor Φ drops from 0.87 at d = 10 nm to 0.60 at d = 32 nm, stays around 0.62 till d = 100 nm, and then quickly decreases to 0.05 at 1 μm vacuum gap. The decrease of switching factor at d > 100 nm is because of the weaker impact of graphene chemical potential on modulating the radiative heat transfer as the near-field coupling becomes weaker at larger gap distances. The gap dependence suggests practical vacuum gaps between 32 nm to 100 nm for a thermal modulator with both strong switching effect and high near-field radiative flux.

4.3.4 Impact of asymmetric chemical potentials ($\mu_E \neq \mu_R$)

In order to possibly obtain stronger thermal modulation and switching effects, we now consider different chemical potentials of the graphene sheets on the thermal emitter and receiver, i.e., $\mu_E \neq \mu_R$. Figures 4.16(a) and 4.16(b) present the contour plots of modulation factor Ω as a function of μ_E and μ_R independently varied from 0 to 1 eV at d

= 10 nm and 100 nm, respectively. Clearly, the largest modulation in near-field radiative flux is obtained at $\mu_E = \mu_R$ under which the surface plasmon coupling is strongest due to best-matching optical properties between graphene covered thermal emitter and receiver. The maximum modulation factor Ω_{max} is 2.18 at $\mu_E = \mu_R = 0.15$ eV for d = 10 nm and 2.52 at 0.75 eV for 100 nm gap distance. However, with asymmetric chemical potentials, the near-field radiative flux could reach smaller values due to weaker coupling, leading to a smallest modulation factor $\Omega'_{min} = 0.06$ at d = 10 nm with asymmetric chemical potentials (μ_E = 1 eV, μ_R = 0.15 eV), which is much lower than $\Omega_{min} = 0.29$ with symmetric μ*'s*. Similarly, at d = 100 nm, a smaller $\Omega'_{min} = 0.38$ is under with μ_E = 1 eV and μ_R = 0.12 eV. Obviously, the asymmetric structure provides more flexibility to modulate the heat flux between the thermal emitter and receiver. As a result, larger switching factors $\Phi' = 0.97$ and 0.85 are obtained respectively at d = 10 nm and 100 nm with asymmetric tuning of emitter and receiver graphene chemical potentials.

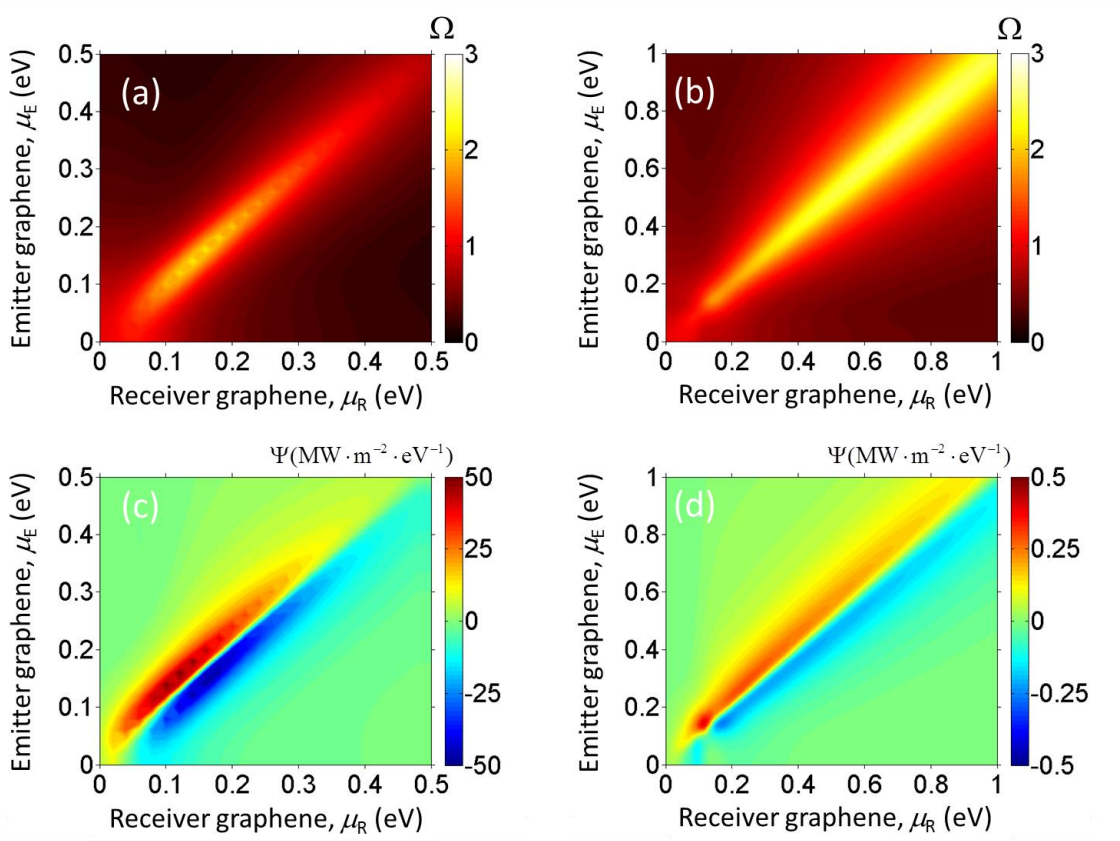

Figure 4.16 Contour plots of the modulation factor $\Omega = q/q_0$ between the thermal emitter and receiver under the asymmetric case as a function of different chemical potentials applied to the two graphene sheets at a vacuum gap of (a) d = 10 nm and (b) 100 nm. Contour plots of thermal sensitivity factor Ψ as a function of asymmetric emitter and receiver graphene chemical potentials μ_E and μ_R at a vacuum gap of (c) d = 10 nm and (d) 100 nm.

The thermal sensitivity factors Ψ under asymmetric chemical potentials are shown in Figs. 4.16(c) and 4.16(d) respectively for 10 nm and 100 nm vacuum gaps. Note that for asymmetric case, Ψ is defined as the derivative of q to μ_R as shown in Eq. (4.7), while μ_E is fixed at a constant. It can be clearly observed that the amplitude $|\Psi|$ is

almost symmetric along the diagonal line where $\mu_E = \mu_R$, while Ψ is positive with increasing heat flux when $\mu_E > \mu_R$, and vice versa. Compared to the symmetric case, a much higher maximum thermal sensitivity factor $\Psi'_{max} = 50.2$ MW·m^{-2}·eV^{-1} is achieved at μ_E = 0.16 eV and μ_R = 0.12 eV for d = 10 nm. While for d = 100 nm, $\Psi'_{max} = 0.4$ MW·m^{-2}·eV^{-1} is achieved at μ_E = 0.15 eV and μ_R = 0.12 eV.

CHAPTER 5 NEAR-FIELD MAGNETIC POLARITONS EXCITED IN NANOMETRIC VACUUM GAP

It has been demonstrated during the last decade that radiative transfer could be significantly enhanced when distance between two objects is smaller than the characteristic thermal wavelength due to photon tunneling or coupling of evanescent waves [43, 44, 64]. In particular, near-field radiative flux could far exceed the blackbody limit by the resonant coupling of surface plasmon/phonon polaritons (SPP/SPhP) across the vacuum gap both theoretically and experimentally [99, 100]. Recently, excitations of magnetic SPhP [101, 102], hyperbolic modes [78, 103, 104], and epsilon-near-pole or epsilon-near-zero modes [105] with different types of metamaterials have also been studied to further improve the near-field radiative flux. Moreover, compared to the case of two plates, the near-field radiative transport between two gratings can be further enhanced due to guided modes [106] and spoof surface plasmon polaritons [107] between two Au gratings at a large vacuum gap distance of 1 μm, and hyperbolic modes between two doped silicon gratings [108]. Near-field thermal radiation could find many promising applications in energy-harvesting [64, 109], near-field imaging [110], and thermal management [47, 50, 72, 111-113]. Several experimental methods have been reported to measure near-field radiative heat flux between planar surfaces at sub-micron vacuum gaps [93-95].

5.1 Spectral Heat Flux

5.1.1 Spectral heat flux at d = 100 nm and numerical validation

Magnetic polaritons (MP) refer to the strong coupling of external electromagnetic

waves with the magnetic resonance excited inside the nanostructures. MP artificially realized with metallic micro/nanostructures has been employed to control light propagation and tailor exotic optical and radiative properties in the far field, such as thermophotovoltaic emitter [74], and switchable or tunable metamaterial [28, 29]. Phonon-mediated MP have also been excited in both SiC deep grating and binary grating configurations as well [81]. On the other hand, the MP excitation has been achieved in the SiO_2 spacer between two Ag binary gratings [114]. In comparison to SPP/SPhP that has been well studied for tailoring both far- and near-field thermal radiation, magnetic resonance or MP has only been investigated for controlling far-field thermal radiation while its role in near-field radiative transport has yet to be identified. In this section, we will theoretically investigate the possible effect of MP in near-field radiative transfer between two metallic grating microstructures separated by a vacuum gap d below 100 nm.

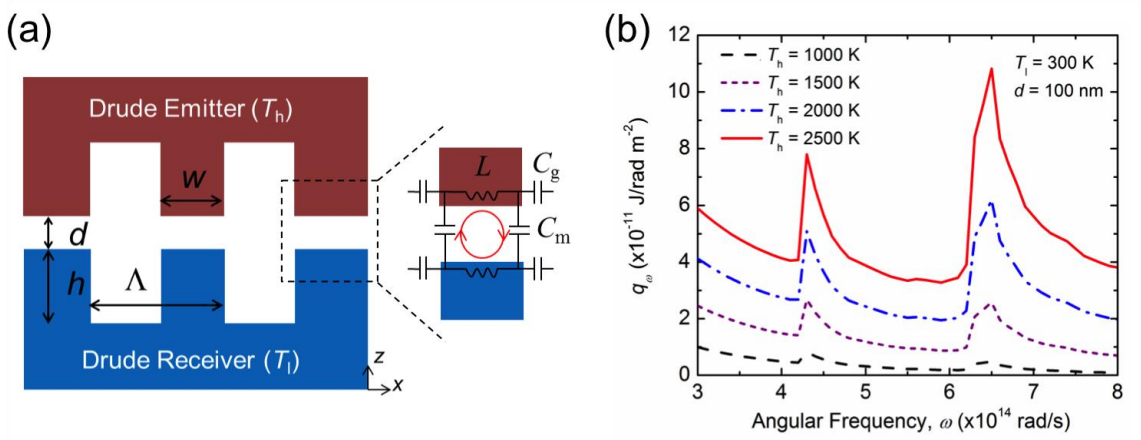

Figure 5.1 (a) Schematic of radiative transfer between two symmetric, perfectly aligned metallic gratings with parameters of period ($\Lambda = 2$ μm), depth (h = 1 μm), and ridge width (w = 1 μm). The Drude emitter and receiver temperatures are respectively set as T_h and T_l. The vacuum gap distance is denoted as d. An equivalent LC circuit model and the

resulting electrical current loops in the vacuum gap at excitation of magnetic polariton (MP) are also depicted. (b) Spectral heat fluxes between these two perfectly aligned metallic gratings at different emitter temperatures when the receiver is separated by a vacuum gap of d = 100 nm and maintained at T_l = 300 K.

As depicted in Fig. 5.1(a), the gratings are assumed to be perfectly aligned with period, depth, and ridge width respectively as Λ = 2 μm, h = 1 μm, and w = 1 μm, which are kept unchanged in the present work unless specified. Vacuum is considered to be in the grating grooves, while the metal filling ratio is then $f = w/\Lambda = 0.5$. The temperatures of the emitter and receiver are set as T_h and T_l, respectively. Note that an equivalent inductor-capacitor (LC) circuit model, which has been widely used to predict the MP resonance frequency in far field [114], is also shown in Fig. 5.1(a) along with the resulting current loop. The question is that whether MP resonance can be excited in the nanometer vacuum gap to spectrally enhance near-field radiative transfer. To address this question, the scattering formalism [115-117] that is incorporated into fluctuational electrodynamics with rigorous coupled-wave analysis (RCWA) [60, 61] is employed to rigorously calculate the near-field radiative flux. The dielectric function of the metals is described by a Drude model as $\varepsilon_{\text{Drude}}(\omega) = 1 - \dfrac{\omega_p^2}{\omega^2 + i\gamma\omega}$, where ω is the angular frequency, the plasma frequency is ω_p = 1.37×10^{16} rad/s, and scattering rate is γ = 7.31×10^{13} rad/s[14], which are taken from the material properties of gold at room temperature as an example here. While the present study mainly focuses on the explanation of the physical mechanism and behavior of MP resonance in the near-field

radiative transfer, similar MP excitation is expected to occur with other metals like Ag, Al, W [26, 27, 32], as well as some refractory plasmonic materials like ITO, AZO and TiN, which could possibly withstand high temperatures up to 3250 K [11].

Through the exact scattering theory, near-field spectral radiative transfer between two gratings is expressed as [118, 119]

$$q_w = \frac{1}{2p^3}\left[\Theta_h(w,T_h) - \Theta_l(w,T_l)\right]\int_0^{p/L}\int_0^{\infty} x(w,k_{x0},k_y)dk_y dk_{x0} \tag{5.1}$$

where $\Theta(\omega,T) = \hbar\omega/\left(e^{\hbar\omega/k_BT}-1\right)$ is the Planck oscillator, and k_{x0} and k_y are the incident wavevector components at the grating surface in the x and y directions, respectively. The energy transmission coefficient $\xi(\omega, k_{x0}, k_y)$, which considers all the polarization states, is

$$\xi\left(\omega,k_{x0},k_y\right) = \mathrm{tr}\left(\mathbf{D}\mathbf{W}_1\mathbf{D}^{\dagger}\mathbf{W}_2\right) \tag{5.2a}$$

$$\mathbf{D} = \left(\mathbf{I}-\mathbf{S}_1\mathbf{S}_2\right)^{-1} \tag{5.2b}$$

$$\mathbf{W}_1 = \Sigma_{-1}^{pw} - \mathbf{S}_1\Sigma_{-1}^{pw}\mathbf{S}_1^{\dagger} + \mathbf{S}_1\Sigma_{-1}^{ew} - \Sigma_{-1}^{ew}\mathbf{S}_1^{\dagger} \tag{5.2c}$$

$$\mathbf{W}_2 = \Sigma_1^{pw} - \mathbf{S}_2^{\dagger}\Sigma_1^{pw}\mathbf{S}_2 + \mathbf{S}_2^{\dagger}\Sigma_1^{ew} - \Sigma_1^{ew}\mathbf{S}_2 \tag{5.2d}$$

where **D** is the so-called Fabry-Perot denominator considering multiple reflection between two gratings, $\mathbf{W}_i$ indicate the photon absorption, $\mathbf{S}_1 = \mathbf{R}_1$, and $\mathbf{S}_2 = e^{ik_{z0}d}\mathbf{R}_2 e^{ik_{z0}d}$. $\mathbf{R}_1$ and $\mathbf{R}_2$ are the reflection operators of the two gratings, which can be obtained through RCWA method [60-62]. $k_x^{(n)} = k_{x0} + n\frac{2\pi}{\Lambda}$ is defined according to the Bloch wave condition. *n* runs from *–N* to *N*, where *N* is the highest diffraction order. The operators $\Sigma_n^{pw/ew} = \frac{1}{2}k_z^n\Pi^{pw/ew}$, where $\Pi^{pw/ew}$ are the projectors on the propagative and evanescent

sectors, were clearly defined in Ref. [118]. To ensure the numerical accuracy of the calculation with reasonable computational time, a total of 51 angular frequency values evenly spanned from 3×10^{14} rad/s to 8×10^{14} rad/s was considered, while 21 and 121 data points were respectively used for k_{x0} and k_y with the upper limit of k_y set as $100\omega/c$ at d = 100 nm. A total of 361 diffraction orders (i.e., N = 180) were applied to calculate the spectral heat flux with a relative error smaller than 5% compared to that obtained with N = 300. The numerical results obtained by the scattering matrix theory are treated to be rigorous.

Figure 5.1(b) presents the spectral heat fluxes between two metallic gratings at a vacuum gap distance of d = 100 nm with different emitter temperatures T_h from 1000 K to 2500 K when the receiver temperature is fixed at T_l = 300 K. There clearly exist two spectral heat flux peaks around angular frequencies of 4.3×10^{14} rad/s and 6.5×10^{14} rad/s. As T_h increases, the spectral peak locations surprisingly do not change, while the peak amplitudes are greatly enhanced mainly due to more energetic Planck oscillator at higher temperatures. For example, the spectral heat flux q_ω at the frequency of 6.5×10^{14} rad/s could reach as high as 1.1×10^{-10} J/rad m^{-2} at T_h = 2500 K. Note that, the angular frequency of 6.5×10^{14} rad/s corresponds to 0.43 eV in energy, thus the observed spectral heat flux peaks could possibly greatly improve the thermophotovoltaic (TPV) energy conversion by spectrally enhancing photon transport above the bandgaps of TPV cells (e.g., $In_xGa_{1-x}As$ with band gaps varying from 0.36 eV to 1.42 eV).

To validate our numerical calculations, we used our algorithm to calculate the radiative heat transfer between two Au gratings with large gap distances in Fig. 5.2 to compare the results in Ref. [106]. This figure shows the transmission coefficient between

two gold gratings as a function of angular frequency at a single wavevector point of **k** = ($\pi/2\Lambda$, 0). The parameters are grating period Λ = 2.5 μm, width w = 1.25 μm, depth h = 1.5 μm and the vacuum gap distance is d = 1 μm. The results show consistency when compared with those in Ref. [106], which validates the numerical method in our work. Note that the same dielectric function for gold has been used to reproduce the results.

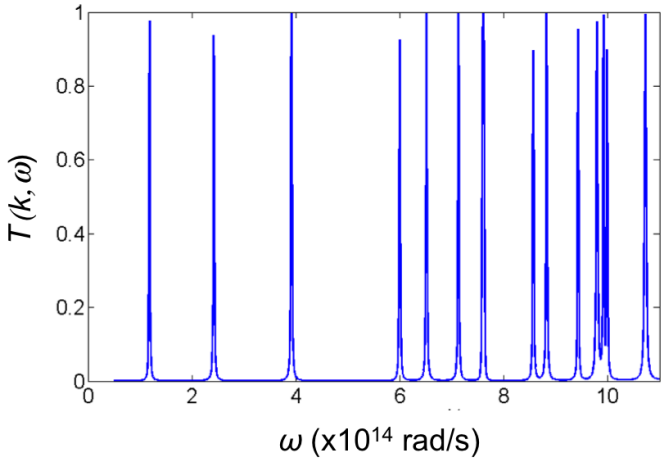

Figure 5.2 The spectral transmission factor between two gold gratings at the vacuum gap distance d = 1 μm with period Λ = 2.5 μm, grating width w = 1.25 μm and corrugation depth h = 1.5 μm.

5.1.2 Spectral heat flux at different vacuum gaps and comparison with PA and EMT

In order to understand the physical mechanisms responsible for these two spectral heat flux peaks, we first investigate the spectral heat fluxes at different vacuum gap distances of d = 100 nm, 50 nm, 20 nm and 10 nm as shown in Fig. 5.3. As the Planck oscillator only considers the effect of temperature, the spectral heat flux q_ω is normalized to the Planck oscillator difference $\Theta_h - \Theta_l$ in order to directly indicate the effects of materials and structures on the radiative transfer, which would better reveal the

underlying mechanisms. It can be clearly observed from Fig. 5.3(a) that, at a vacuum gap distance of d = 100 nm, there are two peaks of normalized spectral heat flux at angular frequencies of 4.3×10^{14} rad/s and 6.5×10^{14} rad/s, respectively. When d decreases to 50 nm the larger peak shifts to $\omega = 6.0\times10^{14}$ rad/s, and further to 5×10^{14} rad/s at d = 20 nm. However, when d becomes 10 nm, there are two spectral peaks respectively at the frequencies of 4×10^{14} rad/s and 7.8×10^{14} rad/s, in addition to the small spectral peak around $\omega = 4.3\times10^{14}$ rad/s, whose frequency does not change at all at different vacuum gaps but the peak amplitude increases from 0.5×10^{10} $rad^{-1}\cdot m^{-2}$ at d = 100 nm to 1×10^{11} $rad^{-1}\cdot m^{-2}$ at d = 10 nm.

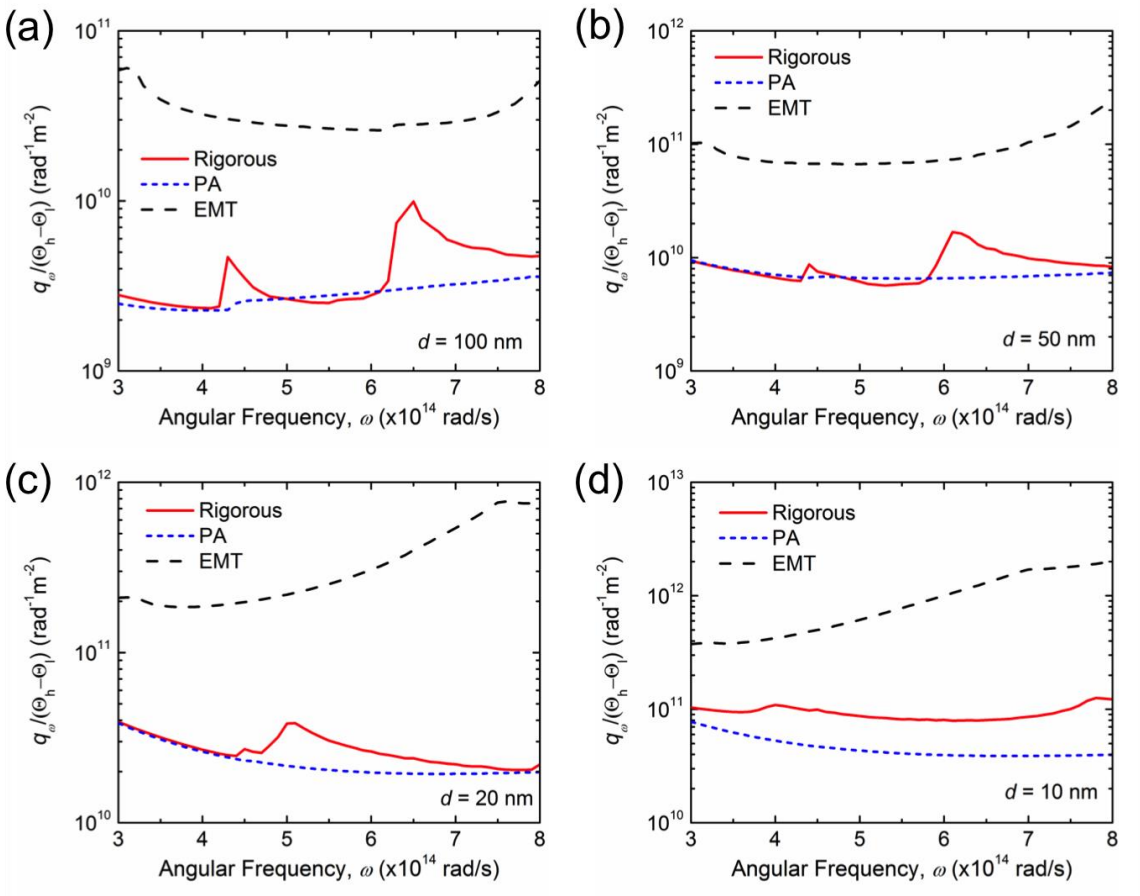

Figure 5.3 Normalized spectral heat fluxes between the Drude grating emitter and receiver at different vacuum gaps of (a) d = 100 nm, (b) d = 50 nm, (c) d = 20 nm, and (*d*) d = 10 nm, obtained from the scattering matrix method (denoted as "Rigorous") in comparison with those from Derjaguin's proximity approximation method (denoted as "PA") and effective medium theory (denoted as "EMT").

In order to understand the physical mechanisms responsible for the normalized spectral heat flux peaks predicted by the rigorous calculation, the Derjaguin's proximity approximation (PA) method, which represents a weighted approach for SPhP or SPP coupling with different vacuum gap distances, is first considered. The spectral heat flux between two gratings from the PA method can be weighted by the ones between two plates with different gap distances as

$$q_\omega^{\mathrm{PA}} = f \times q_\omega^{\mathrm{plate}}(d) + (1-f) \times q_\omega^{\mathrm{plate}}(d+2h) \tag{5.3}$$

where $q_\omega^{\mathrm{plate}}(L)$ means the spectral heat flux between two plates with a gap distance L. As inferred by Eq. (5.3), the PA method only considers the contributions by SPP coupling between planar surfaces at different vacuum gap distances. This indicates that the PA method would be accurate if coupled SPhP or SPP resonance is the only mechanism that dominates near-field radiative transfer as discussed in Fig. 5.4. However, by comparing the normalized spectral heat flux from the PA method to the rigorous solution in Fig. 5.2, the PA method turns out to be accurate with good agreement with the rigorous solution except for the angular frequencies where spectral heat flux peaks exist for d from 100 nm to 20 nm. At d = 10 nm, the PA method fails to predict the exact values by significant discrepancies within the entire spectrum of interests. Apparently, the PA method or the

SPP coupling between planar surfaces cannot explain the spectral heat flux peaks that exist between metallic gratings.

Furthermore, the effective medium theory (EMT), which considers the grating layer as a homogeneous uniaxial medium, is also examined to see whether or not it is responsible for the spectral enhancement. By setting the diffraction order to zero in the RCWA algorithm, the metallic gratings are considered as effectively homogenous media with zero-order approximation with more details discussed in Figs. 5.5 and 5.6. The near-field radiative flux between the metallic gratings with effective media approximation was also calculated and presented in Fig. 5.2 with different vacuum gaps. Comparing with the rigorous method, the EMT method overpredicts the normalized spectral heat flux by one order of magnitude, which is due to the enhancement from the hyperbolic modes unnecessarily predicted by the effective medium treatment [See the Supplemental Materials]. After all, EMT is inherently a homogenization approach which cannot take into account the local resonance modes like coupled SPP or MP that could possibly occur within the vacuum gap [108, 120, 121]. Therefore, effective medium approximation cannot explain the unusual radiative transfer between the metallic gratings across ultrasmall vacuum gaps, while physical mechanisms other than coupled SPP or EMT have to be identified and understood.

Derjaguin's proximity approximation (PA) method represents a weighted approach when coupled SPP or SPhP modes are the main mechanisms for the radiative transport across nanometer vacuum gaps. It is expected that, the PA method should be able to predict the radiative heat transfer between grating structures reasonably accurately

without magnetic polariton excitation in comparison with the rigorous results from the scattering matrix method.

Figure 5.4 shows the normalized spectral heat fluxes obtained from both the scattering matrix theory and the PA method between either two SiO_2 gratings or metallic gratings. As shown in Fig. 5.4(a), the SPhP coupling between SiO_2 gratings at d = 100 nm can be predicted well by both scattering theory and PA method [2]. Even considering the spectral heat flux between two metallic gratings (Λ = 2 μm, w = 1 μm, h = 1 μm) in Fig. 5.4(b), the results are also consistent between the rigorous method and the PA method at the lower angular frequency range where magnetic polariton excitation is absent. This also further validates numerical calculations from the scattering matrix method with grating structures in this work.

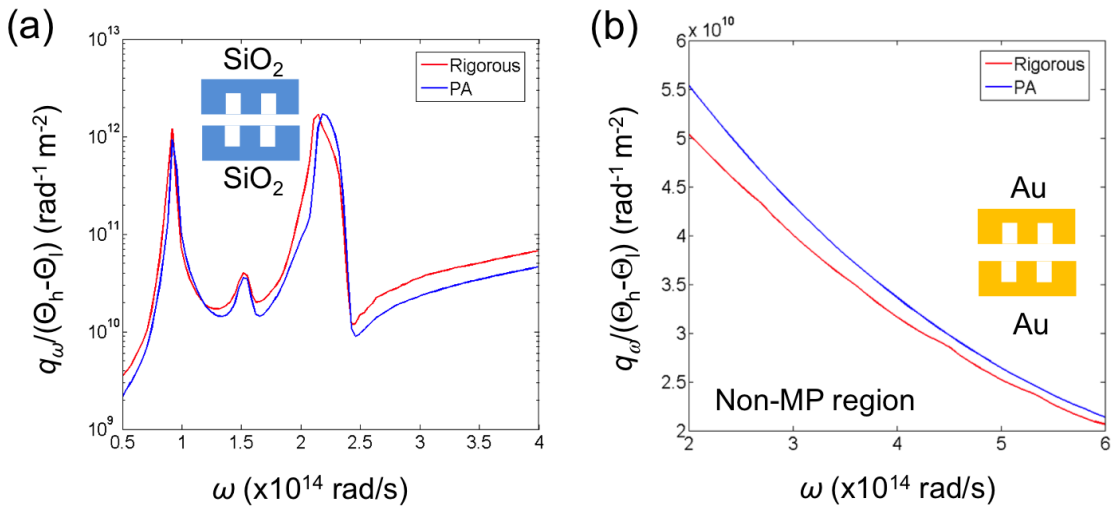

Figure 5.4 Normalized spectral heat fluxes between (a) two SiO_2 gratings and (b) two metallic gratings (denoted as rigorous) at vacuum gap of d = 100 nm. The SiO_2 grating geometry is Λ = 0.5 μm, w = 0.2 μm and h = 0.5 μm, which follows that in Ref. [2],

while that for metallic gratings is Λ = 2 μm, w = 1 μm and h = 1 μm. The normalized spectral heat flux obtained from the PA method is also present.

On the other hand, the radiative heat transfer between two metallic gratings can be approximated using the effective medium theory (EMT), which homogenizes the grating layer as a uniaxial thin film. The effective dielectric functions of the homogenized grating region are expressed as

$$\varepsilon_{\mathrm{O}} = (1-f) + \varepsilon_{\mathrm{Au}} f \tag{5.4a}$$

$$\varepsilon_{\mathrm{E}} = \frac{\varepsilon_{\mathrm{Au}}}{(1-f)\varepsilon_{\mathrm{Au}} + f} \tag{5.4b}$$

where the subscript "O" and "E" denote the ordinary and extraordinary component of dielectric function, respectively. As the optical axis of considered grating structure is along x axis, it gives $\varepsilon_{xx} = \varepsilon_{\mathrm{E}}$, and $\varepsilon_{yy} = \varepsilon_{zz} = \varepsilon_{\mathrm{O}}$. The real parts of both components for a filling ratio of f = 0.5 are presented in Fig. 5.5. Clearly, $\varepsilon_{\mathrm{O}} < 0$ and $\varepsilon_{\mathrm{E}} > 0$ at the frequency range 3×10^{14} rad/s < ω < 8×10^{14} rad/s, indicating hyperbolic behavior within this spectral region.

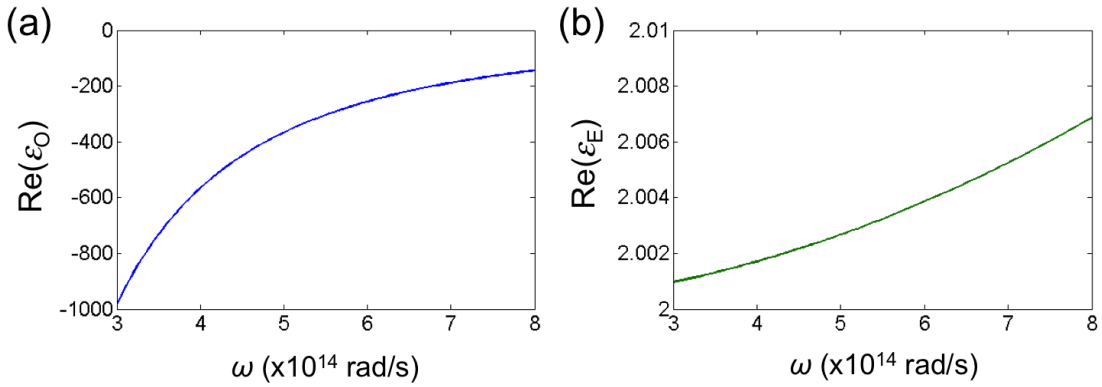

Figure 5.5 Real parts of effective dielectric functions of metallic gratings: (a) ordinary component ε_O and (b) extraordinary component ε_E. Note that the filling ration is $f = 0.5$.

A straightforward way to treat grating layer as an effectively homogenized layer is to set the diffraction order in the RCWA method to be 0, as the 0th order solution of the rigorous method basically considers the grating as an effective medium. The same approach has also been applied to calculate near-field radiative transfer between other nanostructures previously [120]. However, it should be noticed in Eq. (5.1) for the rigorous method that the integration range for k_{x0}, which is from 0 to π/Λ, can be extended to a much larger k_x range through Bloch wave condition $k_x^{(n)} = k_{x0} + 2n\pi/\Lambda$ for periodic gratings with sufficient diffraction orders N. However, when $N = 0$ is set for the EMT calculation by treating the periodic gratings as a homogenous layer, a sufficiently larger range is needed for k_{x0} in order to ensure the calculation accuracy instead of the previous k_{x0} range from 0 to π/Λ. The convergence check on the k_{x0} range for the near-field radiative transfer with effective medium approximation was performed by increasing the number of data (or mk_{x0}) and the upper limit (or k_{x0_max}) on k_{x0}. Note that 51 angular frequency data points are evenly distributed from 3×10^{14} rad/s to 8×10^{14} rad/s, and a total of 1000 data points is set for k_y from 0 to $20\omega/c_0$ at each angular frequency.

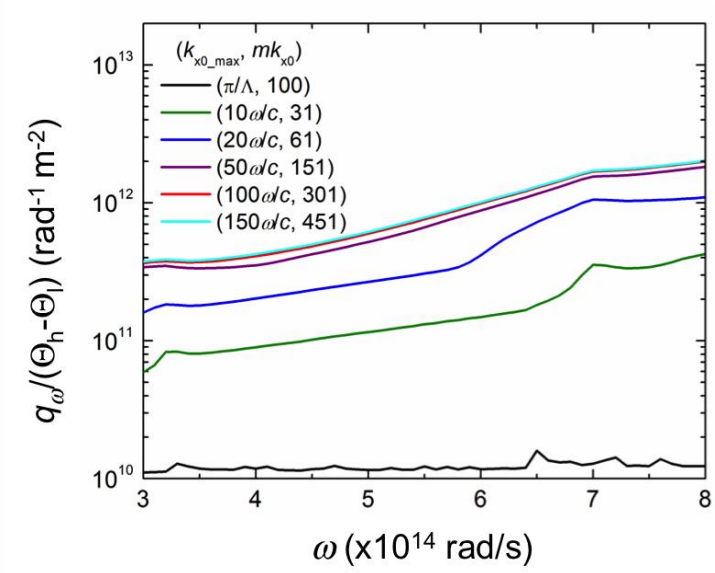

Figure 5.6 Normalized spectral heat fluxes between two metallic gratings at d = 10 nm through the effective medium method with different ranges for k_{x0}. The dielectric function of the metal follows the Drude model. The grating geometry is Λ = 2 μm, h = 1 μm, w = 1 μm.

Figure 5.6 presents the normalized spectral heat flux between two metallic gratings at d = 10 nm with different k_{x0} ranges. It can be clearly observed that the calculation is converged with k_{x0_max} = 100ω/c_0 and mk_{x0} = 301, which has a relative difference within 3% compared to that with k_{x0_max} = 150ω/c_0 and mk_{x0} = 451. The computation time is about 2 hours on a workstation with a 12-core 3.1 GHz processor and 64 GB memory. Similar convergence check has been done for all other vacuum gap distances to ensure the accuracy.

5.2 Contour Plot of Transmission Coefficient

5.2.1 Effect of vacuum gap distance and substrate

To gain a better idea on the radiative transfer between the Drude grating emitter and receiver, the contour plots of transmission coefficient in the ω - k_{x0} domain under k_y = 0 from the rigorous method are presented in Fig. 5.7 at corresponding vacuum gap distances. Multiple bright horizontal bands, which are independent of k_{x0} and indicate the enhanced near-field radiative transfer channels, can be clearly observed. Among different vacuum gap distances, the one at $\omega = 4.3\times10^{14}$ rad/s barely shifts with different d values, which is corresponding to the smaller spectral heat flux peak at the same frequency observed in Fig. 5.3. As intensively discussed in Ref.[106], this is associated with the guided mode, whose resonance condition strongly depends on the cavity depth, i.e. $H = 2h+d$. Note that the grating depth is h = 1 μm, which is much larger than the sub-100-nm vacuum gap distances considered here. Therefore, it can be understood that, the guide mode would not shift when d varies from 100 nm to 10 nm as $H \gg d$. However, the same theory of guided modes cannot explain the brighter and broader resonance mode around $\omega = 6.5\times10^{14}$ rad/s at d = 100 nm, which clearly shifts to lower frequencies with smaller d. As the coupled SPP, effective medium and guided modes cannot explain this particular unusual spectral enhancement between metallic gratings, could it be associated with possible excitation of magnetic resonance or MP?

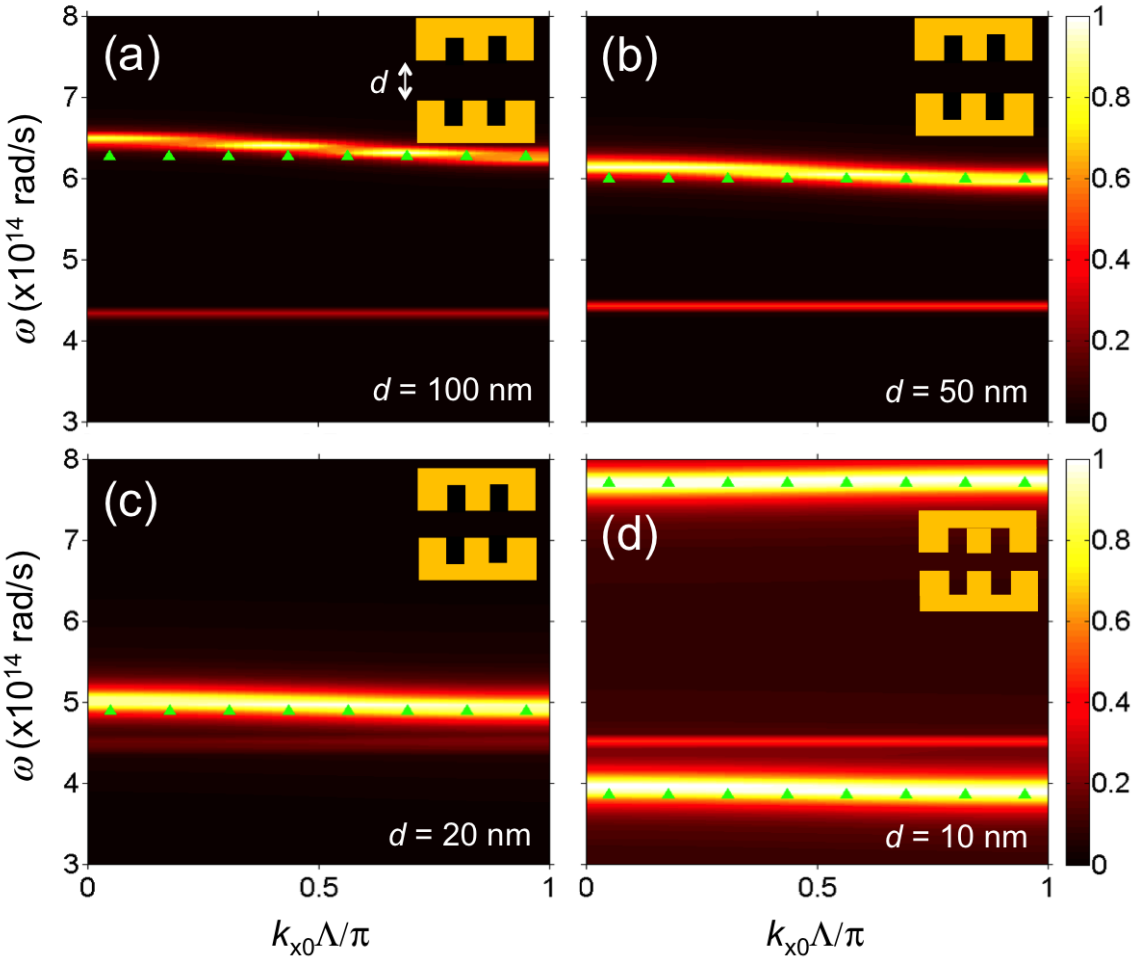

Figure 5.7 Contour plots of energy transmission coefficient (ξ) between the Drude grating emitter and receiver at vacuum gaps of (a) d = 100 nm, (b) d = 50 nm, (c) d = 20 nm, and (d) d = 10 nm. The base geometric parameters of the metallic gratings are Λ = 2 μm, w = 1 μm, and h = 1 μm. Note that k_y = 0 is assumed and k_{x0} is normalized to the first Brillouin zone. The LC circuit model prediction of MP resonance conditions is shown as green triangles.

In order to verify our hypothesis of MP resonance, an equivalent LC circuit is employed to analytically predict the resonance conditions of MP between two metallic gratings in near field [114]. Note that the LC model, based on the resonant charge

distributions, has been successfully employed to verify the physical mechanisms of MP modes in metal-insulator-metal (MIM) nanostructures in selective control of far-field thermal radiation . After all, the nanometer vacuum gap between the Drude grating emitter and receiver here forms similar MIM configurations. Here, the inductance of the metallic gratings can be expressed as $L = L_{\mathrm{m}} + L_{\mathrm{e}}$, where the first term $L_{\mathrm{m}} = 0.5\mu_0 wd$ accounts for the mutual inductance of two parallel plates with width *w* separated by a distance *d*, and the kinetic inductance $L_{\mathrm{e}} = \omega/(\varepsilon_0 \omega_p^2 \delta)$ considers the contribution of drifting electrons. Note that μ_0 and ε_0 are the permeability and permittivity of vacuum, while $\delta = \lambda/2\pi\kappa$ is the field penetration depth with κ being the extinction coefficient of the metal. On the other hand, the parallel-plate capacitance between the upper and lower metal ridges can be expressed as $C_{\mathrm{m}} = c_1 \varepsilon_0 w/d$, where c_1 = 0.22 is the correction factor considering non-uniform charge distribution [114]. The capacitance between left and right metal ridges is denoted as $C_{\mathrm{g}} = \varepsilon_0 h/(\Lambda - w)$. Thus, the resonance frequency for the fundamental MP mode can be obtained when the total circuit impedance reaches zero:

$$\omega_{\mathrm{MP1}} = 1/\sqrt{(L_{\mathrm{m}} + L_{\mathrm{e}})(C_{\mathrm{m}} + C_{\mathrm{g}})} \tag{5.5}$$

With the base grating geometries as Λ = 2 μm, *w* = 1 μm, *h* = 1 μm, the MP1 resonance frequencies between the Drude grating emitter and receiver are predicted to be 6.4×10^{14} rad/s, 6.0×10^{14} rad/s, 4.9×10^{14} rad/s, and 3.8×10^{14} rad/s respectively for *d* = 100 nm, 50 nm, 20 nm, and 10 nm, which match surprisingly well with the unusual spectral enhancement mode predicted by the rigorous solution as shown in Fig. 5.7. Note that the independence of the MP resonance condition on the k_{x0} has been thoroughly discussed and well understood previously . At *d* = 10 nm, the contour shows an additional

resonance mode around $\omega = 7.7\times10^{14}$ rad/s, which is actually the second harmonic order of MP resonance with doubled resonance frequency from MP1. The unanimous agreements between the rigorous solution and the analytical LC model prediction at different vacuum gaps clearly verify the physical mechanism of MP excitation in spectrally enhancing near-field radiative transfer between metallic grating structures.

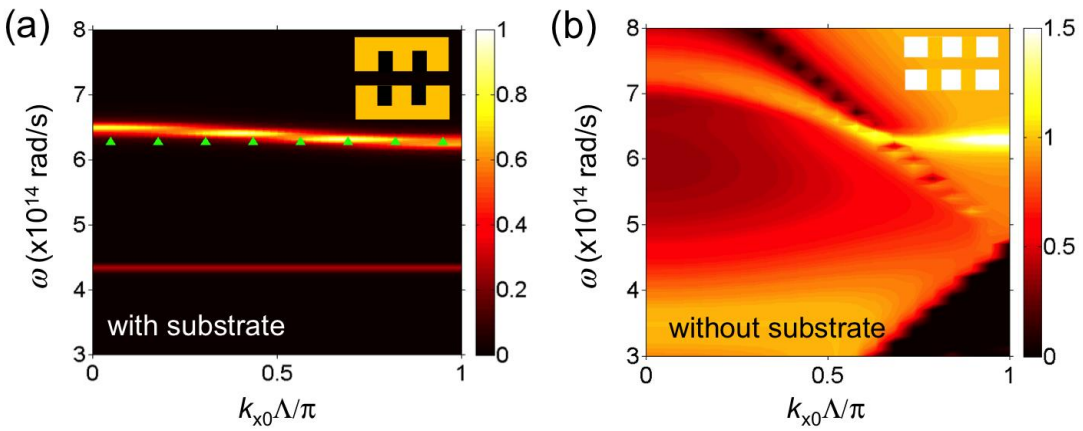

Figure 5.8 Contour plots of *p* polarized energy transmission coefficient (ξ) at vacuum gap of d = 100 nm (a) between two metallic gratings with metal substrate and (b) between two metal slits without metal substrate. Geometric parameters of metallic gratings or slits are Λ = 2 μm, w = 1 μm, and h = 1 μm.

To verify the existence of magnetic polariton or MP in the near field, the LC circuit model developed in Ref. [114] for far-field thermal radiation was applied to confirm the MP resonance frequency mentioned above. However, differently studied in Ref. [114], MP is excited between in the SiO_2 spacer two Ag periodic slits (without Ag substrates). In the present work, we intended to explore the MP excitation between two metallic gratings with semi-infinite substrate. Therefore, here we verify the effect of

grating substrate on the MP resonance frequency, which would justify whether the LC model developed in Ref. [114] for periodic slits is suitable to predict MP excitation between gratings with substrate in this study. In order to verify this, the contour plots of transmission coefficient between two metallic gratings (with metal substrate) and that between two metal slits (without metal substrate but vacuum) are shown in Fig. 5.8(a) and 5.8(b), respectively. By comparison, it is clearly observed that MP is excited as a horizontal enhancement band at the same angular frequency of 6.2×10^{14} rad/s for both metal slits and gratings, though the energy transfer has different magnitudes. The consistence of MP resonance frequency from the rigorous scattering matrix calculation undoubtedly confirms the validity of the LC circuit model developed in Ref. [114] for verifying the MP excitation with metal gratings in this work.

5.2.2 Effect of grating geometry and lateral shift

To further confirm and understand the behaviors of MP resonance in near-field radiative transport across nanometer vacuum gaps, the grating geometric effect on near-field radiative transfer between the Drude grating emitter and receiver is investigated in terms of transmission coefficient at the gap distance d = 20 nm. Figure 5.9(a) and 5.9(b) present the effect of grating depth respectively with h = 0.5 μm and 1.5 μm, while other geometric parameters are kept at the base values. In comparison with the case of h = 1 μm in Fig. 5.7(c), the strong and broad MP resonance mode around $\omega = 5\times10^{14}$ rad/s slightly shifts toward lower frequencies, which is in good agreement with the LC model prediction. Note that, the grating depth h only affects the capacitance C_g, which is less than $C_m/10$ and thereby negligible with given parameters. Therefore, h has little effect on

the MP resonance condition. On the other hand, the guided mode, which strongly depends on the cavity depth, shifts from 4.3×10^{14} rad/s to 6.2×10^{14} rad/ when h increases from 1 μm to 1.5 μm.

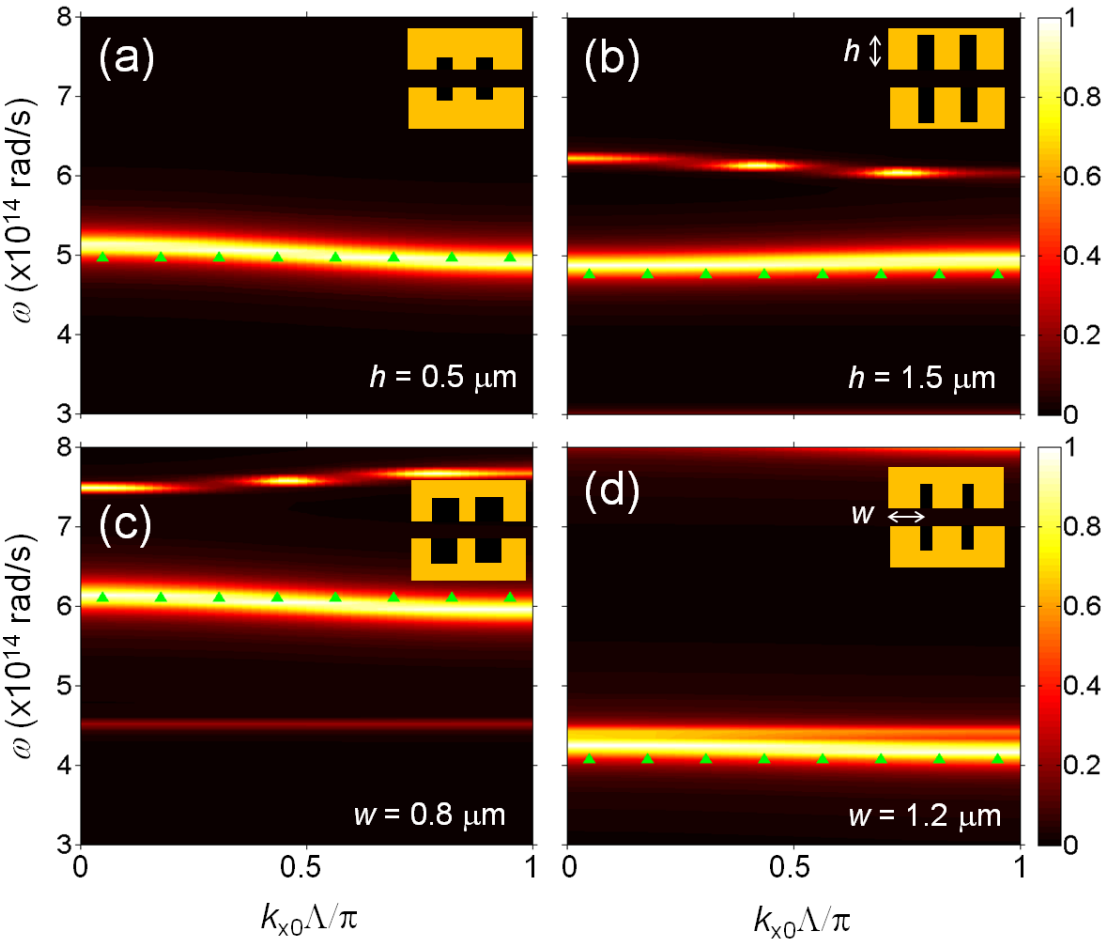

Figure 5.9 Contour plots of energy transmission coefficient (ξ) between two perfectly aligned metallic gratings at d = 20 nm with different geometries: (a) h = 0.5 μm, (b) h = 1.5 μm, (c) w = 0.8 μm, and (d) w = 1.2 μm, while the rest of parameters are kept at the base values: Λ = 2 μm, w = 1 μm, and h = 1 μm. Note that k_y = 0 is assumed and k_{x0} is normalized to the first Brillouin zone. The LC circuit model prediction of MP resonance conditions is shown as green triangles.

The effect of grating width (w) on the near-field radiative transfer spectrally enhanced by MP resonance is studied similarly in terms of transmission coefficient. By comparing Figs. 5.9(c) and 5.9(d) with 5.7(c), when the grating ridges becomes wider from 0.8 to 1.2 μm, both the rigorous solution and the LC model consistently show that the MP resonance mode changes from $\omega = 6.1\times10^{14}$ rad/s to 4.2×10^{14} rad/s. From the perspective of charge distribution, grating width (w) is linear to L_m, L_e, and C_m. With negligible C_g at d = 20 nm, the MP resonance frequency $\omega_{MP1} \approx 1/\sqrt{(L_m + L_e)C_m}$ is essentially inversely proportional to w. Further tuning the geometric parameters of gratings, it is possible to shift the MP resonance and associated spectral flux peak to lower frequencies to better match the thermal wavelength at a given emitter temperature for total heat flux enhancement. On the contrary, the weaker guided mode around $\omega = 4.3\times10^{14}$ rad/s does not change with different grating width, whose resonance frequency is only a strong function of cavity depth H or grating depth h [106].

The discussions on the geometric effect above are for perfectly aligned gratings, i.e. the relative lateral displacement $\Delta/\Lambda = 0$. Figure 5.10(a) and 5.10(b) look into the misalignment effect on the *p*-polarized energy transmission coefficients when the lateral shift is $\Delta/\Lambda = 0.1$ and 0.2, respectively. In comparison with the perfect alignment case in Fig. 5.7(c), slight misalignment will shift the MP resonance band from 5×10^{14} rad/s ($\Delta/\Lambda = 0$) to higher frequencies around 6×10^{14} rad/s ($\Delta/\Lambda = 0.1$) and 7×10^{14} rad/s ($\Delta/\Lambda = 0.2$). This can be understood by the decreasing overlapping metal ridges between the gratings, or an effective overlapping ridge width $w' = w - D$. As shown in Fig. 5.9(c), a smaller ridge width will lead to a higher MP resonance frequency. Moreover, by replacing the

grating width w by w¢, the LC circuit model can be used to simply predict the lateral shift effect on the MP resonance frequency. Clearly, the analytical LC model predicts the same MP behavior as the energy transmission contour from the rigorous solutions, while the discrepancy becomes greater for larger lateral shift, mainly due to the influenced charge distribution upon lateral shift [114]. Clearly, the LC model captures and verifies the geometric effects on the MP resonance behaviors, which effective medium, PA, or cavity resonance could not well explain.

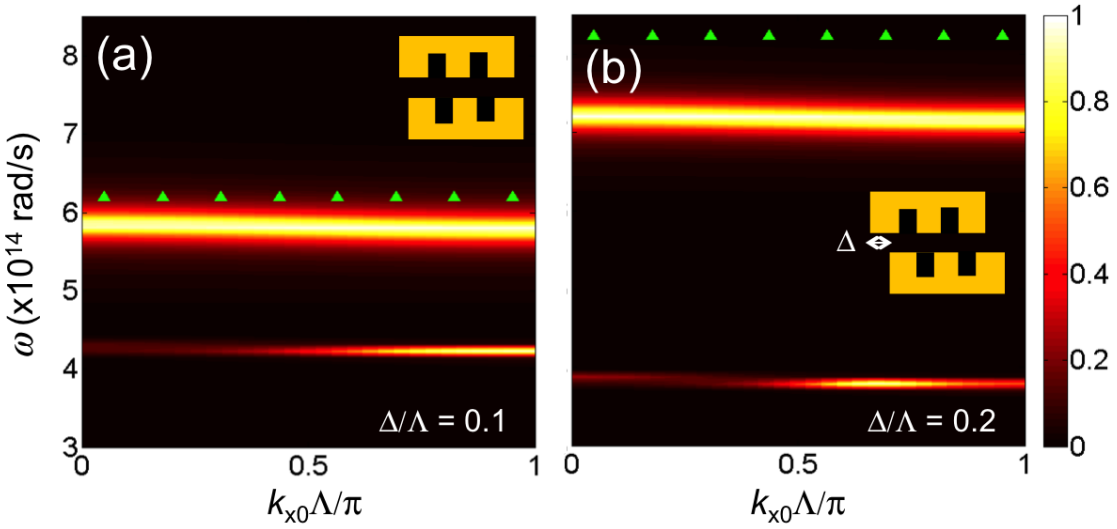

Figure 5.10 Contour plots of energy transmission coefficient (ξ) between two metal gratings (Λ = 2 μm, w = 1 μm, h = 1 μm) at d = 20 nm with different degrees of lateral displacement: (a) Δ/Λ = 0.1 and (b) Δ/Λ = 0.2. Note that k_y = 0 is assumed and k_{x0} is normalized to the first Brillouin zone. The LC circuit model prediction of MP resonance conditions is shown as green triangles.

CHAPTER 6 CONCLUSION AND RECOMMENDATIONS

This dissertation theoretically investigated the dynamic control of radiative heat transfer for thermal management in both far and near fields through applying tunable materials. The optical properties of vanadium dioxide (VO_2) and graphene, which are the two main tunable materials being used, are introduced at first. VO_2 is a phase transition material, which undergoes a phase change from insulator to metal when the temperature goes beyond 68 ℃, while graphene's optical properties can be easily tuned through its chemical potential change.

In far field, a VO_2 based switchable thermal emitter is constructed with a VO_2 thin film sandwiched by a Au grating and Au substrate [122]. When VO_2 is at metallic phase, this device is highly reflective. However, when VO_2 is at insulating phase, there exists an emittance peak as high as 1 at the wavelength around 5 μm, which is caused by the MP resonance. The electromagnetic wave distribution is plotted to present the energy confinement effect, which could be used to verify the existence of MP. The LC circuit model is also employed to predict the MP resonance frequency. Similarly, a VO_2 based tunable thermal emitter is designed as well [84]. As VO_2 changes its phase from insulator to metal, the MP resonance shifts from 15 μm to 10.5 μm. Moreover, I also investigate the tunable emission by covering graphene on top of a SiC 1D grating [85]. MP resonance is excited in the SiC grating slit with an emittance peak, which would shift to different frequency with different graphene chemical potential. This is because the single graphene layer functions as an additional inductor, and the inductance is changing as graphene chemical potential varies. These studies could benefit the applications like optical sensing, energy harvesting/saving in flexible conditions.

In near field, the radiation based thermal management devices including thermal rectifier [72], switch [112] and modulator [123] are theoretically designed. The near-field radiative heat transfer between VO_2 and SiO_2 is explored for the purpose of achieving thermal rectification effect. The emitter and receiver are fixed at 400 K and 300 K, respectively. For the forward bias, SiO_2 is set as the emitter and VO_2 is set as the receiver, which is at the insulating phase. The near-field radiative heat transfer is significantly enhanced due to the strong SPhP coupling between SiO_2 and insulating VO_2. However, for the reverse bias, when VO_2 becomes the emitter, the total heat flux is suppressed because of the weak resonance coupling between SiO_2 and metallic VO_2. The contour plots of transmission coefficients are made to explain the underlying mechanism. The rectification factor can be achieved as high as 2 at vacuum gap distance of 10 nm. A near-field radiation based thermal switch is proposed as well by looking into the heat transfer between two VO_2 plates. The VO_2 receiver temperature is kept at 300 K, while the emitter temperature increases from 330 K to 350 K, for which the VO_2 receiver is always at insulating phase, while the emitter changes its phase from insulating to metallic across 341 K. The "on" mode of the thermal switch is identified when the VO_2 emitter temperature is below 341 K, whose radiative heat transfer is greatly improved due to strong SPhP coupling between two insulating VO_2 plates, and vice the versa. The switching factor could be as high as 0.8 below 20-nm vacuum gap distance. I also investigate the thermal modulation effect based on the near field radiative heat transfer between two graphene covered SiC plates. By tuning graphene chemical potential, the strength and resonance frequency of SPP coupling between graphene covered SiC plates will be changed, which causes the thermal modulation effect. Several parameters,

including the modulation factor, sensitivity and switching factor are defined to characterize the modulation effect. These near-field radiation based thermal management devices possess much faster transport speed with photon than phonon-based ones, which are basically conduction. These devices could also potentially be used to compose an "optical computing" circuit.

As mentioned above, MP is the main mechanism applied in far field to achieve tunable thermal emission, while SPhP/SPP coupling is the main one used in near field. One question is proposed about that whether or not MP exists in near field. I demonstrate the existence of MP in near field for the first time by exploring the near-field radiative transport between two metal gratings [124]. The radiative transfer could be spectrally enhanced between two metal gratings compared with that between two plates. The PA and EMT method, which could respectively capture the mechanism of SPhP/SPP coupling and hyperbolic modes, are also investigated and compared with the rigorous method of scattering matrix theory. However, neither PA nor EMT could predict the spectral heat flux enhancement calculated by the rigorous method. The perfect match between the LC circuit model prediction and the spectral heat flux enhancement confirms that the enhancement is caused by the MP resonance. The vacuum gap distance and grating geometry effect further verifies the existence of MP in the vacuum gap between two metal gratings. The significance of this work is to provide a new scope to manage near-field radiative transfer, which is especially beneficial for energy harvesting systems like thermophotovoltaic.

All the works proposed in this dissertation are based on theoretical calculations, and the future recommendations would be the experimental demonstration. For far-field

metamaterial-based tunable thermal emitters, the experimental demonstration will mainly include the sample fabrication and emittance characterization. One common way to fabricate VO_2 thin film is through sputtering heated V/V_2O_5 target with O_2 input, and the target temperature and O_2 pressure need to be precisely controlled though. A large-area single- or multiple-layer graphene sample could be made by chemical vapor deposition (CVD) technique. The thin film deposition methods include electron beam evaporation, sputtering, and CVD, while I can try to use focused ion beam, photo/electron-beam lithography techniques to fabricate grating based micro/nanostructures. After sample fabrication, the emittance characterization could be done with Fourier Transform Infrared Spectroscopy (FTIR) bench and microscope via measuring the reflectance (R) and transmittance (T), and the emittance, which is equal to the absorptance, could be calculated with $1-R-T$ due to energy balance. Besides the experimental demonstration of the existing devices, I also want to try different tunable materials, micro/nanostructures to achieve tunable thermal emitters with larger tunability and for different specific applications.

The biggest challenge of near-field radiation measurement between two plates is to build a platform to maintain the small vacuum gap distance (usually below 1 μm) between the emitter and receiver. Several methods have been proposed before. As a pioneer work, Ito et al. [95] used the micromachined low-density pillars to create a submicron vacuum gap. Recently, Lim et al. [93] and St-Gelais et al. [94] were able to measure near-field radiative heat transfer between two plates with submicron vacuum gap using MEMS-based platforms. I plan to apply the nanospacer based technique at first, which is simpler in fabrication compared to MEMS based one. The polymer nanospacer

of SU-8 with thermal conductivity of 0.3 W/m-K at room temperature is going to be used. The nanospacer fabrication will include the spin coating of a SU-8 thin film on the sample first, and then using the deep-UV lithography with a photomask to realize an array of dilute square spacers with the spacer size about 2 μm and the spacing between each two about 1 mm, which can minimize the conduction heat transfer to be less than 5% compared with radiative transfer.

REFERENCES

[1] Barker Jr, A., H. Verleur, and H. Guggenheim, *Infrared optical properties of vanadium dioxide above and below the transition temperature.* Physical Review Letters, 1966. **17**(26): p. 1286.

[2] Liu, X. and Z. Zhang, *Graphene-assisted near-field radiative heat transfer between corrugated polar materials.* Applied Physics Letters, 2014. **104**(25): p. 251911.

[3] Rephaeli, E., A. Raman, and S. Fan, *Ultrabroadband photonic structures to achieve high-performance daytime radiative cooling.* Nano Letters, 2013. **13**(4): pp. 1457-1461.

[4] Tittl, A., et al., *Palladium-based plasmonic perfect absorber in the visible wavelength range and its application to hydrogen sensing.* Nano Letters, 2011. **11**(10): pp. 4366-4369.

[5] Celanovic, I., N. Jovanovic, and J. Kassakian, *Two-dimensional tungsten photonic crystals as selective thermal emitters.* Applied Physics Letters, 2008. **92**(19): p. 193101.

[6] Massiot, I., et al., *Nanopatterned front contact for broadband absorption in ultra-thin amorphous silicon solar cells.* Applied Physics Letters, 2012. **101**(16): p. 163901.

[7] Greffet, J.-J., et al., *Coherent emission of light by thermal sources.* Nature, 2002. **416**(6876): pp. 61-64.

[8] Chen, Y.B. and Z.M. Zhang, *Design of tungsten complex gratings for thermophotovoltaic radiators.* Optics Communications, 2007. **269**(2): pp. 411-417.

[9] Heinzel, A., et al., *Radiation filters and emitters for the NIR based on periodically structured metal surfaces.* Journal of Modern Optics, 2000. **47**(13): pp. 2399-2419.

[10] Pralle, M., et al., *Photonic crystal enhanced narrow-band infrared emitters.* Applied Physics Letters, 2002. **81**(25): pp. 4685-4687.

[11] Narayanaswamy, A. and G. Chen, *Thermal emission control with one-dimensional metallodielectric photonic crystals.* Physical Review B, 2004. **70**(12): p. 125101.

[12] Nagpal, P., et al., *Efficient Low-Temperature Thermophotovoltaic emitters from metallic photonic crystals.* Nano Letters, 2008. **8**(10): pp. 3238-3243.

[13] Laroche, M., et al., *Tailoring silicon radiative properties.* Optics Communications, 2005. **250**(4): pp. 316-320.

[14] Wang, L., S. Basu, and Z. Zhang, *Direct measurement of thermal emission from a Fabry–Perot cavity resonator.* Journal of Heat Transfer, 2012. **134**(7): p. 072701.

[15] Qazilbash, M., et al., *Infrared spectroscopy and nano-imaging of the insulator-to-metal transition in vanadium dioxide.* Physical Review B, 2009. **79**(7): p. 075107.

[16] Wen, Q.-Y., et al., *A tunable hybrid metamaterial absorber based on vanadium oxide films.* Journal of Physics D: Applied Physics, 2012. **45**(23): p. 235106.

[17] Li, J.-N., W. Li, and S.-J. Chang, *Terahertz metamaterial modulator based on vanadium dioxide.* Journal of Electronic Science and Technology, 2014. **1**: p. 009.

[18] Dicken, M.J., et al., *Frequency tunable near-infrared metamaterials based on VO2 phase transition.* Opt. Express, 2009. **17**(20): pp. 18330-18339.

[19] Kats, M.A., et al., *Thermal tuning of mid-infrared plasmonic antenna arrays using a phase change material.* Optics Letters, 2013. **38**(3): pp. 368-370.

[20] Kats, M.A., et al., *Ultra-thin perfect absorber employing a tunable phase change material.* Applied Physics Letters, 2012. **101**(22): p. 221101.

[21] Ben-Abdallah, P., H. Benisty, and M. Besbes, *Microsecond switchable thermal antenna.* Journal of Applied Physics, 2014. **116**(3): p. 034306.

[22] Falkovsky, L. and A. Varlamov, *Space-time dispersion of graphene conductivity.* The European Physical Journal B, 2007. **56**(4): pp. 281-284.

[23] Falkovsky, L. *Optical properties of graphene*. Journal of Physics: Conference Series, 2008. **129**(1): p. 012004.

[24] Falkovsky, L. and S. Pershoguba, *Optical far-infrared properties of a graphene monolayer and multilayer*. Physical Review B, 2007. **76**(15): p. 153410.

[25] Wu, J., et al., *Design of infrared surface plasmon resonance sensors based on graphene ribbon arrays.* Optics & Laser Technology, 2014. **59**: pp. 99-103.

[26] Cheng, H., et al., *Dynamically tunable plasmonically induced transparency in periodically patterned graphene nanostrips.* Applied Physics Letters, 2013. **103**(20): p. 203112.

[27] Chu, H.-S. and C.H. Gan, *Active plasmonic switching at mid-infrared wavelengths with graphene ribbon arrays.* Applied Physics Letters, 2013. **102**(23): p. 231107.

[28] Alaee, R., et al., *A perfect absorber made of a graphene micro-ribbon metamaterial.* Optics Express, 2012. **20**(27): pp. 28017-28024.

[29] Thongrattanasiri, S., F.H. Koppens, and F.J.G. de Abajo, *Complete optical absorption in periodically patterned graphene.* Physical Review Letters, 2012. **108**(4): p. 047401.

[30] Fang, Z., et al., *Active tunable absorption enhancement with graphene nanodisk arrays.* Nano Letters, 2013. **14**(1): pp. 299-304.

[31] Song, S., et al., *Great light absorption enhancement in a graphene photodetector integrated with a metamaterial perfect absorber.* Nanoscale, 2013. **5**(20): pp. 9615-9619.

[32] Roberts, N. and D. Walker, *A review of thermal rectification observations and models in solid materials.* International Journal of Thermal Sciences, 2011. **50**(5): pp. 648-662.

[33] Li, B., L. Wang, and G. Casati, *Thermal diode: rectification of heat flux.* Physical Review Letters, 2004. **93**(18): p. 184301.

[34] Dames, C., *Solid-state thermal rectification with existing bulk materials.* Journal of Heat Transfer, 2009. **131**(6).

[35] Chang, C., et al., *Solid-state thermal rectifier.* Science, 2006. **314**(5802): pp. 1121-1124.

[36] Li, B., L. Wang, and G. Casati, *Negative differential thermal resistance and thermal transistor.* Applied Physics Letters, 2006. **88**(14): p. 143501.

[37] Miner, A., A. Majumdar, and U. Ghoshal, *Thermoelectromechanical refrigeration based on transient thermoelectric effects.* Applied Physics Letters, 1999. **75**(8): pp. 1176-1178.

[38] Snyder, G.J., et al., *Supercooling of Peltier cooler using a current pulse.* Journal of Applied Physics, 2002. **92**(3): pp. 1564-1569.

[39] Wei-Cheng, T., et al., *Multiple-stage microfabricated preconcentrator-focuser for micro gas chromatography system.* Journal of Microelectromechanical Systems, 2005. **14**(3): pp. 498-507.

[40] Polder, D. and M. Van Hove, *Theory of radiative heat transfer between closely spaced bodies.* Physical Review B, 1971. **4**(10): pp. 3303-3314.

[41] Hu, L., et al., *Near-field thermal radiation between two closely spaced glass plates exceeding Planck's blackbody radiation law.* Applied Physics Letters, 2008. **92**(13): p. 133106.

[42] Kralik, T., et al., *Strong near-field enhancement of radiative heat transfer between metallic surfaces.* Physical Review Letters, 2012. **109**(22): p. 224302.

[43] Cahill, D.G., et al., *Nanoscale thermal transport.* Journal of Applied Physics, 2003. **93**(2): p. 793.

[44] Cahill, D.G., et al., *Nanoscale thermal transport. II. 2003–2012.* Applied Physics Reviews, 2014. **1**(1): p. 011305.

[45] Mulet, J.-P., et al., *Nanoscale radiative heat transfer between a small particle and a plane surface.* Applied Physics Letters, 2001. **78**(19): pp. 2931-2933.

[46] Mulet, J.-P., et al., *Enhanced radiative heat transfer at nanometric distances.* Microscale Thermophysical Engineering, 2002. **6**(3): pp. 209-222.

[47] Otey, C.R., W.T. Lau, and S. Fan, *Thermal rectification through vacuum.* Physical Review Letters, 2010. **104**(15): p. 154301.

[48] Iizuka, H. and S. Fan, *Rectification of evanescent heat transfer between dielectric-coated and uncoated silicon carbide plates.* Journal of Applied Physics, 2012. **112**(2): p. 024304.

[49] Basu, S. and M. Francoeur, *Near-field radiative transfer based thermal rectification using doped silicon.* Applied Physics Letters, 2011. **98**(11): p. 113106.

[50] Wang, L.P. and Z.M. Zhang, *Thermal rectification enabled by near-field radiative heat transfer between intrinsic silicon and a dissimilar material.* Nanoscale and Microscale Thermophysical Engineering, 2013. **17**(4): pp. 337-348.

[51] Zhu, L., C.R. Otey, and S. Fan, *Negative differential thermal conductance through vacuum.* Applied Physics Letters, 2012. **100**(4): p. 044104.

[52] Volokitin, A.I. and B.N.J. Persson, *Near-field radiative heat transfer between closely spaced graphene and amorphous SiO_{2}.* Physical Review B, 2011. **83**(24): p. 241407.

[53] Ilic, O., et al., *Near-field thermal radiation transfer controlled by plasmons in graphene.* Physical Review B, 2012. **85**(15): p. 155422.

[54] Svetovoy, V.B., P.J. van Zwol, and J. Chevrier, *Plasmon enhanced near-field radiative heat transfer for graphene covered dielectrics.* Physical Review B, 2012. **85**(15): p. 155418.

[55] Lim, M., S.S. Lee, and B.J. Lee, *Near-field thermal radiation between graphene-covered doped silicon plates.* Optics Express, 2013. **21**(19): pp. 22173-22185.

[56] Ben-Abdallah, P., et al., *Heat flux splitter for near-field thermal radiation.* Applied Physics Letters, 2015. **107**(5): p. 053109.

[57] van Zwol, P.J., et al., *Phonon polaritons enhance near-field thermal transfer across the phase transition of VO_{2}.* Physical Review B, 2011. **84**(16): p. 161413.

[58] Zhang, Z.M., *Nano/Microscale Heat Transfer*. 2007, New York: McGraw-Hill.

[59] Falkovsky, L. and A. Varlamov, *Space-time dispersion of graphene conductivity.* The European Physical Journal B-Condensed Matter and Complex Systems, 2007. **56**(4): pp. 281-284.

[60] Li, L., *Use of Fourier series in the analysis of discontinuous periodic structures.* Journal of the Optical Society of America A, 1996. **13**(9): pp. 1870-1876.

[61] Moharam, M.G., et al., *Formulation for stable and efficient implementation of the rigorous coupled-wave analysis of binary gratings.* Journal of the Optical Society of America A, 1995. **12**(5): pp. 1068-1076.

[62] Guérout, R., et al., *Thermal Casimir force between nanostructured surfaces.* Physical Review A, 2013. **87**(5): p. 052514.

[63] Rytov, S.M., Y.A. Kravtsov, and V.I. Tatarskii, *Principles of statistical radiophysics 2.* 1988.

[64] Basu, S., Z.M. Zhang, and C.J. Fu, *Review of near-field thermal radiation and its application to energy conversion.* International Journal of Energy Research, 2009. **33**(13): pp. 1203-1232.

[65] Biehs, S.-A., *Thermal heat radiation, near-field energy density and near-field radiative heat transfer of coated materials.* The European Physical Journal B-Condensed Matter and Complex Systems, 2007. **58**(4): pp. 423-431.

[66] Francoeur, M., M.P. Mengüç, and R. Vaillon, *Spectral tuning of near-field radiative heat flux between two thin silicon carbide films.* Journal of Physics D: Applied Physics, 2010. **43**(7): p. 075501.

[67] Biehs, S.A., et al., *Nanoscale heat flux between nanoporous materials.* Optics Express, 2011. **19**(S5): pp. A1088-A1103.

[68] Wang, H., et al., *Anisotropic optical properties of silicon nanowire arrays based on the effective medium approximation.* International Journal of Thermal Sciences, 2013. **65**: pp. 62-69.

[69] Lee, B., L. Wang, and Z. Zhang, *Coherent thermal emission by excitation of magnetic polaritons between periodic strips and a metallic film.* Optics Express, 2008. **16**(15): pp. 11328-11336.

[70] Wang, L. and Z. Zhang, *Wavelength-selective and diffuse emitter enhanced by magnetic polaritons for thermophotovoltaics.* Applied Physics Letters, 2012. **100**(6): p. 063902.

[71] Palik, E.D., *Handbook of optical constants of solids*. 1998.

[72] Yang, Y., S. Basu, and L. Wang, *Radiation-based near-field thermal rectification with phase transition materials.* Applied Physics Letters, 2013. **103**(16): p. 163101.

[73] Wang, H. and L. Wang, *Perfect selective metamaterial solar absorbers.* Optics Express, 2013. **21**(106): pp. A1078-A1093.

[74] Zhao, B., et al., *Thermophotovoltaic emitters based on a two-dimensional grating/thin-film nanostructure.* International Journal of Heat and Mass Transfer, 2013. **67**: pp. 637-645.

[75] Zhou, J., et al., *Unifying approach to left-handed material design.* Optics Letters, 2006. **31**(24): pp. 3620-3622.

[76] Costa, F., et al., *A circuit-based model for the interpretation of perfect metamaterial absorbers.* 2012. **61**(3): pp. 1201-1209.

[77] Isenstadt, A. and J. Xu, *Subwavelength metal optics and antireflection.* Electronic Materials Letters, 2013. **9**(2): pp. 125-132.

[78] Cortes, C., et al., *Quantum nanophotonics using hyperbolic metamaterials.* Journal of Optics, 2012. **14**(6): p. 063001.

[79] Liu, M., et al., *Symmetry breaking and geometric confinement in VO2: Results from a three-dimensional infrared nano-imaging.* Applied Physics Letters, 2014. **104**(12): p. 121905.

[80] Liu, M., et al., *Anisotropic electronic state via spontaneous phase separation in strained vanadium dioxide films.* Physical Review Letters, 2013. **111**(9): p. 096602.

[81] Wang, L. and Z. Zhang, *Phonon-mediated magnetic polaritons in the infrared region.* Optics Express, 2011. **19**(102): pp. A126-A135.

[82] Zhao, B., J. Zhao, and Z. Zhang, *Enhancement of near-infrared absorption in graphene with metal gratings.* Applied Physics Letters, 2014. **105**(3): p. 031905.

[83] Chen, Y.-B. and F.-C. Chiu, *Trapping mid-infrared rays in a lossy film with the Berreman mode, epsilon near zero mode, and magnetic polaritons.* Optics Express, 2013. **21**(18): pp. 20771-20785.

[84] Wang, H., Y. Yang, and L. Wang, *Infrared frequency-tunable coherent thermal sources.* Journal of Optics, 2015. **17**(4): p. 045104.

[85] Wang, H., Y. Yang, and L. Wang, *Wavelength-tunable infrared metamaterial by tailoring magnetic resonance condition with VO2 phase transition.* Journal of Applied Physics, 2014. **116**(12): p. 123503.

[86] Basu, S., B.J. Lee, and Z.M. Zhang, *Near-field radiation calculated with an improved dielectric function model for doped silicon.* Journal of Heat Transfer, 2009. **132**(2): p. 023302.

[87] Francoeur, M., M.P. Mengüç, and R. Vaillon, *Coexistence of multiple regimes for near-field thermal radiation between two layers supporting surface phonon polaritons in the infrared.* Physical Review B, 2011. **84**(7): p. 075436.

[88] Basu, S. and Z. Zhang, *Ultrasmall penetration depth in nanoscale thermal radiation.* Applied Physics Letters, 2009. **95**(13): p. 133104.

[89] Francoeur, M., M.P. Mengüç, and R. Vaillon, *Coexistence of multiple regimes for near-field thermal radiation between two layers supporting surface phonon polaritons in the infrared.* Physical Review B, 2011. **84**(7): p. 075436.

[90] Rytov, S.M., *Principles of Statistical Radiophysics*. Springer-Verlag, 1987.

[91] Berger, C., et al., *Electronic confinement and coherence in patterned epitaxial graphene.* Science, 2006. **312**(5777): pp. 1191-1196.

[92] Ohta, T., et al., *Controlling the electronic structure of bilayer graphene.* Science, 2006. **313**(5789): pp. 951-954.

[93] Lim, M., S.S. Lee, and B.J. Lee, *Near-field thermal radiation between doped silicon plates at nanoscale gaps.* Physical Review B, 2015. **91**(19): p. 195136.

[94] St-Gelais, R., et al., *Demonstration of strong near-field radiative heat transfer between integrated nanostructures.* Nano Letters, 2014. **14**(12): pp. 6971-6975.

[95] Ito, K., et al., *Parallel-plate submicron gap formed by micromachined low-density pillars for near-field radiative heat transfer.* Applied Physics Letters, 2015. **106**(8): p. 083504.

[96] Falkovsky, L.A. and S.S. Pershoguba, *Optical far-infrared properties of a graphene monolayer and multilayer.* Physical Review B, 2007. **76**(15): p. 153410.

[97] Falkovsky, L.A., *Optical properties of graphene.* Journal of Physics: Conference Series, 2008. **129**(1): p. 012004.

[98] Messina, R., et al., *Tuning the electromagnetic local density of states in graphene-covered systems via strong coupling with graphene plasmons.* Physical Review B, 2013. **87**(8): p. 085421.

[99] Pendry, J., *Radiative exchange of heat between nanostructures.* Journal of Physics: Condensed Matter, 1999. **11**(35): p. 6621.

[100] Shen, S., A. Narayanaswamy, and G. Chen, *Surface phonon polaritons mediated energy transfer between nanoscale gaps.* Nano Letters, 2009. **9**(8): pp. 2909-2913.

[101] Basu, S. and M. Francoeur, *Penetration depth in near-field radiative heat transfer between metamaterials.* Applied Physics Letters, 2011. **99**(14): p. 143107.

[102] Petersen, S.J., S. Basu, and M. Francoeur, *Near-field thermal emission from metamaterials.* Photonics and Nanostructures-Fundamentals and Applications, 2013. **11**(3): pp. 167-181.

[103] Biehs, S.-A., M. Tschikin, and P. Ben-Abdallah, *Hyperbolic metamaterials as an analog of a blackbody in the near field.* Physical Review Letters, 2012. **109**(10): p. 104301.

[104] Guo, Y., et al., *Broadband super-Planckian thermal emission from hyperbolic metamaterials.* Applied Physics Letters, 2012. **101**(13): p. 131106.

[105] Molesky, S., C.J. Dewalt, and Z. Jacob, *High temperature epsilon-near-zero and epsilon-near-pole metamaterial emitters for thermophotovoltaics.* Optics Express, 2013. **21**(101): pp. A96-A110.

[106] Guérout, R., et al. *Enhanced radiative heat transfer between nanostructured gold plates*. in Journal of Physics: Conference Series. 2012. 395(1): p. 012154.

[107] Dai, J., S.A. Dyakov, and M. Yan, *Enhanced near-field radiative heat transfer between corrugated metal plates: Role of spoof surface plasmon polaritons.* Physical Review B, 2015. **92**(3): p. 035419.

[108] Liu, X., B. Zhao, and Z.M. Zhang, *Enhanced near-field thermal radiation and reduced Casimir stiction between doped-Si gratings.* Physical Review A, 2015. **91**(6): p. 062510.

[109] Park, K., et al., *Performance analysis of near-field thermophotovoltaic devices considering absorption distribution.* Journal of Quantitative Spectroscopy and Radiative Transfer, 2008. **109**(2): pp. 305-316.

[110] Hoshino, K., et al., *Nanoscale fluorescence imaging with quantum dot near-field electroluminescence.* Applied Physics Letters, 2012. **101**(4): p. 043118.

[111] Ben-Abdallah, P. and S.-A. Biehs, *Near-field thermal transistor.* Physical Review Letters, 2014. **112**(4): p. 044301.

[112] Yang, Y., S. Basu, and L. Wang, *Vacuum thermal switch made of phase transition materials considering thin film and substrate effects.* Journal of Quantitative Spectroscopy and Radiative Transfer, 2015. **158**: pp. 69-77.

[113] Gu, W., G.-H. Tang, and W.-Q. Tao, *Thermal switch and thermal rectification enabled by near-field radiative heat transfer between three slabs.* International Journal of Heat and Mass Transfer, 2015. **82**: pp. 429-434.

[114] Wang, L. and Z.M. Zhang, *Effect of magnetic polaritons on the radiative properties of double-layer nanoslit arrays.* Journal of the Optical Society of America B, 2010. **27**(12): pp. 2595-2604.

[115] Bimonte, G., *Scattering approach to Casimir forces and radiative heat transfer for nanostructured surfaces out of thermal equilibrium.* Physical Review A, 2009. **80**(4): p. 042102.

[116] Messina, R. and M. Antezza, *Casimir-Lifshitz force out of thermal equilibrium and heat transfer between arbitrary bodies.* Europhysics Letters, 2011. **95**(6): p. 61002.

[117] Krüger, M., T. Emig, and M. Kardar, *Nonequilibrium electromagnetic fluctuations: heat transfer and interactions.* Physical Review Letters, 2011. **106**(21): p. 210404.

[118] Lussange, J., et al., *Radiative heat transfer between two dielectric nanogratings in the scattering approach.* Physical Review B, 2012. **86**(8): p. 085432.

[119] Lambrecht, A. and V.N. Marachevsky, *Casimir interaction of dielectric gratings.* Physical Review Letters, 2008. **101**(16): p. 160403.

[120] Chalabi, H., E. Hasman, and M.L. Brongersma, *Near-field radiative thermal transfer between a nanostructured periodic material and a planar substrate.* Physical Review B, 2015. **91**(1): p. 014302.

[121] Liu, X., T. Bright, and Z. Zhang, *Application conditions of effective medium theory in near-field radiative heat transfer between multilayered metamaterials.* Journal of Heat Transfer, 2014. **136**(9): p. 092703.

[122] Wang, H., Y. Yang, and L. Wang, *Switchable wavelength-selective and diffuse metamaterial absorber/emitter with a phase transition spacer layer.* Applied Physics Letters, 2014. **105**(7): p. 071907.

[123] Yang, Y. and L. Wang, *Electrically-controlled near-field radiative thermal modulator made of graphene-coated silicon carbide plates.* Journal of Quantitative Spectroscopy and Radiative Transfer, 2016, in press.

[124] Yang, Y. and L. Wang, *Spectrally enhancing near-field radiative transfer between metallic gratings by exciting magnetic polaritons in nanometric vacuum gap.* Physical Review Letters, 2016. **117**: p. 044301.

VITA

YUE YANG

Yue Yang was born in Anqing, Anhui Province, China in 1990. He received his Bachelor's degree from the University of Science and Technology of China in 2012 in mechanical engineering. Yue entered the School for Engineering of Matter, Transport and Energy at Arizona State University in Fall 2012 as a PhD student, and since then he has been studying in Dr. Liping Wang's group in the area of nanoscale radiative heat transfer. His research focuses on dynamic control of radiative heat transfer with tunable materials for thermal management in both far and near fields.

During his PhD study, he has published over 10 journal papers listed below in *Physical Review Letters*, *Applied Physics Letters*, *Journal of Quantitative Spectroscopy and Radiative Transfer*, and other peer-reviewed journals. He has also co-authored over 15 conference presentations, and has given several oral and poster presentations in international conferences, such as *8th International Symposium on Radiative Transfer*, *The 6th International Conference on Metamaterials, Photonic Crystals and Plasmonics* and *ASME 2013 International Mechanical Engineering Congress and Exposition*. He also received the GPSA *travel grant* in 2016, ASU *University Graduate Fellowship* in 2014 and *travel grant* from the US National Science of Foundation in 2013. Besides, he has been actively contributing to the professional community by reviewing scientific manuscripts.

Dissertation Related Journal Publication List

1. **Yang, Y.** and L. Wang, *Spectrally enhancing near-field radiative transfer between metallic gratings by exciting magnetic polaritons in nanometric vacuum gap.* Physical Review Letters, 2016. **117**: p. 044301.
2. **Yang, Y.** and L. Wang, *Electrically-controlled near-field radiative thermal modulator made of graphene-coated silicon carbide plates.* Journal of Quantitative Spectroscopy and Radiative Transfer, 2016, in press. doi: 10.1016/j.jqsrt.2016.06.013.
3. **Yang, Y.**, S. Basu, and L. Wang, *Vacuum thermal switch made of phase transition materials considering thin film and substrate effects.* Journal of Quantitative Spectroscopy and Radiative Transfer, 2015. **158**: pp. 69-77.
4. Wang, H.[#], **Y. Yang**[#], and L. Wang, *Infrared frequency-tunable coherent thermal sources.* Journal of Optics, 2015. **17**(4): p. 045104. (# Equal contribution)
5. Wang, H., **Y. Yang**, and L. Wang, *Wavelength-tunable infrared metamaterial by tailoring magnetic resonance condition with VO2 phase transition.* Journal of Applied Physics, 2014. **116**(12): p. 123503.
6. Wang, H., **Y. Yang**, and L. Wang, *Switchable wavelength-selective and diffuse metamaterial absorber/emitter with a phase transition spacer layer.* Applied Physics Letters, 2014. **105**(7): p. 071907.
7. **Yang, Y.**, S. Basu, and L. Wang, *Radiation-Based Near-Field Thermal Rectification with Phase Transition Materials*. Applied Physics Letters, 2013. **103**(16): p. 163101.

Dissertation Non-Related Journal Publication List

1. **Yang, Y.**[#], P. Sabbaghi[#], and L. Wang, *Effects of Magnetic Polaritons in SiC Deep Gratings on Radiative Transport from Far to Near Field*. International Journal of Heat and Mass Transfer, 2016, submitted. (# Equal Contribution)
2. **Yang, Y.**, J.-Y. Chang , P. Sabbaghi, and L. Wang, *Performance Analysis of a Near-Field Thermophotovoltaic Device with a Metallodielectric Selective Emitter and Electrical Contacts for the Photovoltaic Cell*. Journal of Heat Transfer, accepted.
3. Chang, J.-Y., **Y. Yang**, and L. Wang, *Extraordinary Photon Transport by Near-Field Coupling of a Nanostructured Metamaterial with a Graphene-Covered Dielectric Plate*. Journal of Quantitative Spectroscopy and Radiative Transfer, 2016. **184**: pp. 58-67.
4. Chang, J.-Y., S. Basu, S., **Y. Yang**, and L. Wang, *Near-field Radiation between Dual Uniaxial Electromagnetic Metamaterials*. Journal of Applied Physics, 2016. **119**: p. 213108.
5. Wang, H., J.-Y. Chang, **Y. Yang**, and L. Wang, *Performance Analysis of Solar Thermophotovoltaic Conversion Enhanced by Selective Metamaterial Absorbers and Emitters*. International Journal of Heat and Mass Transfer, 2016. **98**: pp. 788-798.
6. Chang, J.-Y., **Y. Yang**, and L. Wang, *Tungsten Nanowire Based Hyperbolic Metamaterial Emitters for Near-Field Thermophotovoltaic Applications*. International Journal of Heat and Mass Transfer, 2015. **87**: pp. 237-247.
7. Basu, S., **Y. Yang,** and L. Wang, *Near-Field Radiative Heat Transfer between Metamaterials Coated with Silicon Carbide Thin Films*. Applied Physics Letters, 2015. **106**(3): p. 103106.